Coherent control of spatial resolution enhancement with scalar and vector beams

A thesis submitted by

Partha Das

to

Indian Institute of Technology Guwahati

in partial fulfillment of the requirements for the degree of

DOCTOR OF PHILOSOPHY

Under the Supervision of

Prof. Tarak Nath Dey

Department of Physics
Indian Institute of Technology Guwahati
Guwahati - 781039, Assam, India

March 2, 2026

TH-3976_186121017

TH-3976_186121017

Dedicated

to

my grandfather

TH-3976_186121017

Declaration

I hereby declare that the research work presented in this thesis, entitled "**Coherent control of spatial resolution enhancement with scalar and vector beams**", has been conducted solely by me under the supervision of Prof. Tarak Nath Dey, Department of Physics, Indian Institute of Technology Guwahati, India. This thesis is an original piece of work and has not been submitted, either in part or in full, for the award of any degree or qualification at this or any other university. Except where explicit reference is made in the text, the work reported herein is entirely my own.

Partha Das
February 24, 2026

Partha Das
Roll No. 186121017
Department of Physics
Indian Institute of Technology Guwahati
Guwahati, India
E-mail: partha.2015@iitg.ac.in

TH-3976_186121017

Certificate

This is to certify that the work presented in the thesis entitled "**Coherent control of spatial resolution enhancement with scalar and vector beams**", submitted by Partha Das in partial fulfillment of the requirements for the award of the degree of Doctor of Philosophy in Physics, Department of Physics, Indian Institute of Technology Guwahati, is an original record of research carried out by the candidate under my supervision and guidance. The contents of this thesis have not been submitted, either in part or in full, to any other university or institute for the award of any degree.

Prof. Tarak Nath Dey
February 24, 2026

Dr. Tarak Nath Dey
Professor
Department of Physics
Indian Institute of Technology, Guwahati
Guwahati, India
E-mail: tarak.dey@iitg.ac.in

TH-3976_186121017

TH-3976_186121017

Acknowledgment

"A journey of a thousand miles begins with a single step." — Lao Tzu

As I look back on this long academic journey, I am reminded of the many hands and hearts that guided and supported me along the way. I offer my sincere gratitude to all of them. I would like to take this opportunity to thank everyone whose encouragement, assistance, and presence made the completion of this thesis possible. First of all I would like to thank my supervisor Prof. Tarak Nath Dey, for his constant support, guidance, and advice throughout my Ph.D. journey. I will not forget his support during the challenging time of my family. I am greatly indebted to him for giving me the opportunity to carry out my research work under his supervision.

I would like to thank my doctoral committee members, Prof. Ashwini Kumar Sharma, Prof. Basanta Ranjan Boruah, and Prof. Gagan Kumar for their insightful comments and suggestions during my annual progress seminars.

I am also indebted to other professors at IIT Guwahati, specially Prof. Bibhas Ranjan Majhi, Prof. Debaprasad Maity, Prof. Arunansu Sil, Dr. Uday Narayan Maity, Dr. Arif Warsi Laskar, and my master's project guide Prof. Soumitra Nandi. I also thank all academic and non-academic staff of the physics department. Sincere acknowledgement goes to the financial assistance from MHRD and the project grant from ANRF, which helped me in completing my research work successfully. I thank my seniors, Dr. Sandeep Sharma, Dr. Nawaz Sarif Mallick, Dr. Nilamoni Daloi, Dr. Samit Kumar Hazra, and Dr. Sanket Das, for their insightful discussions and guidance on various aspects of my research. I would also like to thank my juniors, Madan Mohan Mahana and Gunjan Yadav, for their fruitful discussions. A special thanks to Dr. Nilamoni Daloi, whose help with numerical coding was indispensable.

I am grateful to have been a part of the IITG SPIE student chapter. I thank all the members and wish them the very best in their noble outreach activities.

It is my pleasure to acknowledge the "walk after dinner" group members Rony da, Samit, Swarup, Soumen, Amit, Avishek, Niloy, and Saswata for the enjoyable conversations, fun moments, and enlightening discussions on physics and beyond.

Thanks are also due to all my batchmates, especially Nikhil, with whom I spent countless hours in Brahmaputra hostel discussing wildlife, academics, and much more. His help in improving my spoken English is something I deeply appreciate. I also thank all the mess workers and hostel maintenance staff for their dedicated efforts that made hostel life comfortable.

I would also like to take this opportunity to thank my table-tennis partners—Sovan Sau, Surojit da, Arghyajit da, and Sayan da for helping me stay physically active and refreshed through sports.

My sincere gratitude goes to some of the extraordinary school teachers, like Maheswar sir and Gautam sir, whose teachings and discipline deeply shaped my outlook and motivation.

I came across so many good friends throughout my school and college years. I thank Sanjay, Saptarshi, Shubham, Souvik, Arnab Sarkar, Arnab Seth, Arnab Bera, Partha Sarathi Rana, Ritesh, Balaram, and Mithun for their enduring friendship. I am grateful to Sudha, my Master's friend with whom I still share a lot of thoughts on physics and many aspects of life. During the COVID lockdown, playing online chess with Sudha and Ritesh helped me cope with the long periods of isolation.

On a personal note, this thesis would not have been possible without the unconditional love and support of my parents, my grandmother, and beloved sister Puja. My parents always encouraged me to pursue the path I was interested in, and the values and principles they instilled in me from childhood have remained a guiding force throughout my journey. My sister consistently gave me strength and kept me motivated during difficult times. Finally, I express my heartfelt gratitude to my soulmate Tiyasa for her unwavering love, support, and faith in me.

Abstract

The work presented in this thesis investigates the coherent manipulation of light-matter interactions using scalar and vector beams to achieve controlled enhancement of spatial resolution. In the first two research works, we employ atomic media to examine how scalar and vector beam influences linear and nonlinear optical responses, while the third work extends this exploration to a quantum dot system to realize super-resolution imaging with structured light.

In Chapter 1, we provide a concise introduction to the fundamental theories and essential concepts that form the foundation of this thesis. We adopt a semiclassical framework to describe light–matter interaction, beginning with Maxwell's equations to outline the classical behaviour of electromagnetic radiation. The propagation of electromagnetic waves in linear and nonlinear media is subsequently derived within the paraxial approximation. We then develop the atom–field interaction Hamiltonian under the electric-dipole approximation and introduce the density-matrix formalism as a powerful tool for analysing quantum systems. In this chapter we also include a discussion of exciton–phonon interactions in quantum dots. Later in this chapter, we investigate how electromagnetic fields interact with two- and three-level atomic systems, highlighting several intriguing optical phenomena that arise in such configurations. The concept of super-resolution is introduced, and the resolution limit for stimulated emission depletion (STED) microscopy is explicitly derived. Finally, we present an overview of vector beams, their methods of generation, and their potential applications in modern photonics.

In Chapter 2, we address the first research problem by investigating the phase-induced susceptibility of both components of cylindrical vector beams in a nondegenerate four-level closed-loop atomic system. The closed-loop configuration renders the relative phase between the probe beam and control field a critical parameter for manipulating the medium's linear susceptibility. Variations in this phase shift correspond to distinct quantum excitation pathways, giving rise to either gain or loss in the medium. We analyse the state of polarization of the probe vector beam as it propagates over one Rayleigh length, demonstrating that the phase shift leads to characteristic polarization rotation. The study is further extended into the nonlinear regime by increasing the probe intensity and atomic density. Under these conditions, we observe quasi-periodic chain-like self-focusing and self-defocusing patterns for radial, azimuthal, and spiral vector beams. Such nonlinear interactions result in a significant reduction of the beam spot size, accompanied by enhanced gain, suggesting promising avenues for resolution enhancement.

In Chapter 3, we compare the focusing behaviour of scalar and vector beams in a four-level active-Raman-gain medium. Using the probability-amplitude method, we analytically derive both the linear and third-order nonlinear susceptibilities of the system. Owing to the nonzero detuning of the signal field, the cross-Kerr nonlinearity becomes significantly enhanced, enabling strong beam modulation. By appropriately choosing the input field intensities and the spatial profile of the control beam, the scalar probe beam can be focused within the medium. Although the energy transfer from the control beam to the probe beam contributes to the focusing, it is the enhanced cross-Kerr nonlinearity that leads to a substantial reduction in the probe beam waist. In contrast, when a vector beam is used as the probe, we observe gain-assisted narrowing arising predominantly from energy transfer from the control beam. We also examine the state of polarization of the vector beam at its minimum

beam waist. Overall, this chapter offers a comprehensive account of the distinct focusing phenomena exhibited by scalar and vector beams in an active-Raman-gain configuration.

In Chapter 4, we explore super-resolution imaging in a two-level quantum dot system using two structured spatiotemporal beams incorporating chirping and time delay. The rapid adiabatic passage (RAP) protocol is employed to achieve robust population transfer between the ground and excited states. Based on the stimulated emission depletion microscopy technique, and appropriately tailoring the spatiotemporal envelopes of the structured beams, we demonstrate the generation of a super-resolved spot. To investigate the influence of temperature-dependent phonon-induced decoherence on image formation, we adopt the variational master equation formalism. An unwanted low-intensity circular ring arising from the dominance of the Laguerre–Gaussian beam tail over that of the super-Gaussian beam was found to degrade resolution. This artifact is effectively eliminated by employing Bessel-modulated truncated structured beams. Our numerical analysis further reveals that, at finite temperatures and low pulse areas, exciton–phonon interactions distort the image, whereas operation at higher pulse areas enters a decoupling regime that restores resolution. These findings highlight the potential protocol for achieving controllable and scalable nanoscale optical imaging.

In Chapter 5, we present an overall summary of the key findings from each research problem addressed in this thesis and outline several promising future directions that may be pursued based on the insights gained.

Indian Institute of Technology Guwahati

Contents

TH-3976_186121017

List of Figures

TH-3976_186121017

TH-3976_186121017

List of Tables

TH-3976_186121017

Chapter 1

Introduction

The study of light has been central to scientific inquiry for centuries. Early philosophical debates, dating back to ancient Greece and India, speculated on whether vision resulted from rays emitted by the eye or from light entering it. Ibn al-Haytham argued persuasively that vision occurs when light enters the eye from external sources, not via rays emitted by the eye [3]. Johannes Kepler recognized that the intensity of light diminishes with the square of the distance from its source, because light spreads over the growing surface area of a sphere, known as the inverse-square law of light intensity [4]. He also investigated reflection from flat and curved mirrors, demonstrating how images are formed and distinguishing between real and virtual images [5, 6]. Around the same time, Snellius discovered how light bends when crossing different media, called Snell's law of refraction [7, 8]. This formed the basis of modern lens design. In the 17th century, the nature of light was one of the most debated questions in physics. Huygens introduced his wave theory of light [9], where he imagined light as a disturbance spreading out in all directions, much like ripples on water. A few years later, Isaac Newton put forward the corpuscular theory [10], suggesting that light consists of tiny particles, or "corpuscles," emitted from luminous objects. Although Newton's particle theory was widely accepted in his time, the wave perspective gained strength in the 19th century with Thomas Young's double-slit experiment [11, 12], which demonstrated the interference and diffraction of light. James Clerk Maxwell's electromagnetic (EM) theory [13, 14] then unified electricity, magnetism, and optics into a single framework, establishing light as an electromagnetic wave. However, in the early 20th century, it was revealed that this classical description of light was incomplete. In 1900, Max Planck solved the mystery of blackbody radiation by proposing that energy is not emitted continuously but in discrete packets called "quanta" [15]. This idea, known as Planck's quantum hypothesis marked the foundation of quantum theory. After five years, Albert Einstein extended this by proposing that light itself consists of photons (quanta of light), explaining the photoelectric effect and proving that light has both wave and particle nature [16, 17]. This wave–particle duality gave birth to quantum optics—the study of light and its interaction with matter at the quantum level. Over the next two decades, pioneers like Niels Bohr, Werner Heisenberg, and Erwin Schrödinger developed quantum mechanics, providing powerful tools to describe the atom and the behavior of electrons. Paul Dirac quantized the electromagnetic field [18]. Feynman, Schwinger, and others established quantum electrodynamics (QED) [19, 20], the most precise theory of light and matter, which became the theoreti-

TH-3976_186121017

cal backbone of quantum optics. The invention of the laser in 1960 by Theodore Maiman provided a highly coherent and controllable source of light, enabling experimental tests of quantum theory that were previously unimaginable [21]. Phenomena such as coherent population trapping (CPT) [22], electromagnetically induced transparency (EIT) [23], Rabi oscillations [24], and squeezed states of light [25] highlight how quantum interference and coherence fundamentally alter the optical response of atomic and solid-state systems. Roy J. Glauber developed the quantum theory of optical coherence [26]. His work explained the fundamental difference between thermal light and laser light and laid the cornerstone for studying quantum states of light, such as coherent, squeezed, and entangled states. Later, researchers like Serge Haroche and David Wineland pushed the frontiers further, demonstrating exquisite control over single atoms and photons [27]. In modern times, quantum optics has become a cornerstone of quantum technologies, underpinning areas such as quantum communication, computation, and metrology [28, 29].

To study the radiation-matter interaction, usually two formalisms are adopted: semiclassical or fully quantum. This depends on the radiation, which is treated classically or quantum mechanically [30]. However, the atoms have their own discrete quantum levels. In this thesis, we have opted for the semiclassical formalism of light-matter interaction to study the optical properties of the medium. This chapter is dedicated to the theoretical foundation of our research work. It starts with the semiclassical description of electromagnetic radiation. We derive the propagation equation of light in both linear and nonlinear media. Next, we discuss the atom-field interaction in atomic systems. Subsequently, we introduce the basic formalism of the density matrix used in our thesis. Then we discuss the exciton-phonon interaction in quantum dots (QDs). We further explore the two and three-level atomic system interacting with the EM field. Next, we provide an overview of the principles of super-resolution microscopy and its significance. Finally, we introduce vector beams (VBs), along with their generation mechanisms and key applications.

1.1 Theoretical framework for electromagnetic wave propagation

The classical description of electromagnetic fields is fundamentally governed by Maxwell's equations, which provide a complete theoretical framework for describing the behavior of electric and magnetic fields in space and time. These equations provide the basis for classical electrodynamics. In the context of this work, Maxwell's equations are employed to derive the propagation equations for optical fields, which in turn allow us to understand beam evolution, coherence properties, and control mechanisms within atomic systems.

1.1.1 Maxwell's Equations

Maxwell's equations, comprising two scalar and two vector relations, provide a unified description of electricity, magnetism, and their interdependence [31]. In Gaussian units, the equations are written as

$$\vec{\nabla} \cdot \vec{D} = 4\pi\varrho, \qquad \text{(Gauss's Law)} \tag{1.1a}$$

$$\vec{\nabla} \cdot \vec{B} = 0, \tag{1.1b}$$

$$\vec{\nabla} \times \vec{E} = -\frac{1}{c}\frac{\partial \vec{B}}{\partial t}, \qquad \text{(Faraday's Law)} \tag{1.1c}$$

$$\vec{\nabla} \times \vec{H} = \frac{4\pi}{c}\vec{J} + \frac{1}{c}\frac{\partial \vec{D}}{\partial t}, \qquad \text{(Ampere's Law).} \tag{1.1d}$$

where $\vec{E}$, and $\vec{H}$ represent the electric and magnetic field at a given point in space and time ($\vec{r}$, t), and c is the speed of light in free space. The source terms ρ and $\vec{J}$ denote free charge density and current density, respectively. This source terms are the physical quantities that generate or influence the electromagnetic fields. Together, the equations form a set of four coupled, linear, partial differential equations. In addition, the electric displacement, $\vec{D}$ and the magnetic induction, $\vec{B}$ are related by

$$\vec{D} = \vec{E} + 4\pi\vec{P}, \tag{1.2a}$$

$$\vec{B} = \vec{H} + 4\pi\vec{\mathcal{M}}, \tag{1.2b}$$

where $\vec{P}$ and $\vec{\mathcal{M}}$ are the electric and magnetic polarization of the medium. In free space, both quantities are zero. In Eq. (1.2a) $\vec{P}$ represents only the electric dipole polarization, since at optical frequencies this term captures the essential physics of light–matter interaction. Higher multipole contributions are neglected because their effects are orders of magnitude weaker at optical frequencies. In this thesis, we have considered the system which is non-magnetic ($\vec{\mathcal{M}} = 0$), and non-conducting ($\vec{J} = 0$), with no free charge ($\rho = 0$). Now we want to derive the EM wave equation used in this thesis. Taking the curl of Eq. (1.1c), and using Eqs. (1.1d), (1.2a), and (1.2b) we get

$$\vec{\nabla} \times \left(\vec{\nabla} \times \vec{E}\right) + \frac{1}{c^2}\frac{\partial^2}{\partial t^2}(\vec{E} + 4\pi\vec{P}) = 0. \tag{1.3}$$

Using the vector identity, $\vec{\nabla} \times (\vec{\nabla} \times \vec{E}) = \vec{\nabla}(\vec{\nabla} \cdot \vec{E}) - \nabla^2\vec{E}$, Eq. (1.3) can be written as

$$\vec{\nabla}^2\vec{E} - \frac{1}{c^2}\frac{\partial^2\vec{E}}{\partial t^2} = \frac{4\pi}{c^2}\frac{\partial^2\vec{P}}{\partial t^2}. \tag{1.4}$$

The above second-order inhomogeneous differential wave equation comprises a source term on the right-hand side, representing the medium's response induced by the electric field $\vec{E}$. In free space, the source term is zero, which takes the form

$$\vec{\nabla}^2\vec{E} - \frac{1}{c^2}\frac{\partial^2\vec{E}}{\partial t^2} = 0. \tag{1.5}$$

As the optical wavelength is very small compared to the characteristic transverse scale, the field does not vary rapidly in the transverse direction compared to its variation in the direction of propagation. So, it becomes a 1D wave equation, which has the general solution of a standing wave as

$$\vec{E} = \vec{E_1}(z - ct) + \vec{E_2}(z + ct), \tag{1.6}$$

where $\vec{E_1}$, and $\vec{E_2}$ represent the forward and backward propagating wave, each traveling with speed c.

Now, in the presence of the source term, Eq. (1.4) denotes the propagation of EM wave inside a dielectric medium. However, the exact solution to this equation

is very difficult to obtain. But employing "slowly varying envelope approximation" (SVEA) it can be solved both analytically and numerically in principle. We consider a linearly polarized plane wave propagating in the z-direction through the dielectric medium, and its electric field can be defined as

$$\vec{E}(x,y,z,t) = \hat{e}\mathcal{E}(x,y,z,t)e^{-i(\omega t - kz)} + c.c., \tag{1.7}$$

where $\hat{e}$ is the unit polarization vector, $\mathcal{E}(x,y,z,t)$ is the envelope of the field, ω is the carrier angular frequency, and $k = \omega/c$ is the wave number. The complex conjugate ($c.c.$) ensures the field is real. The medium's polarization is the dipole moment per unit volume induced by the electric field. So, $\vec{P}$ must oscillate with the same carrier frequency ω, and wavevector k. The induced polarization is written as

$$\vec{P}(x,y,z,t) = \hat{e}\mathcal{P}(x,y,z,t)e^{-i(\omega t - kz)} + c.c., \tag{1.8}$$

Now to solve Eq. (1.4) we need to find the relevant derivatives, which are as follows:

$$\nabla^2\vec{E} = \hat{e}\left(\nabla_\perp^2\mathcal{E} + \frac{\partial^2\mathcal{E}}{\partial z^2} + 2ik\frac{\partial\mathcal{E}}{\partial z} - k^2\mathcal{E}\right)e^{i(kz-\omega t)} + c.c., \tag{1.9a}$$

$$\frac{\partial^2\vec{E}}{\partial t^2} = \hat{e}\left(\frac{\partial^2\mathcal{E}}{\partial t^2} - 2i\omega\frac{\partial\mathcal{E}}{\partial t} - \omega^2\mathcal{E}\right)e^{i(kz-\omega t)} + c.c., \tag{1.9b}$$

$$\frac{\partial^2\vec{P}}{\partial t^2} = \hat{e}\left(\frac{\partial^2\mathcal{P}}{\partial t^2} - 2i\omega\frac{\partial\mathcal{P}}{\partial t} - \omega^2\mathcal{P}\right)e^{i(kz-\omega t)} + c.c., \tag{1.9c}$$

where the Laplacian operator, $\nabla_\perp^2 = \partial^2/\partial x^2 + \partial^2/\partial y^2$ represents variation in the transverse direction. We assume that the variation in the envelope of electric field $\mathcal{E}$, and the polarization $\mathcal{P}$ with space and time is very small within the optical period and the wavelength. This approximation is known as SVEA [30] and is mathematically written as:

$$|k\mathcal{E}| \gg \left|k^2\frac{\partial\mathcal{E}}{\partial z}\right| \gg \left|\frac{\partial^2\mathcal{E}}{\partial z^2}\right|, \quad |\omega\mathcal{E}| \gg \left|\omega^2\frac{\partial\mathcal{E}}{\partial t}\right| \gg \left|\frac{\partial^2\mathcal{E}}{\partial t^2}\right|, \tag{1.10a}$$

$$|k\mathcal{P}| \gg \left|k^2\frac{\partial\mathcal{P}}{\partial z}\right| \gg \left|\frac{\partial^2\mathcal{P}}{\partial z^2}\right|, \quad |\omega\mathcal{P}| \gg \left|\omega^2\frac{\partial\mathcal{P}}{\partial t}\right| \gg \left|\frac{\partial^2\mathcal{P}}{\partial t^2}\right|. \tag{1.10b}$$

We substitute the relevant derivatives in Eq. (1.4), and by neglecting the second-order partial derivatives with respect to z and t, we get

$$\frac{1}{2ik}\nabla_\perp^2\mathcal{E} + \frac{\partial\mathcal{E}}{\partial z} + \frac{1}{c}\frac{\partial\mathcal{E}}{\partial t} = 2\pi ik\mathcal{P}. \tag{1.11}$$

Note that the solution of the form in Eq. (1.6) cannot be the solution of Eq. (1.11). Now, to make the numerical calculation easier, we consider a frame of reference moving at the speed of light, c in vacuum. The transformations look like:

$$\tau = t - z/c, \quad \zeta = z, \tag{1.12}$$

so we get

$$\partial/\partial z + c^{-1}\partial/\partial t = \partial/\partial\zeta, \quad \partial/\partial t = \partial/\partial\tau. \tag{1.13}$$

Substituting in Eq. (1.11) we get

$$\frac{1}{2ik}\nabla_{\perp}^{2}\mathcal{E}+\frac{\partial\mathcal{E}}{\partial\zeta}=2\pi ik\mathcal{P}. \tag{1.14}$$

The above form of the wave equation is known as the "paraxial wave equation". Now, in case of a laser pulse, the transverse variation of the field envelop is connsidered to be very small in comparison to the variation in z and t. Therefore we can ignore the first term in the left-hand side of the Eq. (1.14) for which the propagation equation for a light pulse reduces to

$$\frac{\partial\mathcal{E}}{\partial z}+\frac{1}{c}\frac{\partial\mathcal{E}}{\partial t}=2\pi ik\mathcal{P}. \tag{1.15}$$

On the other hand, for a continuous wave (CW) quasi-monochromatic beam, the slowly varying envelope does not vary with time, *i.e.* $\partial\mathcal{E}/\partial t=0$. Hence, the propagation equation for a light beam is given as

$$\frac{\partial\mathcal{E}}{\partial z}=\frac{i}{2k}\nabla_{\perp}^{2}\mathcal{E}+2\pi ik\mathcal{P}. \tag{1.16}$$

In the above equation, the first term on the right-hand side is accountable for diffraction and the second term represents absorption and dispersion of the light beam. The induced polarization can be calculated from the optical Bloch equation, which we will discuss later in this chapter.

1.1.2 Nonlinear polarization

The EM field itself induces the polarization of an atomic gas that does not have permanent polarization. Therefore the input field drives the polarization and vice versa. The response of a dielectric medium to an intense EM field, such as that produced by lasers, is generally nonlinear in the field amplitude. Physically, this arises because the electrons bound within atoms or molecules do not behave as perfect harmonic oscillators when subjected to strong fields. Instead, their motion becomes anharmonic [32]. In the most general case, for a monochromatic EM wave, the polarization can be expressed as a nonlinear function of the electric field:

$$\vec{P}(\vec{r},t)=\vec{P}^{(1)}(\vec{r},t)+\vec{P}^{(2)}(\vec{r},t)+\vec{P}^{(3)}(\vec{r},t)+\cdots, \tag{1.17}$$

where the linear and the nonlinear polarization can be written as

$$\vec{P}_{L}(\vec{r},t)=\vec{P}^{(1)}(\vec{r},t), \tag{1.18a}$$

$$\vec{P}_{NL}(\vec{r},t)=\vec{P}^{(2)}(\vec{r},t)+\vec{P}^{(3)}(\vec{r},t)+\cdots, \tag{1.18b}$$

The linear order is associated with the second rank susceptibility tensor. Similarly, the second-order polarization is associated with the third rank susceptibility tensor and so on. This can be represented as

$$P_{j}^{(1)}=\sum_{k}\chi_{jk}^{(1)}E_{k}, \tag{1.19a}$$

$$P_{j}^{(2)}=\sum_{k,l}\chi_{jkl}^{(2)}E_{k}E_{l}, \tag{1.19b}$$

$$P_{j}^{(3)}=\sum_{k,l,m}\chi_{jklm}^{(3)}E_{k}E_{l}E_{m}. \tag{1.19c}$$

In the above equation, P_j denotes the components of the polarization vector, also $\chi^{(1)}_{jk}$, $\chi^{(2)}_{jkl}$, and $\chi^{(3)}_{jklm}$ represent second, third, and fourth rank susceptibility tensor respectively with $j, k, l, m \in x, y, z$. Therefore, the susceptibility maps the electric field components to the corresponding polarization component. It is important to note that for centrosymmetric media, the even-order nonlinear effects are forbidden, because the medium's inversion symmetry cancels out these contributions. Therefore, the third-order nonlinear term becomes the lowest-order nonlinear effect in centrosymmetric media. This third-order polarization gives rise to important phenomena such as the Kerr effect [33], self-phase and cross-phase modulation [34], third-harmonic generation (THG), and four-wave mixing (FWM) [32, 35].

Now we are interested in deriving an analytical expression for the critical intensity of a beam for which self-focusing or cross-Kerr induced focusing would be prominent. It is evident from Eq. (1.16) that if diffraction is neglected, the nonlinear phase build-up from an input boundary at $z = 0$ is [36]

$$\Phi_{NL} = \left(\frac{2\pi\omega z}{c}\right) \mathrm{Re}\left[\chi^{(3)}\right] |\mathcal{E}|^2, \tag{1.20}$$

where ω is the carrier frequency of the beam. The nonlinear distance is defined by setting the phase deviation across the beam $\Phi_{NL} = 1$, so that

$$z_{NL} = \left(\frac{c}{2\pi\omega}\right) \frac{1}{\mathrm{Re}\left[\chi^{(3)}\right] |\mathcal{E}|^2}. \tag{1.21}$$

Also from the wave equation, for a beam of waist w_0, we can define the a characteristic distance for diffraction as

$$z_{DIF} = \left(\frac{\pi w_0^2 n_0}{\lambda}\right), \tag{1.22}$$

where n_0 is the linear refractive index and λ corresponds to the wavelength of the light beam. If $z_{DIF} \ll z_{NL}$, then the beam will be affected by the diffraction much earlier than the nonlinear effect, so it will just diffract without any nonlinear behavior. For $z_{DIF} \gg z_{NL}$, the nonlinear effect will be more evident than diffraction and because of self-Kerr or cross-Kerr modulation, the beam will tend to focus. Further, for $z_{DIF} \approx z_{NL}$, the two effects balance each other, which give us soliton solutions. So, equating the two distances, we can find the critical intensity for focusing as

$$|\mathcal{E}|^2 \approx \left(\frac{\lambda^2}{4\pi^3 w_0^2 n_0 \mathrm{Re}\left[\chi^{(3)}\right]}\right). \tag{1.23}$$

In the above equation, $\mathrm{Re}\left[\chi^{(3)}\right]$ is proportional to the nonlinear refractive index of the medium. A positive value of the nonlinear refractive index gives rise to the Kerr effect, in which the refractive index of a medium increases with optical beam intensity. This leads to key nonlinear effects such as self-focusing, and cross-Kerr focusing.

1.2 Atom-field interaction

In the semiclassical theory of light–matter interaction, the atom is treated as a quantum mechanical system while the EM field is considered as a classical wave. Our

goal is to obtain a Hamiltonian that describes how the atomic degrees of freedom couple to the applied optical field. We start from the minimal-coupling prescription in electrodynamics, where the charged particles inside the atom (electrons) interact with the electromagnetic potentials through their kinetic momentum. For simplicity, and in particular for hydrogen-like and alkali atoms, we adopt the single active electron (SAE) approximation, where the atomic core provides an effective central potential and only the outer electron couples strongly to the external field. Using this framework, and under suitable approximations such as the dipole approximation, one can derive the familiar form of the atom–field interaction Hamiltonian that serves as the foundation for semiclassical optical Bloch equations.

An electron with charge -e, and mass m, moving through an electric field $\vec{E}$ and magnetic field $\vec{B}$ with a velocity $\vec{v}$ experiences the Lorentz force $\vec{F} = -e(\vec{E} + (\vec{v} \times \vec{B})/c)$ [31, 37]. Since the electric and magnetic fields themselves are not the most fundamental quantities but can be derived from more basic functions known as the scalar potential ϕ and vector potential $\vec{A}$ as

$$\vec{E}(\vec{r},t) = -\vec{\nabla}\phi(\vec{r},t) - \frac{1}{c}\frac{\partial}{\partial t}\vec{A}(\vec{r},t), \tag{1.24}$$

$$\vec{B}(\vec{r},t) = \vec{\nabla} \times \vec{A}(\vec{r},t). \tag{1.25}$$

By expressing the EM fields in terms of the scalar and vector potentials and applying the Euler–Lagrange formalism, we can obtain the Lagrangian for an electron in an EM field as

$$L(\vec{r},\dot{r},t) = \tfrac{1}{2}m\dot{\vec{r}}^2 + e\phi(\vec{r},t) - \left(\frac{e}{c}\right)\dot{\vec{r}} \cdot \vec{A}(\vec{r},t), \tag{1.26}$$

which consistently reproduces the Lorentz force. The single active electron is also bound by the central Coulomb potential $V(r)$ due to the nucleus. Now, the Hamiltonian can be obtained from the Lagrangian in Eq. (1.26) by using the Legendre transformation, and can be written as

$$\mathcal{H} = \frac{1}{2m}\left[\vec{p} + \frac{e}{c}\vec{A}(\vec{r},t)\right]^2 - e\phi(\vec{r},t) + V(r), \tag{1.27}$$

where $\vec{p}$ is the canonical momentum. The quantization of the electron's motion is achieved by replacing classical variables with the corresponding quantum operators as, $\vec{p} \to -i\hbar\vec{\nabla}$, and $E \to i\hbar\partial/\partial t$ respectively. Here, $\hbar = h/2\pi$, where h is the Planck constant. The Hamitonian for the electron bound by the Coulomb potential is then given by

$$H = -\frac{\hbar^2}{2m}\nabla^2 + V(r). \tag{1.28}$$

Thus, the motion of an electron is governed by the non-relativistic Schrödinger equation as

$$\begin{aligned} i\hbar\frac{\partial}{\partial t}\Psi(\vec{r},t) &= H\Psi \\ &= \left[\frac{-\hbar^2}{2m_e}\nabla^2 + V(r)\right]\Psi(\vec{r},t), \end{aligned} \tag{1.29}$$

where $\Psi(\vec{r},t)$ denotes the wave function of the quantum system, and $|\Psi(\vec{r},t)|^2$ gives the probability density of finding the electron at position $\vec{r}$ and time t. The general solution of Eq. (1.29) is given by

$$\Psi(\vec{r},t) = \psi(\vec{r},t)\exp\left[i\chi\right], \tag{1.30}$$

where χ is an arbitrary scalar function and does not influence the probability density. The constant phase factor represents the same physical state. However, if the phase depends on both space and time, the solution becomes

$$\Psi(\vec{r},t) = \psi(\vec{r},t)\exp\left[i\chi(\vec{r},t)\right]. \tag{1.31}$$

The above solution does not satisfy the Schrödinger equation as in Eq. (1.29) but the probability density remains invariant. Therefore to satisfy the local gauge invariance we need to include the scalar and vector potential in the Hamiltonian as

$$i\hbar\frac{\partial}{\partial t}\Psi(\vec{r},t) = \left\{\frac{1}{2m}\left[-i\hbar\vec{\nabla} + \frac{e}{c}\vec{A}(\vec{r},t)\right]^2 - e\phi(\vec{r},t) + V(\vec{r})\right\}\Psi(\vec{r},t). \tag{1.32}$$

It is important to note that the scalar potential ϕ, and the vector potential $\vec{A}$ are not unique. There is a whole family of the potentials that describe the same physical fields. In order to make Eq. (1.32) invariant under the transformation as in Eq. (1.31) we need to replace ϕ, and $\vec{A}$ by their gauge transformations as

$$\vec{A}(\vec{r},t) \rightarrow \vec{A}'(\vec{r},t) = \vec{A}(\vec{r},t) - \frac{\hbar c}{e}\vec{\nabla}\chi(\vec{r},t), \tag{1.33}$$

$$\phi(\vec{r},t) \rightarrow \phi'(\vec{r},t) = \phi(\vec{r},t) + \frac{\hbar}{e}\frac{\partial\chi(\vec{r},t)}{\partial t}. \tag{1.34}$$

Under the above transformation the electric field and the magnetic field remain invariant. We can further simplify the Hamiltonian in Eq. (1.32) by considering the Coulomb or radiation gauge condition which is given by $\phi(\vec{r},t) = 0$ and $\vec{\nabla}\cdot\vec{A}(\vec{r},t) = 0$. Hence, the modified Hamiltonian takes the form

$$H = -\frac{\hbar^2}{2m}\nabla^2 - \frac{ie\hbar}{2mc}\vec{A}(\vec{r},t)\cdot\vec{\nabla} + \frac{e^2}{2mc^2}\vec{A}(\vec{r},t)\cdot\vec{A}(\vec{r},t) + V(r). \tag{1.35}$$

The Coulomb gauge condition separates the instantaneous Coulomb interaction (responsible for binding the electron in the atom) from the transverse radiation field [30, 38, 39]. This separation makes it straightforward to derive the familiar dipole interaction Hamiltonian. In contrast, gauges like the Lorentz gauge tend to mix longitudinal and transverse fields, making it less transparent to distinguish between the bound atomic potential and the external radiation.

1.2.1 Electric dipole approximation

We consider the problem of a bound electron and its dynamics in the presence of an incident plane EM wave. The plane EM wave can be described by the vector potential $\vec{A}(\vec{r},t)$ as

$$\vec{A}(\vec{r}_0+\vec{r},t) = \vec{A}(t)\exp\left[i\vec{k}\cdot(\vec{r}_0+\vec{r})\right] \tag{1.36}$$

where $\vec{r}_0$ is the location of the nucleus. We assume that the wavelength of the EM field is much greater than the characteristic size of the atom, which is on the order of the Bohr radius. Consequently, the spatial variation of the field can be regarded as essentially uniform across the atomic dimensions. Within this approximation, $\vec{k}\cdot\vec{r} \ll 1$, where $|k| = 2\pi/\lambda$ is the wavevector and λ is the wavelength of the EM wave. Therefore, the vector potential is simplified to

$$\begin{aligned}\vec{A}(\vec{r}_0+\vec{r},t) &= \vec{A}(t)\exp\left[i\vec{k}\cdot(\vec{r}_0+\vec{r})\right] \\ &= \vec{A}(t)\exp\left(i\vec{k}\cdot\vec{r}_0\right)\left[1+i\vec{k}\cdot\vec{r}+\cdots\right] \\ &\approx \vec{A}(t)\exp\left(i\vec{k}\cdot\vec{r}_0\right). \end{aligned} \tag{1.37}$$

So we can consider a spatially uniform vector potential using the "electric dipole approximation". Using this approximation, the Hamiltonian takes the form

$$H = -\frac{\hbar^2}{2m}\nabla^2 + V(r) - \frac{ie\hbar}{2mc}\vec{A}(\vec{r}_0,t)\cdot\vec{\nabla} + \frac{e^2}{2mc^2}A^2(\vec{r}_0,t). \tag{1.38}$$

We now make a gauge transformation as $\chi(\vec{r},t) = (-e/\hbar c)\vec{A}(r_0,t)\cdot\vec{r}$. Under this transformation the wave function $\Psi(\vec{r},t)$ looks like

$$\Psi(\vec{r},t) = \exp\left[\frac{-ie}{\hbar c}\vec{A}(\vec{r}_0,t)\cdot\vec{r}\right]\psi(\vec{r},t). \tag{1.39}$$

Now substituting Eq. (1.38), and Eq. (1.39) in Eq. (1.29) we get

$$\left[i\hbar\frac{\partial}{\partial t} + \frac{e}{c}\frac{\partial\vec{A}(\vec{r}_0,t)}{\partial t}\cdot\vec{r}\right]\psi(\vec{r},t) = \left[\frac{-\hbar^2}{2m_e}\nabla^2 + V(r)\right]\psi(\vec{r},t). \tag{1.40}$$

The electric field at $\vec{r}_0$, and time t can be represented using the Coulomb gauge as $\vec{E}(\vec{r}_0,t) = -\frac{1}{c}\frac{\partial}{\partial t}\vec{A}(\vec{r}_0,t)$. We substitute this relation in Eq. (1.40) and find the simplified version as

$$\begin{aligned} i\hbar\frac{\partial}{\partial t}\psi(\vec{r},t) &= \left\{-\frac{\hbar^2}{2m}\nabla^2 + V(r) + e\vec{r}\cdot\vec{E}(\vec{r}_0,t)\right\}\psi(\vec{r},t) \\ &= (H_0+H_I)\psi(\vec{r},t), \end{aligned} \tag{1.41}$$

where H_0, and H_I correspond to the bare and interaction Hamiltonian. In terms of the dipole moment operator $\vec{d} = -e\vec{r}$ the interaction Hamiltonian can be written as

$$H_I = -\vec{d}\cdot\vec{E}. \tag{1.42}$$

We have used this above Hamiltonian to describe the atom-field interaction in the semiclassical picture throughout this thesis.

1.3 Density matrix formalism

In quantum mechanics, the state of a system is represented by a wavefunction ψ, which contains complete information about the system. But in many real situations,

we do not have complete information about the system. For instance, in an atomic vapour, we typically deal with a large ensemble containing an enormous number of identical atoms. The situation gets cumbersome in the presence of incoherent processes, such as damping due to radiative and non-radiative processes. The wave-function formalism does not provide a complete description of the system. Therefore, the density matrix formalism becomes necessary to include statistical mixtures and decoherence in the system [40]. The density matrix operator is defined as

$$\rho = \sum_j p_j |\psi_j\rangle\langle\psi_j|, \tag{1.43}$$

where p_j is the classical probability of being in state $|\psi_j\rangle$. The conservation of probability suggests $\sum_j p_j = 1$. Depending on the amount of information we possess about a system, it can be classified as either pure or mixed state. A system being in a definite quantum state $|\psi\rangle$, the corresponding density matrix for a pure state is $\rho = |\psi\rangle\langle\psi|$. For a pure state, the density matrix satisfies $\rho^2 = 1$, and $Tr(\rho^2) = Tr(\rho) = 1$. In contrast, a mixed state arises when the system is represented by a statistical mixture of several pure states, each occurring with a certain probability. In this case, $\rho^2 \neq \rho$, and $Tr(\rho^2) < 1$. We now want to discuss the expectation value of a quantum mechanical operator $\mathcal{O}$ using density matrix. The expectation value can be written as

$$\begin{aligned}
\langle\mathcal{O}\rangle &= \sum_j p_j \langle\psi_j|\mathcal{O}|\psi_j\rangle, \\
&= \sum_j p_j \sum_n \langle\psi_j|\mathcal{O}|n\rangle\langle n|\psi_j\rangle \quad \left(\text{As}, \sum_n |n\rangle\langle n| = 1\right), \\
&= \sum_n \sum_j p_j \langle n|\psi_j\rangle\langle\psi_j|\mathcal{O}|n\rangle = \sum_n \langle n| \sum_j p_j |\psi_j\rangle\langle\psi_j|\mathcal{O}|n\rangle = \sum_n \langle n|\rho\mathcal{O}|n\rangle, \\
&= Tr\left[\rho\mathcal{O}\right].
\end{aligned} \tag{1.44}$$

So, by using Eq. (1.44) we can get the expectation value using the density matrix formalism for both pure and mixed quantum states.

Now we will be deriving the equation of motion using the density matrix. The time evolution of a system denoted as a wavefunction ψ_j can be obtained by Schrödinger equation as

$$\frac{\partial|\psi_j\rangle}{\partial t} = -\frac{i}{\hbar} H|\psi_j\rangle. \tag{1.45}$$

Also, the time evolution of the density matrix is expressed as

$$\begin{aligned}
\dot{\rho} &= \sum_j p_j \left(|\dot{\psi}\rangle\langle\psi| + |\psi\rangle\langle\dot{\psi}|\right), \\
&= -\frac{i}{\hbar} \sum_j p_j \left(H|\psi_j\rangle\langle\psi_j| - \psi_j\rangle\langle\psi_j|H\right), \\
&= -\frac{i}{\hbar}\left(H\rho - \rho H\right) = -\frac{i}{\hbar}\left[H, \rho\right].
\end{aligned} \tag{1.46}$$

The above Eq. (1.46) is known as the Liouville or Von Neumann equation. It generalizes the Schrödinger equation to ensembles of particles and tells us how quantum states evolve in time when expressed in terms of the density operator. However, real physical systems like atomic vapours suffer from incoherent processes such as spontaneous emission, dephasing (collisional or thermal), optical pumping, relaxation due to phonons or environment. So we can modify the Liouville equation by including additional relaxation and decoherence terms as

$$\dot{\rho} = -\frac{i}{\hbar}\left[H, \rho\right] + \frac{\gamma}{2}\mathcal{L}\left[\sigma^{-}\right]\rho, \tag{1.47}$$

where $\sigma^{-} = |0\rangle\langle 1|$, γ is the spontaneous decay rate, and the Lindblad superoperator acting on a operator $\mathcal{O}$ is defined by, $\mathcal{L}\left[\mathcal{O}\right] = 2\mathcal{O}\rho\mathcal{O}^{\dagger} - \mathcal{O}^{\dagger}\mathcal{O}\rho - \rho\mathcal{O}^{\dagger}\mathcal{O}$. The above Eq. (1.47) is known as Lindblad master equation [41].The second term on the right hand side of Eq. (1.47) incorporates all the incoherent processes of the system.

1.4 Exciton-phonon interaction in quantum dot

Although quantum effects are often associated with single atoms or subatomic particles, these phenomena can also appear in much larger systems, containing large number of atoms (more than 10^4) [42]. In semiconductor materials, the band structure allows to create regions where charge carriers electrons and holes are spatially confined. By combining two different semiconductor materials with different bandgaps, a potential well can be formed that traps these carriers within a limited region of space. Depending on the number of confined dimensions, different nanostructures are realized. Quantum wells provide confinement in one dimension, quantum wires confine carriers in two dimensions, and QDs confine carriers in all three spatial dimensions, leading to discrete atom-like energy levels. According to their properties and preparation techniques, it can be classified into three types: colloidal QDs [43], self-assembled QDs [44], and electrochemically or ion-implanted QDs [45]. Among these, self-assembled QDs yield high optical and electronic quality suitable for quantum devices.

In semiconducting and ionic solids, the movement of charge carriers (electrons and holes) is strongly influenced by their interaction with the crystal lattice vibrations, known as phonons. The excitation makes the electron transition from the valance band to the conduction band and modifies the charge configuration [46, 47]. Therefore the change in the equilibrium position of the lattice ions gives rise to coupling between the exciton and phonons. The electron–phonon interaction is crucial for understanding QD dynamics because it directly influences how charge carriers relax, and lose coherence inside the dot. We consider the electron is at $\vec{r}_j$ and the ion is at a position $\vec{R}_m = \vec{R}_m^{(0)} + \vec{Q}_m$, where $\vec{R}_m^{(0)}$, and $\vec{Q}_m$ are the equilibrium position and small displacement of the ion, respectively. So, the interaction Hamiltonian can be written as

$$H_{ei} = \sum_{jm} V_{ei}\left(\vec{r}_j - \vec{R}_m^{(0)} - \vec{Q}_m\right). \tag{1.48}$$

As the displacements are usually small we can Taylor expand the potential as

$$V_{ei}\left(\vec{r}_j - \vec{R}_m^{(0)} - \vec{Q}_m\right) = V_{ei}\left(\vec{r}_j - \vec{R}_m^{(0)}\right) - \vec{Q}_m \cdot \nabla V_{ei}\left(\vec{r}_j - \vec{R}_m^{(0)}\right) + \mathcal{O}\left(\vec{Q}_m^2\right). \tag{1.49}$$

The first term on the right-hand side of Eq. (1.49) corresponds to the periodic potential for the electron in the unperturbed lattice. Since this potential is already accounted for in the unperturbed Hamiltonian used to construct the excitonic basis, we do not need to consider further. The second term describes the linear electron-phonon interaction due to the ion displacement.

$$V_{ep}(\vec{r}) = -\sum_m \vec{Q}_m \cdot \nabla V_{ei}\left(\vec{r} - \vec{R}_m^{(0)}\right). \tag{1.50}$$

If we take the Fourier transformation of the potential, it looks like

$$V_{ei}(\vec{r}) = \frac{1}{N}\sum_{\vec{q}} V(\vec{q}) e^{i\vec{q}\cdot\vec{r}}. \tag{1.51}$$

So, now Eq. (1.50) can be written as

$$\begin{aligned} V_{ep}(\vec{r}_j) &= -\frac{i}{N}\sum_{\vec{q}}\sum_m \vec{Q}_m e^{-i\vec{q}\cdot\vec{R}_m^{(0)}} \cdot \vec{q}\, V(\vec{q}) e^{i\vec{q}\cdot\vec{r}} \\ &= -\frac{i}{\sqrt{N}}\sum_{\vec{q}} \vec{Q}_{\vec{q}} \cdot \vec{q}\, V(\vec{q}) e^{i\vec{q}\cdot\vec{r}}, \end{aligned} \tag{1.52}$$

where $\vec{Q}_{\vec{q}} = \sum_m \vec{Q}_m e^{-i\vec{q}\cdot\vec{R}_m^{(0)}}/\sqrt{N}$. The wave vector $\vec{q}$ runs all over the space, but we consider the low-energy excitation in our system only couple the states within the first Brillouin zone, and thus simply replace $\vec{q}$ by $\vec{k}$. We can relate through the reciprocal lattice vector $\vec{G}$. The displacement operator $\vec{Q}_{\vec{k}}$ can be written in terms of the phonon creation and annihilation operator like $\vec{Q}_{\vec{k}} = (i/\sqrt{2m\hbar\omega_{\vec{k}}})\left(b_{\vec{k}} + b^\dagger_{-\vec{k}}\right)$, where m is the mass of the ions. By putting these in Eq. (1.52) we get

$$V_{ep}(\vec{r}_j) = \sum_{\vec{k}} \sqrt{\frac{\hbar}{2mN\omega_{\vec{k}}}}\vec{k}\, V(\vec{k}) e^{i\vec{k}\cdot\vec{r}}\left(b_{\vec{k}} + b^\dagger_{-\vec{k}}\right). \tag{1.53}$$

Now the total Hamiltonian for the electron-phonon interaction can be obtained by integrating over the charge density of the solid as

$$\begin{aligned} H_{ep} &= \int d^3r \rho(\vec{r}) V_{ep}(\vec{r}) \\ &= \sum_{\vec{k}} \vec{M}_{\vec{k}} \rho(\vec{k})\left(b_{\vec{k}} + b^\dagger_{-\vec{k}}\right), \end{aligned} \tag{1.54}$$

where $\rho(\vec{k}) = \int d^3r \rho(\vec{r}) e^{i\vec{k}\cdot\vec{r}}$ and $\vec{M}_{\vec{k}} = \vec{k}V(\vec{k})\sqrt{\hbar}/\sqrt{2mN\omega_{\vec{k}}}$. There are mainly three types of electron–phonon interactions occur in solid-state systems [48]. They are, deformation potential coupling, piezoelectric coupling, and polar (Fröhlich) coupling. For arsenide semiconductor QDs such as GaAs, and InAs both deformation potential and piezoelectric coupling can exist. However, the effect of piezoelectric fields is almost canceled when the electron and hole wavefunctions overlap significantly. So, phenomenologically, the deformation potential can be considered by replacing $\vec{k}$ by experimentally determined constants D_c and D_v for conduction and valence band, respectively.

1.4.1 Phonon spectral density

The phonon spectral density describes how strongly a system couples to phonons of different frequencies. We consider a two-level QD system with ground state $|0\rangle$ and the excited state $|1\rangle$. The total charge density of the system can be written as

$$\rho(\vec{k}) = \frac{I}{2}\left(\rho_{00}(\vec{k}) + \rho_{11}(\vec{k})\right) + \frac{\sigma_z}{2}\left(\rho_{11}(\vec{k}) - \rho_{00}(\vec{k})\right), \tag{1.55}$$

where I, and σ_z are the identity operator and the z-component of the Pauli spin matrix. As the first term on the right-hand side of Eq. (1.55) corresponds to a constant shift in the density, we can ignore that term. Now, putting the total charge density in Eq. (1.54) we get

$$H_{ep} = \sigma_z \sum_{\vec{k}} \vec{M}_{\vec{k}} \left(b_{\vec{k}} + b^{\dagger}_{-\vec{k}}\right),$$
$$\vec{M}_{\vec{k}} = \sqrt{\frac{\hbar}{2mN\omega_{\vec{k}}}}|\vec{k}|(D_c\rho_{11}(\vec{k}) - D_v\rho_{00}(\vec{k})). \tag{1.56}$$

By assuming spherically symmetric parabolic potential for both valence and conduction band we can write the QD wavefunction as [49]

$$\psi_j(\vec{r}) = \left(d_j\sqrt{\pi}\right)^{-3/2} e^{-\frac{r^2}{2d_j^2}}, \tag{1.57}$$

where $j \in 0, 1$, d_j correspond to the size of the wavefunction. Therefore, the charge density can we written as

$$\rho_{jj}(\vec{k}) = \int d^3r |\psi_j(\vec{r})|^2 e^{i\vec{k}\cdot\vec{r}}. \tag{1.58}$$

We can now use Eqs. (1.57), and (1.58) in Eq. (1.56) and by solving the integration we get

$$\vec{M}_{\vec{k}} = \sqrt{\frac{\hbar}{2mN\omega_{\vec{k}}}}|\vec{k}| \left(D_c e^{-\frac{k^2 d_1^2}{4}} - D_v e^{-\frac{k^2 d_0^2}{4}} \right). \tag{1.59}$$

The phonon spectral density is defined as

$$J_{ph}(\omega) = \sum_{\vec{k}} M_{\vec{k}}^2 \, \delta(\omega - \omega_{\vec{k}}). \tag{1.60}$$

For simplicity, we can take $d_0 = d_1 = d$, which describes the spherically symmetric QD. Converting the summantion over $\vec{k}$ into the integral and assuming the linear dispersion $\omega_{\vec{k}} = c\vec{k}$ we get

$$J_{ph}(\omega) = \alpha\omega^3 e^{-\frac{\omega^2}{\omega_c^2}}, \tag{1.61}$$

where $\alpha = V(D_c - D_v)^5\hbar/4\pi^2 mNc^5$ is the electron-phonon coupling strength, and $\omega_c = \sqrt{2}c/d$ denotes the phonon cutoff frequency, respectively.

1.5 Two level atomic system

In this section we discuss the interaction of a single electromagnetic field with a two-level atomic system. A two-level atomic system is the simplest model used to describe the light-matter interaction. In reality, atoms possess many energy levels and cannot

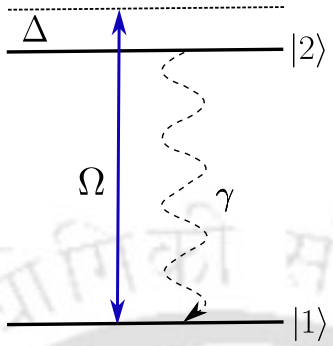

Figure 1.1: Schematic diagram of a two-level atomic system. The ground state $|1\rangle$ and the excited state $|2\rangle$ is coupled by a EM field with Rabi frequency Ω and detuning Δ. The spontaneous decay rate of the excited state is γ.

be strictly treated as two-level systems. However, when an external radiation field interacts resonantly or nearly resonantly with a particular pair of energy states, and all other states are far detuned, the atom's behavior can be effectively described using a two-level model [50]. We consider a two-level atomic system consisting of a ground state $|1\rangle$ and an excited state $|2\rangle$ as in Fig. 1.1. The two states are coupled by a plane monochromatic laser field defined as

$$\vec{E}(\vec{r},t) = \hat{e}\mathcal{E}(\vec{r})e^{i(\vec{k}\cdot\vec{r}-\omega t)} + c.c., \tag{1.62}$$

where $\hat{e}$, $\mathcal{E}(\vec{r})$, $\vec{k}$, and ω are the unit polarization vector, spatial envelop, wavevector and carrier frequency respectively. The Hamiltonian of the system in the absence of the external EM field can be written as

$$\begin{aligned} H_0 &= \hbar\omega_1|1\rangle\langle 1| + \hbar\omega_2|2\rangle\langle 2|, \\ &= \hbar\omega_{21}|2\rangle\langle 2|, \end{aligned} \tag{1.63}$$

where $\hbar\omega_1$, and $\hbar\omega_2$ are the energy eigenvalues of the states $|1\rangle$ and $|2\rangle$ respectively. We have considered the ground state energy as zero. Therefore, $\omega_{21} = \omega_2 - \omega_1$ denotes the transition frequency for the two-level system. The interaction Hamiltonian can be expressed as

$$\begin{aligned} H_I &= -\hat{d}\cdot\vec{E} \\ &= -(\vec{d}_{12}|1\rangle\langle 2| + \vec{d}_{21}|2\rangle\langle 1|)\cdot\vec{E}, \\ &= -\left[\vec{d}_{12}\cdot\hat{e}\mathcal{E}(\vec{r})e^{i(\vec{k}\cdot\vec{r}-\omega t)} + \vec{d}_{12}\cdot\hat{e}\mathcal{E}^*(\vec{r})e^{-i(\vec{k}\cdot\vec{r}-\omega t)}\right]|1\rangle\langle 2|, \\ &\quad -\left[\vec{d}_{21}\cdot\hat{e}\mathcal{E}(\vec{r})e^{i(\vec{k}\cdot\vec{r}-\omega t)} + \vec{d}_{21}\cdot\hat{e}\mathcal{E}^*(\vec{r})e^{-i(\vec{k}\cdot\vec{r}-\omega t)}\right]|2\rangle\langle 1|, \end{aligned} \tag{1.64}$$

where $\vec{d}_{12}$, and $\vec{d}_{21}$ are the matrix element of the induced dipole moment for the transition $|1\rangle \leftrightarrow |2\rangle$. The diagonal element $\vec{d}_{11}$, and $\vec{d}_{22}$ are zero as dipole moment

operator has odd parity, and therefore the matrix element of the dipole operator will be nonzero if $|1\rangle$ and $|2\rangle$ has different parity. The symbol '$*$' denotes complex conjugate. We define the Rabi frequency as

$$\Omega = \frac{\vec{d}_{21}\cdot\hat{e}}{\hbar}\mathcal{E}(\vec{r})e^{i\vec{k}\cdot\vec{r}}, \text{and} \quad \tilde{\Omega} = \frac{\vec{d}_{21}\cdot\hat{e}}{\hbar}\mathcal{E}^*(\vec{r})e^{-i\vec{k}\cdot\vec{r}}. \tag{1.65}$$

So now, the total Hamiltonian of the two-level atomic system can be written as

$$\begin{aligned} H &= H_0 + H_I \\ &= \hbar\omega_{21}|2\rangle\langle 2| - \hbar\left[\Omega e^{-i\omega t} + \tilde{\Omega}e^{i\omega t}\right]|2\rangle\langle 1| - \hbar\left[\tilde{\Omega}^* e^{-i\omega t} + \Omega^* e^{i\omega t}\right]|1\rangle\langle 2| \end{aligned} \tag{1.66}$$

The state vector $|\psi\rangle$ of a two-level atomic system can be written as

$$|\psi\rangle = c_1|1\rangle + c_2|2\rangle, \tag{1.67}$$

where $c_j (j = 1, 2)$ represents the probability amplitude of being in state $|j\rangle$. To remove the explicit time dependence in the Hamiltonian, as in Eq. (1.66) we use the following unitary transformation

$$\begin{aligned} |\psi(t)\rangle &= U|\phi(t)\rangle, \\ &= e^{-i\omega t|1\rangle\langle 1|}|\phi(t)\rangle. \end{aligned} \tag{1.68}$$

So the Schrödinger equation can be written as

$$i\hbar\frac{\partial|\phi(t)\rangle}{\partial t} = \mathcal{H}|\phi(t)\rangle, \tag{1.69}$$

where $\mathcal{H}$ is the effective Hamiltonian and is given as $\mathcal{H} = U^\dagger H U - i\hbar\partial_t U$ which simplifies Eq. (1.66) to

$$\mathcal{H} = -\hbar\Delta|2\rangle\langle 2| - \hbar\left[\Omega + \tilde{\Omega}e^{2i\omega t}\right]|2\rangle\langle 1| - \hbar\left[\Omega^* + \tilde{\Omega}^* e^{-2i\omega t}\right]|1\rangle\langle 2|, \tag{1.70}$$

where $\Delta = \omega - \omega_{12}$ is the detuning of the external field from the atomic transition frequency. In Eq. (1.70) $\tilde{\Omega}$, and $\tilde{\Omega}^*$ are associated with the highly oscillating terms with frequency $\pm 2\omega$ which contribute to the $\mathcal{H}$ only when $\tilde{\Omega} \approx 2\omega$. In the optical frequency domain where $\tilde{\Omega} \ll 2\omega$, the term $\tilde{\Omega}$ can be neglected. This approximation is known as the "rotating wave approximation" (RWA) [30, 51] which we have used throughout our thesis. Under this approximation, the effective Hamiltonian becomes explicitly time independent written as

$$\mathcal{H} = -\hbar\left[\Delta|2\rangle\langle 2| - \Omega|2\rangle\langle 1| - \Omega^*|1\rangle\langle 2|\right]. \tag{1.71}$$

1.5.1 Rabi oscillation

We now want to study the population dynamics of the two-level atomic system interacting with the external laser field. The density matrix operator of the system is defined as

$$\begin{aligned} \rho &= |\psi\rangle\langle\psi|, \\ &= \left(c_1|1\rangle + c_2|2\rangle\right)\left(c_1^*\langle 1| + c_2^*\langle 2|\right), \\ &= \rho_{11}|1\rangle\langle 1| + \rho_{22}|2\rangle\langle 2| + \rho_{21}|2\rangle\langle 1| + \rho_{12}|1\rangle\langle 2|, \end{aligned} \tag{1.72}$$

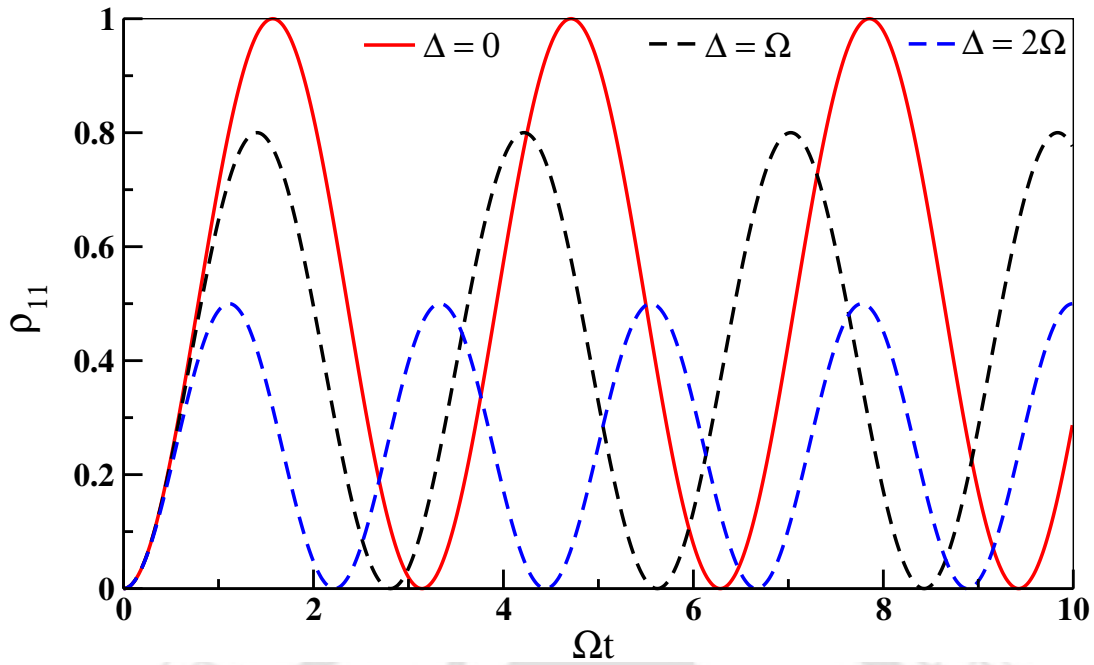

Figure 1.2: The excited state population is plotted as a function of normalized time for different values of detuning.

where $\rho_{11} = |c_1|^2$, and $\rho_{22} = |c_2|^2$ denote the population in the ground and excited state respectively. The off-diagonal terms, $\rho_{21} = c_2 c_1^*$ and $\rho_{12} = c_1 c_2^*$ correspond to the atomic coherences between the two states. We use the following Liouville's equation to obtain the dymanics of the system as

$$\frac{\partial \rho}{\partial t} = -\frac{i}{\hbar}[\mathcal{H}, \rho]. \tag{1.73}$$

The equation of motion is obtained from the following density matrix equations

$$\dot{\rho}_{11} = -\dot{\rho}_{22} = i\Omega^* \rho_{21} - i\Omega \rho_{12}, \tag{1.74a}$$
$$\dot{\rho}_{21} = \dot{\rho}_{12}^* = i\Delta \rho_{21} + i\Omega \left(\rho_{11} - \rho_{22}\right). \tag{1.74b}$$

The above equations are known as optical "Bloch equations" (OBE). We note that for a closed two-level system as the population is conserved *i.e.* $\rho_{11} + \rho_{22} = 1$ we get $\dot{\rho_{11}} = -\dot{\rho}_{22}$. To solve the Eqs. (1.74) we need the initial condition for which we choose that atoms are initially in the ground state *i.e.* $\rho_{11}(t = 0) = 1$. Thus the solution for atomic population and coherences are given by

$$\rho_{22} = \frac{4|\Omega|^2}{\Omega_G^2} \sin^2\left(\frac{\Omega_G t}{2}\right), \tag{1.75}$$
$$\rho_{21} = \frac{2\Omega}{\Omega_G^2} \sin\left(\frac{\Omega_G t}{2}\right) \left\{ i\Omega_G \cos\left(\frac{\Omega_G t}{2}\right) - \Delta \sin\left(\frac{\Omega_G t}{2}\right) \right\}, \tag{1.76}$$

where $\Omega_G = \sqrt{\Delta^2 + 4|\Omega|^2}$ is called the generalized Rabi frequency of the system. Figure 1.2 shows how the excited state population varies with respect to time for three different values of detunings. For $\Delta = 0$, the excited state population ρ_{22} oscillates between maximum value 1 to minimum value 0 with a frequency Ω. As the detuning increases the frequency of oscillation increases with a reduction in amplitude. This

oscillation of population is known as Rabi oscillation. The first discovery of Rabi oscillation is attributed to physicist Isidor Rabi in 1937 while studying atomic nuclei using molecular beams [24]. The theoretical explanation and experimental verification of this effect became the basis for modern NMR spectroscopy [52]. In 1944 Rabi was awarded Nobel Prize for his resonance method for recording the magnetic properties of atomic nuclei.

1.5.2 Influence of decoherence on the evolution of population and coherence

So far, we have discussed the dynamics of the two-level atomic system without taking any kind of decoherence processes. In a real atomic system, relaxation mechanisms such as spontaneous emission and collisions alter the population and coherence dynamics of the system. Using Eq. (1.47), we can get the full density matrix equation incorporating the decay rates as

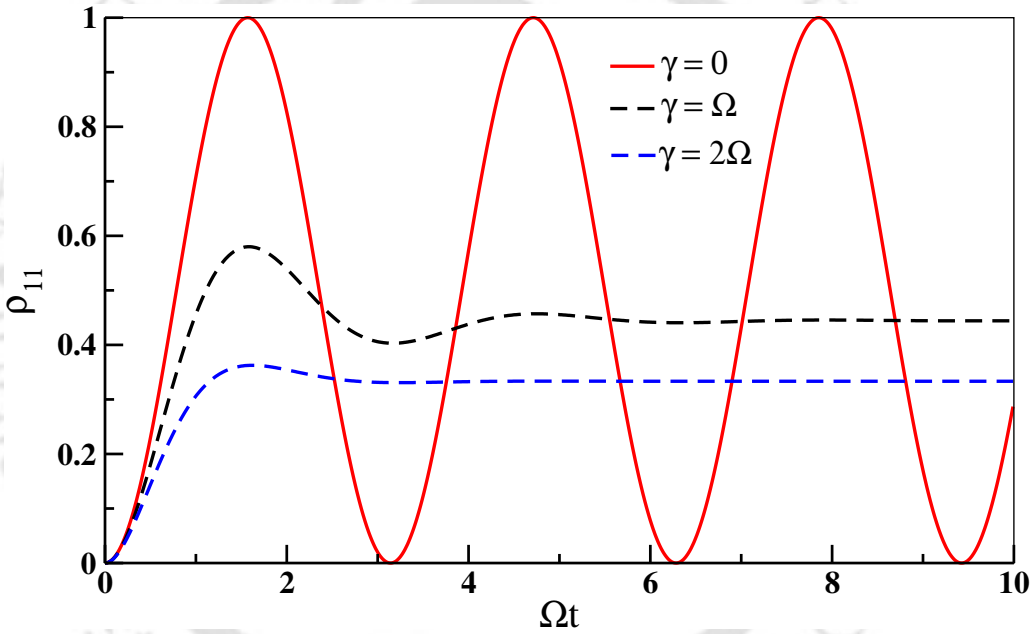

Figure 1.3: Population of the excited state is plotted as a funtion of normalized time in the presence of the spontaneous decay rate γ.

$$\dot{\rho}_{11} = -\dot{\rho}_{22} = i\Omega^*\rho_{21} - i\Omega\rho_{12} + \gamma\rho_{22}, \tag{1.77a}$$

$$\dot{\rho}_{21} = \dot{\rho}^*_{12} = (i\Delta - \Gamma)\rho_{21} + i\Omega\left(\rho_{11} - \rho_{22}\right), \tag{1.77b}$$

where γ is the spontaneous decay rate from the excited state $|2\rangle$ to ground state $|1\rangle$ and $\Gamma = \gamma + \gamma_c$ represents the coherence decay rates. In the absence of the collisional decay rate γ_c, we can find the exact analytical result for the excited state population as

$$\rho_{22}(t) = \frac{4|\Omega|^2}{(\gamma^2 + 8|\Omega|^2)} - \frac{2|\Omega|^2}{\Gamma'(\gamma^2 + 8|\Omega|^2)}\left[(\Gamma' + 3\gamma)e^{-\frac{(3\gamma-\Gamma')t}{4}} + (\Gamma' - 3\gamma)e^{-\frac{(3\gamma+\Gamma')t}{4}}\right], \tag{1.78}$$

where $\Gamma' = \sqrt{\gamma^2 - 64|\Omega|^2}$. Now there arise two cases. If $\gamma^2 > 64|\Omega|^2$, Γ' is real, which is the overdamped case. For this situation, the solution is given by Eq. (1.78). At

$t \to \infty$ the exponentials vanish and the steady value is $\rho_{22}(\infty) = (4|\Omega|^2/\gamma^2 + 8|\Omega|^2)$. On the other hand, if $\gamma^2 < 64|\Omega|^2$, Γ' is imaginary and let $\Gamma' = i\Gamma''$. For this underdamped case, the solution is given by

$$\rho_{22}(t) = \frac{4|\Omega|^2}{\gamma^2 + 8|\Omega|^2}\left[1 - e^{-\frac{3\gamma t}{4}}\left[\cos\left(\frac{\Gamma'' t}{4}\right) + \frac{3\gamma}{\Gamma''}\sin\left(\frac{\Gamma'' t}{4}\right)\right]\right]. \tag{1.79}$$

This shows damped oscillations with angular frequency $(\Gamma''/4)$. Figure 1.3 represents the time-dependent behavior of excited state ρ_{22} for the atoms initially in their ground states. We note that for a finite decay rate the Rabi oscillations are damped out more rapidly and eventually reach a steady state at $\gamma t \gg 1$.

We are now interested to study the steady state response of the system. So the time derivative of the density matrix in Eqs. (1.77) would be zero, *i.e.* $\dot{\rho}_{ij} = 0$. Solving the excited state population and coherence in the steady state, we get

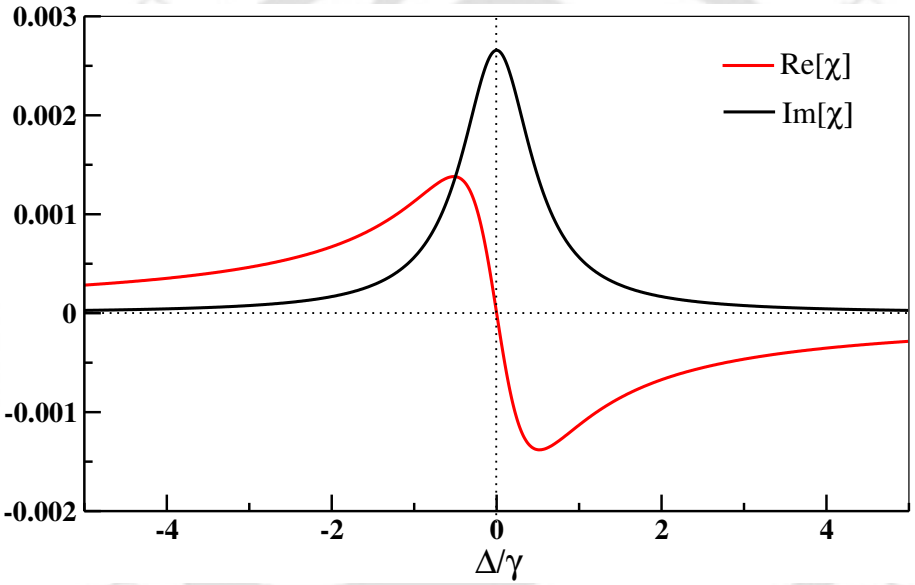

Figure 1.4: Real and imaginary part of χ is plotted as a function of the normalized field detuning. The parameters are taken for ^{87}Rb vapour at a density $\mathcal{N} = 5 \times 10^{11}$ atoms/cc, wavelength $\lambda = 780$ nm, and $\gamma = 3\pi \times 10^6$ rad/s.

$$\rho_{22} = \frac{4|\Omega|^2}{(\gamma^2 + 4\Delta^2) + 8|\Omega|^2}, \quad \rho_{21} = \frac{\Omega(2i\gamma - 4\Delta)}{(\gamma^2 + 4\Delta^2) + 8|\Omega|^2}. \tag{1.80}$$

The charges in the atom are displaced when an external electric field is applied, giving rise to an induced dipole moment. The macroscopic quantity that describes the collective dipole response of the medium is the polarization. This polarization can be obtained by averaging the individual dipole moments over all particles in the system as

$$\vec{P} = \mathcal{N}\langle\vec{d}\rangle = \mathcal{N}Tr(\vec{d}\rho) = \mathcal{N}(\vec{d}_{12}\rho_{21} + H.c.). \tag{1.81}$$

Also, the induced polarization holds the relation $\vec{P} = \chi\vec{E}$, where χ is called the

susceptibility of the medium. Using the steady state solution for ρ_{21} we get

$$\begin{aligned}\chi &= \frac{\mathcal{N}|d_{21}|^2}{\hbar\Omega}\rho_{21}, \\ &= \frac{\mathcal{N}|d_{21}|^2}{\hbar}\frac{(2i\gamma - 4\Delta)}{(\gamma^2 + 4\Delta^2) + 8|\Omega|^2}, \\ &= \frac{3\mathcal{N}\gamma}{2k^3}\frac{(2i\gamma - 4\Delta)}{(\gamma^2 + 4\Delta^2) + 8|\Omega|^2},\end{aligned} \tag{1.82}$$

where $\mathcal{N}$ is the atomic density of the medium. The spontaneous decay rate γ is related by Weisskopf-Wigner theory [30] as $\gamma = 2k^3|d_{21}|^2/3\hbar$. In Fig. 1.4 we plot the real and imaginary parts of the susceptibility as a function of field detuning. The real part of the susceptibility represents the dispersive response of the medium, while the imaginary part corresponds to absorption (or gain) characteristics. The positive value of $\mathrm{Im}[\chi_{21}]$ at $\Delta = 0$ shows maximum absorption of the electric field at resonance. We also find the dispersion exhibits anomalous behaviour around $\Delta = 0$, signifying a rapid change in the refractive index near resonance. The strong resonant absorption in a two-level atomic system hinders the propagation of weak optical fields and limits practical applications. This absorption can be reduced using the saturation absorption (SAT) technique [53, 54], where an intense pump field rapidly drives atoms from ground to excited states, leading to a depletion of the ground-state population. As a result, the medium becomes partially transparent, enabling the weak probe field to propagate with reduced loss. Moreover, by introducing an additional control field, the system can be extended to a three-level configuration, where the susceptibility is drastically modified through quantum interference effects.

1.6 Three level atomic system

A two-level atomic system is fundamental for studying key phenomena such as Rabi oscillations, spontaneous emission, and saturation; however, its application is limited since excitation and emission occur through the same transition. Transitioning to a three-level atomic system enhances atomic coherence and alters absorption and dispersion characteristics. Three primary configurations can be established based on geometric structure and dipole transitions: Ladder (Ξ), Lambda (Λ), and Vee (V) shown in Fig. 1.5. The Λ-system, consisting of two closely spaced lower states and one shared excited state, allows for long-lived ground-state coherences, which are advantageous for investigating quantum interference and coherence effects. This section will focus on the optical properties of the Λ-level atomic system due to atomic coherence between different transitions.

The transition $|1\rangle \leftrightarrow |3\rangle$, and $|3\rangle \leftrightarrow |2\rangle$ are dipole allowed, while the transition $|1\rangle \leftrightarrow |2\rangle$ is dipole forbidden. A strong field at frequency ω_c couples the transition $|2\rangle \leftrightarrow |3\rangle$. This strong field can alter the optical properties of the medium; referred to as the control field. Conversely, a weaker field couples to $|1\rangle \leftrightarrow |3\rangle$ transition to investigate the response of the atomic medium, called the probe field. The probe and the control field can be expressed as

$$\vec{E}_j(r,t) = \hat{e}_j\mathcal{E}_j(\vec{r})e^{-i(\omega_j t - \vec{k}_j\cdot\vec{r})} + c.c., \tag{1.83}$$

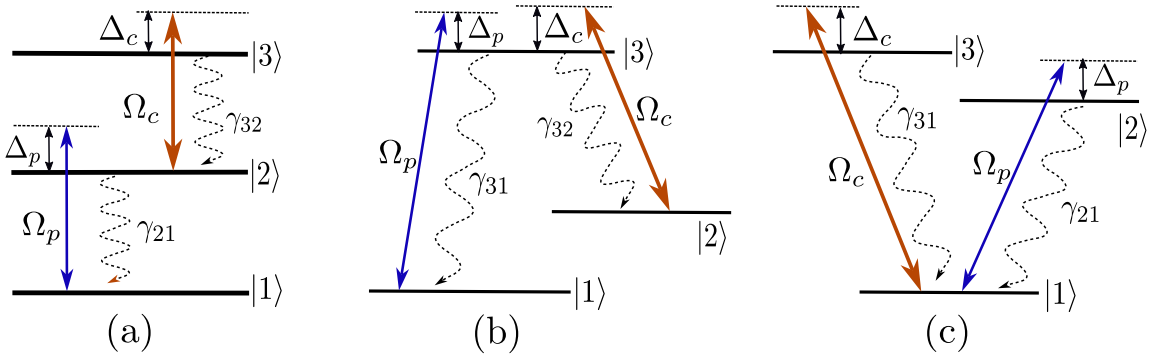

Figure 1.5: Schematic diagram of a three types of three level systems. (a), (b), and (c) are known as "Ladder" Ξ, "Lambda" Λ, and "Vee" V systems, respectively.

where $\hat{e}_j$, $\mathcal{E}_j(\vec{r})$, and $\vec{k}_j$ are unit polarization vector, spatial envelop and wave vector respectively. The index $j \in p, c$ correspond to probe and control fields respectively. The total Hamiltonian of the system is given by

$$H = \hbar\left(\omega_{13}|1\rangle\langle 1| + \omega_{12}|2\rangle\langle 2|\right) - \hbar\left(\Omega_p|3\rangle\langle 1|e^{-i\omega_p t} + \Omega_c|3\rangle\langle 2|e^{-i\omega_c t} + H.c.\right), \quad (1.84)$$

where the Rabi frequencies are defined as

$$\Omega_p = \frac{\vec{d}_{31}\cdot\hat{e}_p}{\hbar}\mathcal{E}_p(\vec{r})e^{i\vec{k}_p\cdot\vec{r}}, \quad \Omega_c = \frac{\vec{d}_{32}\cdot\hat{e}_c}{\hbar}\mathcal{E}_c(\vec{r})e^{i\vec{k}_c\cdot\vec{r}}. \quad (1.85)$$

To eliminate the explicit time dependence in the Hamiltonian we apply an unitary transformation as

$$U = \exp\left[-i\omega_p t|3\rangle\langle 3| - i(\omega_p - \omega_c)t|2\rangle\langle 2|\right], \quad (1.86)$$

and also applying RWA to get the effective Hamiltonian as

$$\mathcal{H} = -\hbar\Delta_p|3\rangle\langle 3| - \hbar(\Delta_p - \Delta_c)|2\rangle\langle 2| - \hbar(\Omega_c|3\rangle\langle 2| + \Omega_p|3\rangle\langle 1| + \text{H.c.}), \quad (1.87)$$

where the single photon detuning for the probe and control field is defined as

$$\Delta_p = \omega_p - \omega_{31}, \quad \Delta_c = \omega_c - \omega_{32} \quad (1.88)$$

To find the population dynamics and the atomic coherence we use the following Liouville equation

$$\frac{\partial\rho}{\partial t} = -\frac{i}{\hbar}[\mathcal{H}, \rho] + \mathcal{L}\rho, \quad (1.89)$$

where the Lindblad superoperator is given by

$$\mathcal{L}\rho = -\sum_{j=1}^{2}\frac{\gamma_{3i}}{2}\left(|3\rangle\langle 3|\rho - 2|j\rangle\langle j|\rho_{jj} + \rho|3\rangle\langle 3|\right), \quad (1.90)$$

where γ_{31}, and γ_{32} are the radiative decay rates from the excited state $|3\rangle$ to the ground state $|1\rangle$, and metastable state $|2\rangle$ respectively. Using Eq. (1.89) we get the

density matrix equation as

$$\dot{\rho}_{11} = \gamma_{31}\rho_{33} + i\left(\Omega_p^*\rho_{31} - \Omega_p\rho_{13}\right), \tag{1.91a}$$
$$\dot{\rho}_{22} = \gamma_{32}\rho_{33} + i\left(\Omega_c^*\rho_{32} - \Omega_c\rho_{23}\right), \tag{1.91b}$$
$$\dot{\rho}_{33} = -\left(\gamma_{32} + \gamma_{31}\right)\rho_{33} + i\left(\Omega_c\rho_{23} - \Omega_c^*\rho_{32} + \Omega_p\rho_{13} - \Omega_p^*\rho_{31}\right), \tag{1.91c}$$
$$\dot{\rho}_{32} = -\left(\Gamma_{32} - i\Delta_c\right)\rho_{32} + i\Omega_p\rho_{12} + i\Omega_c\left(\rho_{22} - \rho_{33}\right), \tag{1.91d}$$
$$\dot{\rho}_{31} = -\left(\Gamma_{31} - i\Delta_p\right)\rho_{31} + i\Omega_c\rho_{21} + i\Omega_p\left(\rho_{11} - \rho_{33}\right), \tag{1.91e}$$
$$\dot{\rho}_{21} = -\left[\Gamma_{21} - i\left(\Delta_p - \Delta_c\right)\right]\rho_{21} + i\left(\Omega_c^*\rho_{31} - \Omega_p\rho_{23}\right) \tag{1.91f}$$

where $\Gamma_{31} = \Gamma_{32} = (\gamma_{31} + \gamma_{32})/2$, and Γ_{21} denotes the decay rate of ground state coherence. The total population is conserved *i.e.* $\rho_{11} + \rho_{22} + \rho_{33} = 1$ and the other of diagonal elements can be found by $\rho_{ij} = \rho_{ji}^*$.

1.6.1 Steady state analysis

We want to now study the steady state solution of the optical Bloch equations as in Eqs. (1.91). These equations are nonlinear due to the interaction between atomic coherences and the applied fields. If the probe field is much weaker than the control field, one can greatly simplify the analysis by employing a perturbative expansion of the atomic density matrix in powers of the probe field strength. As the probe field is much weaker than the control field *i.e.* $\Omega_p \ll \Omega_c$, the perturbation expansion up to first order in probe field can be written as

$$\rho_{ij} = \rho_{ij}^{(0)} + \Omega_p\rho_{ij}^{(1)} + \Omega_p^*\rho_{ij}^{(2)}, \tag{1.92}$$

where $\rho_{ij}^{(0)}$ describes the solution in the absence of the probe field and $\rho_{ij}^{(1)}$, $\rho_{ij}^{(2)}$ represent the linear order solution in the presence of the probe field at a frequency ω_p, and $-\omega_p$, respectively. To find the coherence, we substitute Eq. (1.92) in Eqs. (1.91) and equate the coefficient of Ω_p. Solving the 8 coupled equations, we get the steady state expression of the coherence as

$$\rho_{31} = \frac{i\Omega_p(\Gamma_{21} - i(\Delta_p - \Delta_c))}{|\Omega_c|^2 + (\Gamma_{31} - i\Delta_p)(\Gamma_{21} - i(\Delta_p - \Delta_c))}. \tag{1.93}$$

The linear susceptibility of the medium in terms of atomic coherence ρ_{31} is given by the following relation

$$\chi_{31}(\omega_p) = \frac{\mathcal{N}|d_{31}|^2}{\hbar\Omega_p}\rho_{31} = \frac{i\mathcal{N}|d_{31}|^2}{\hbar}\frac{1}{\frac{|\Omega_c|^2}{(\Gamma_{21} - i(\Delta_p - \Delta_c))} + (\gamma - i\Delta_p)}, \tag{1.94}$$

where we consider $\gamma_{31} = \gamma_{32} = \gamma$. The control field effect on the medium susceptibility can be realized by Eq. (1.94). We can identify that in absence of Ω_c the susceptibility shows similar feature to a two-level atomic system. In Fig. 1.6 we have plotted the real and imaginary parts of the susceptibility as a function of probe field detuning. The $\mathrm{Im}[\chi_{31}]$ shows that the absorption goes to zero at two photon resonance, *i.e.* $\Delta_p - \Delta_c = 0$. Therefore, the medium becomes transparent for the probe field in the presence of a strong control field. This phenomenon is known as "Electromagnetically induced transparency" (EIT) [23]. The term EIT was first coined by Stephen E. Harris and his collaborators in the early 1990s. In a Λ-level

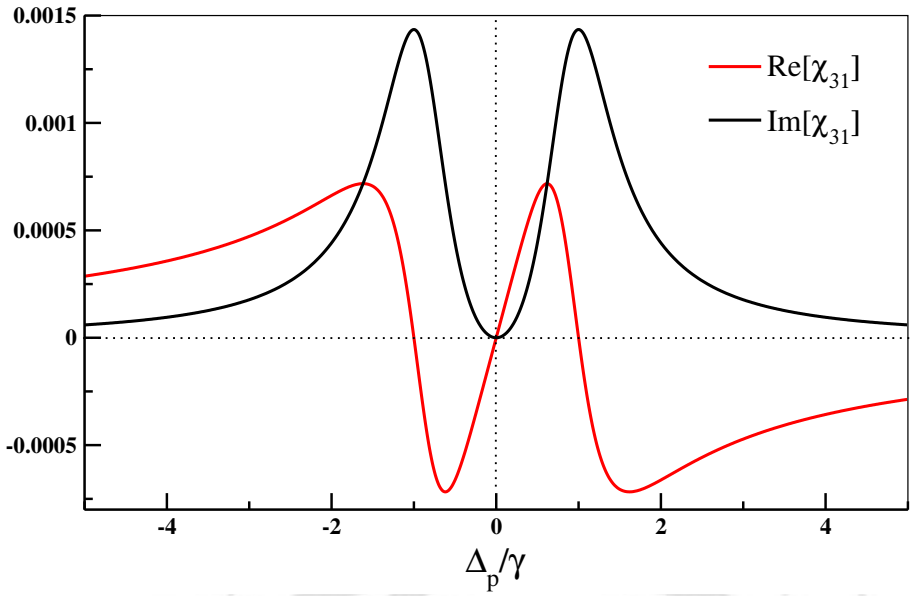

Figure 1.6: Real and imaginary part of χ_{31} is plotted as a function of the normalized probe field detuning. The parameters are taken for ^{87}Rb vapour at a density $\mathcal{N} = 5 \times 10^{11}$ atoms/cc, $\Omega_p = \gamma$, wavelength $\lambda = 780$ nm, and $\gamma = 3\pi \times 10^6$ rad/s.

atomic system, the ground state population in $|1\rangle$ can be transferred to the excited state $|3\rangle$ by two quantum pathways: $|1\rangle \rightarrow |3\rangle$, and $|1\rangle \rightarrow |3\rangle \rightarrow |2\rangle \rightarrow |3\rangle$. At two-photon resonance, the transition probability corresponding to these two pathways destructively interferes, resulting in vanishing absorption. The Re$[\chi_{31}]$ shows a steep normal dispersion at the transparency window. The transparency window can be increased by using a stronger control field. EIT acts as a versatile tool with far-reaching applications in areas such as slow light [55, 56], optical storage [57], precision metrology [58], and quantum information processing [59].

1.6.2 Dressed state analysis

In the presence of interaction with EM fields, the bare atomic energy levels of an atom are no longer the true eigenstates of the system. The new eigenstate of the effective Hamiltonian is called the dressed state. The dressed-state picture offers a deeper and more intuitive physical understanding of EIT. The effective Hamiltonian in Eq. (1.87) is written as

$$\mathcal{H} = -\hbar \begin{pmatrix} 0 & 0 & \Omega_p^* \\ 0 & (\Delta_p - \Delta_c) & \Omega_c^* \\ \Omega_p & \Omega_c & \Delta_p \end{pmatrix}. \tag{1.95}$$

Considering the two photon resonance condition *i.e.* $\Delta_p - \Delta_c = 0$, the eigenvalues of the effective Hamiltonian is given by

$$\lambda_0 = 0, \tag{1.96}$$

$$\lambda_+ = \frac{\hbar}{2}\left[\Delta_p + \sqrt{\Delta_p^2 + 4(|\Omega_p|^2 + |\Omega_c|^2)}\right], \tag{1.97}$$

$$\lambda_- = \frac{\hbar}{2}\left[\Delta_p - \sqrt{\Delta_p^2 + 4(|\Omega_p|^2 + |\Omega_c|^2)}\right], \tag{1.98}$$

and the corresponding eigenvectors are

$$|0\rangle = \cos\theta|1\rangle - \sin\theta|2\rangle, \tag{1.99a}$$
$$|+\rangle = \sin\theta\sin\phi|1\rangle + \cos\theta\sin\phi|2\rangle + \cos\phi|3\rangle, \tag{1.99b}$$
$$|-\rangle = \sin\theta\cos\phi|1\rangle + \cos\theta\cos\phi|2\rangle - \sin\phi|3\rangle, \tag{1.99c}$$

where θ and ϕ are expressed as

$$\tan\theta = \frac{\Omega_p}{\Omega_c}, \quad \tan(2\phi) = \frac{2\sqrt{|\Omega_p|^2 + |\Omega_c|^2}}{\Delta_p}. \tag{1.100}$$

We note from Eqs. (1.99), the dressed state $|0\rangle$ remains at zero energy and the other two state $|+\rangle$, and $|-\rangle$ are shifted equally from energy $\hbar\Delta_p/2$. It is interesting that the state $|0\rangle$ is formed by the linear superposition of ground state $|1\rangle$, and metastable state $|2\rangle$ without containing the excited state $|3\rangle$. An atom prepared in this state does not absorb or emit any light and has no probability for transition to the state $|3\rangle$. Therefore, the population gets trapped in this state, known as 'dark state'. This phenomenon is known as "Coherent Population Trapping" (CPT). The first observation of CPT was made by Alzetta *et al.* [60]. In this phenomena, both the control and probe field are of comparable strength *i.e.* $\Omega_p \approx \Omega_c$. Now, in the other situation, when the probe field is much weaker in comparison to the control field strength $\Omega_p \ll \Omega_c$ the dressed state at probe resonance ($\Delta_p = 0$) is given by

$$|0\rangle = |1\rangle, \tag{1.101a}$$
$$|+\rangle = \frac{1}{\sqrt{2}}\left(|2\rangle + |3\rangle\right), \tag{1.101b}$$
$$|-\rangle = \frac{1}{\sqrt{2}}\left(|2\rangle - |3\rangle\right). \tag{1.101c}$$

We note that the ground state $|1\rangle$ now becomes the dark state. Therefore the transition probability from state $|1\rangle$ to any of the dressed state $|+\rangle$, and $|-\rangle$ is zero, which means the probe field absorption vanishes at two-photon resonance. This explains the EIT phenomenon. Moreover, the states $|2\rangle$, and $|3\rangle$ are dressed by the strong control field which creates states $|+\rangle$, and $|-\rangle$. These two states are separated by an amount $|\Omega_c|$. The transition from the state $|1\rangle$ to the states $|+\rangle$, and $|-\rangle$ results in the formation of two absorption peaks.

1.7 Super-resolution microscopy

In this section, we will be discussing the super-resolution microscopy and its importance in imaging. We often hear that "a picture is worth a thousand words". It holds true not only in everyday life but also in the natural sciences. In fact, the rise of modern science closely paralleled the invention of the light microscope, which, for the first time, allowed humanity to visualize the cellular structure of living organisms [61]. In 1873, Ernst Abbe revealed that light microscopes are fundamentally limited by diffraction [62]. According to this theory, the minimum distance at which distinct elements can be discerned is $d = \lambda/(2n\sin\theta)$, where λ represents the wavelength of light, and $n\sin\theta$ denotes the numerical aperture of the objective lens. Under optimal conditions, focusing microscopes achieve a resolution of approximately 180

nm in the focal plane (x, y) and 500–800 nm along the optic axis (z) [63]. Although electron and near-field microscopes achieved higher spatial resolution [64], they could not replace light microscopy in areas like live-cell imaging, lithography, and optical data storage, where non-invasive, far-field techniques are essential. This diffraction barrier therefore, became a major challenge, driving scientists to search for ways to surpass this fundamental limit.

Reducing the wavelength, as in X-ray microscopy, can improve resolution to around 30 nm [65], but it is not suitable for studying living samples. Another method, 4Pi microscopy [66], enhances axial resolution from about 500 nm to 100 nm by coherently combining light waves from two opposing lenses, yet it still remains limited by diffraction. The true breakthrough came in 1994 when Stefan W. Hell proposed STED microscopy [67], a technique that for the first time provided a practical way to surpass the diffraction limit. By 1999, Hell and his team had successfully demonstrated the STED microscopy [68], leading in the era of super-resolution optical microscopy. After the invention of STED microscopy, several other super-resolution techniques were developed, including reversible saturable optical fluorescence transitions (RESOLFT) [69], photoactivated localization microscopy (PALM) [70], stochastic optical reconstruction microscopy (STORM) [71], and structured illumination microscopy (SIM) [72]. Each of these methods utilizes a distinct physical principle to surpass the classical diffraction barrier of light.

Among the recent super-resolution techniques, minimal fluorescence photon fluxes (MINFLUX) [73] stands out for its novel concept. Unlike PALM and STORM, which localize molecules by detecting the maximum number of fluorescence photons—a process limited by photobleaching, MINFLUX achieves localization by aligning the molecule with the dark center of a doughnut-shaped excitation beam, where fluorescence is minimal. Next, we focus on the STED technique, which we employ to achieve super-resolution imaging in the QD system in one of our research problems.

1.7.1 STED microscopy

In a conventional fluorescence microscope, when a sample is excited by a focused laser beam, all the fluorescent molecules within the focal spot emit light simultane-

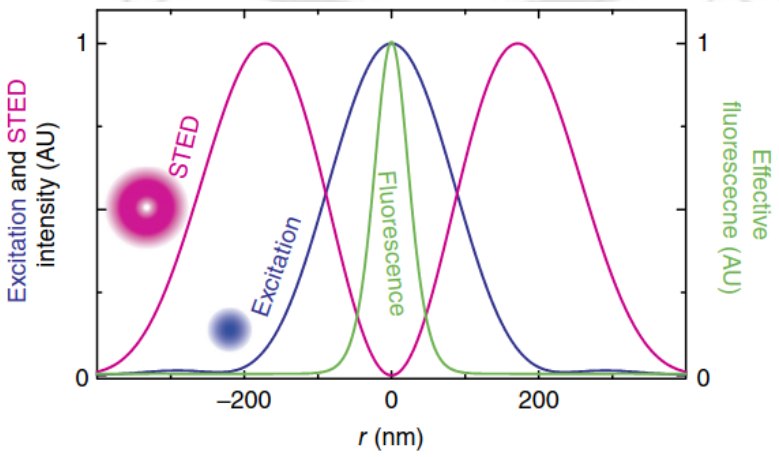

Figure 1.7: A representation of the excitation beam, STED beam and the fluorescence vs spatial extent according to STED microscopy principle [1].

ously, producing a blurred image with a lateral resolution of about 200 nm, limited by diffraction. The key idea of STED microscopy is to achieve spatially selective deactivation of fluorophores, thereby preventing certain molecules from contributing to fluorescence [1]. The technique employs two laser beams: an excitation beam, which promotes the population from the ground state to the excited state (the "on" state), and a red-shifted depletion beam, which drives the excited population back to the ground state via stimulated emission, rendering them non-fluorescent (the "off" state). The depletion beam is shaped like a doughnut, with a dark center surrounded by a bright ring. When both beams are applied together, the population in the outer region of the focal spot is deactivated by the depletion beam before they can emit fluorescence, while only those at the center where the depletion intensity is zero, remain capable of fluorescing, as shown in Fig. 1.7. By increasing the intensity of the depletion beam, the effective fluorescent region can be reduced even further, thereby confining the emission volume to dimensions well below the diffraction limit. An image is then formed by scanning this nanoscale fluorescent spot across the sample, achieving a level of detail previously impossible with conventional light microscopy. This naturally leads to an important question: What defines the new resolution limit in STED microscopy? Clearly, it can no longer be described by the Abbe's equation. To answer this, we next derive the analytical expression for the resolution limit in STED microscopy.

A plane wave incident on a circular aperture produces a far-field diffraction pattern on a distant observation screen, as illustrated in Fig. 1.8. By introducing a converging lens, this observation screen can be moved much closer to the aperture

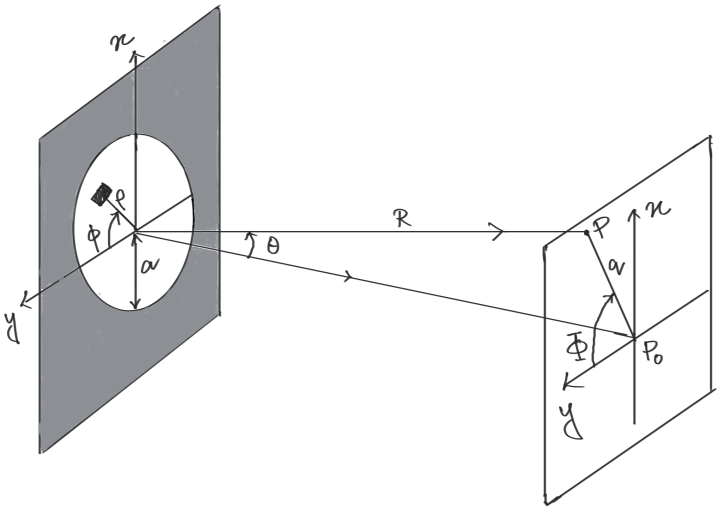

Figure 1.8: A diagram representing diffraction through a circular aperture

without altering the diffraction pattern [74]. Furthermore, if the lens is positioned so that it lies within and completely fills the aperture, the resulting diffraction pattern remains unchanged. After passing through the lens, the light is brought to focus and forms an image in the focal plane. This is the fundamental operating principle behind optical systems such as the eye, telescopes, microscopes, and camera lenses. However, the image formed cannot collapse to an ideal point because diffraction inevitably spreads the light, producing a finite-sized intensity distribution. According to the Huygens–Fresnel principle, the electric field at a point P in the focal plane

can be expressed in spherical coordinates as

$$\vec{E} = \frac{\mathcal{E}\, e^{i(\omega t - kR)}}{R} \int_{\rho=0}^{a} \int_{\phi=0}^{2\pi} e^{i(k\rho q/R)} \cos(\phi - \Phi)\, \rho\, d\rho\, d\phi, \tag{1.102}$$

where $\mathcal{E}$ is the source strength per unit area assumed to be constant over the entire aperture, R is the distance from the center of the aperture to the point P and the differential area $ds = \rho d\rho d\phi$. Because of the complete axial symmetry the solution of Eq. (1.102) must be independent of Φ. So we can solve it by taking $\Phi = 0$ for simplicity and using the identity

$$\int_0^{2\pi} e^{i(m\nu + u\cos\nu)}\, d\nu = 2\pi\, i^m\, J_m(u), \tag{1.103}$$

where $j_m(u)$ represents the Bessel function of first kind of order m. Therefore Eq. (1.102) can now be written as

$$\vec{E} = \frac{\mathcal{E}\, e^{i(\omega t - kR)}}{R}\, 2\pi \int_0^a J_0\left(\frac{k\rho q}{R}\right)\, \rho\, d\rho. \tag{1.104}$$

By using another recurrence form as

$$\frac{d}{du}(u^m J_m(u)) = u^m J_{m-1}(u), \tag{1.105}$$

we can write for $m = 1$ as

$$\int_0^u u' J_0(u')\, du' = u J_1(u). \tag{1.106}$$

Now we want to solve Eq. (1.104). Let $w = (k\rho q/R)$ then $d\rho = (R/kq)dw$. So we can write

$$\int_0^a J_0\left(\frac{k\rho\, q}{R}\right) \rho\, d\rho = \left(\frac{R}{kq}\right)^2 \int_0^{kaq/R} J_0(w)\, w\, dw. \tag{1.107}$$

Solving Eq. (1.104) we get

$$\vec{E} = \frac{\mathcal{E} e^{i(\omega t - kR)}}{R}\, 2\pi a^2 \left(\frac{R}{kaq}\right) J_1\left(\frac{kaq}{R}\right). \tag{1.108}$$

Now, the intensity at point P can be written as

$$I = \tfrac{1}{2}\vec{E}\vec{E}^* = \frac{2\mathcal{E}^2 A^2}{R^2} \left[\frac{J_1\left(\frac{kaq}{R}\right)}{\frac{kaq}{R}}\right]^2, \tag{1.109}$$

where $A = \pi a^2$ is the area of the aperture. From the recurrence relation in Eq. (1.105) for $m = 1$ we can write

$$J_0(u) = \frac{d}{du} J_1(u) + \frac{J_1(u)}{u}. \tag{1.110}$$

Now from Eq. (1.103) we get $J_0(0) = 1$, and $J_1(0) = 0$. By using L'Hospital's rule in Eq. (1.110) we get $J_1(u)/u = 1/2$ at $u = 0$. Therefore, Eq. (1.109) can be written as

$$I = I(0) \left[\frac{2J_1\left(\frac{kaq}{R}\right)}{\frac{kaq}{R}}\right]^2 \tag{1.111}$$

$$= I(0)\left[\frac{2J_1(kan\sin\theta)}{kan\sin\theta}\right]^2, \tag{1.112}$$

where $I(0) = \mathcal{E}^2A^2/2R^2$ is the intensity at the center of the focal plane and $q = Rn\sin\theta$ for a medium of refractive index n. If $x = kan\sin\theta \ll 1$ which means near the central axis, we can expand as

$$\frac{2J_1(x)}{x} = 1 - \frac{x^2}{8} + \cdots \approx \cos\left(\frac{x}{2}\right) = \cos\left(\frac{\pi an\sin\theta}{\lambda}\right). \tag{1.113}$$

Finally we arrived at a analytical expression for the total intensity as

$$I = I(0)\cos^2\left(\frac{\pi an\sin\theta}{\lambda}\right). \tag{1.114}$$

It is evident from Eq. (1.114) that a Gaussian excitation beam in STED microscopy reaches its maximum intensity at $a = 0$. In an analogous manner, the intensity profile of the doughnut-shaped STED beam can be modeled using a term proportional to $\sin^2(\pi an\sin\theta/\lambda)$ which ensures that its intensity vanishes at $a = 0$. So the normalized excitation probability in the focal plane of the lens for the excitation beam $h_{ex}(r)$ (known as point spread function) is modeled as [75]

$$h_{ex}(r) = \cos^2\left(\frac{\pi rn\sin\theta}{\lambda_{ex}}\right), \tag{1.115}$$

where θ is the semi aperture of the lens. After implementing the depletion beam (STED beam) the fluorescence probability $\eta(r)$ of a molecule is decayed to $\eta(r) = \exp(-\kappa\tau)$, where $\kappa = \sigma I_{STED}(r)$ is the depletion rate of the excited state and σ is the cross section for stimulated emission. The intensity of the STED beam is given as

$$I_{STED}(r) = I_{STED}^{max}\sin^2\left(\frac{\pi rn\sin\theta}{\lambda_{STED}}\right), \tag{1.116}$$

where the saturation intensity $I_{sat} = 1/\sigma\tau$. At this value of intensity it drops $(1/e)$ times the maximum value. Now to detect a photon at a position r (radial distance from the center) is given by

$$\begin{aligned}
h(r) &= h_{ex}(r)\eta(r)\\
&= \cos^2\left(\frac{\pi rn\sin\theta}{\lambda_{ex}}\right)\exp\left\{-\sigma\tau I_{STED}\right\}\\
&= \cos^2\left(\frac{\pi rn\sin\theta}{\lambda_{ex}}\right)\exp\left\{-\sigma\tau I_{STED}^{max}\sin^2\left(\frac{\pi rn\sin\theta}{\lambda_{STED}}\right)\right\}\\
&= \frac{1}{2}\left[1+\cos\left(\frac{2\pi rn\sin\theta}{\lambda_{ex}}\right)\right]\exp\left\{-\frac{\sigma\tau I_{STED}^{max}}{2}\left(1-\cos\left(\frac{2\pi rn\sin\theta}{\lambda_{ex}}\right)\right)\right\}\\
&\approx \left[1-\left(\frac{\pi rn\sin\theta}{\lambda}\right)^2\right]\left\{1-\frac{\sigma\tau I_{STED}^{max}}{4}\left(\frac{2\pi rn\sin\theta}{\lambda}\right)^2\right\} \quad (\lambda_{ex}\approx\lambda_{STED}\equiv\lambda)\\
&= 1-\left(\frac{\pi rn\sin\theta}{\lambda}\right)^2(1+\sigma\tau I_{STED}^{max}).
\end{aligned} \tag{1.117}$$

In the above equation we use the Taylor series expansion upto second order for $\cos(2\pi rn\sin\theta)/\lambda$. Now as $h(r) = 1$, Eq. (1.117) reduces to

$$r = \frac{\lambda}{\pi n \sin\theta}\sqrt{\frac{0.5}{1+\sigma\tau I_{STED}^{max}}},$$
$$\implies \Delta r = 2r \approx \frac{\lambda}{2n\sin\theta\sqrt{1+\frac{I_{STED}^{max}}{I_{sat}}}}. \tag{1.118}$$

The above Eq. (1.118) defines the resolution limit for STED microscopy. It is evident that the resolution depends on the ratio between I_{STED}^{max} and I_{sat}. As this ratio I_{STED}^{max}/I_{sat} increases, meaning the depletion intensity becomes much higher than the saturation intensity, the effective resolution improves, allowing finer spatial detail to be resolved.

1.8 Vector beam and its application

The polarization of light, defined as the geometrical orientation of the oscillating electric field in a transverse wave, is a key factor in ensuring accurate and sensitive optical measurements. Unlike scalar beams, which satisfy the scalar Helmholtz equation, VBs are generated through the vector superposition of two orthogonally polarized Laguerre–Gaussian (LG) modes, satisfying the vector form of the Helmholtz equation. This coupling of orthogonal polarizations produces a nonuniform and spatially varying polarization pattern across the beam's transverse plane, giving vector beams their distinctive structural and functional properties [76]. We will be discussing the generation and the applications of the VBs.

1.8.1 Generation of VB

Beams with higher-order spatial structures are solutions of the paraxial wave equation, with Hermite-Gaussian (HG) and Laguerre–Gaussian (LG) beams representing two important families of such solutions. The HG beams arise as solutions of the paraxial Helmholtz equation in Cartesian coordinates, while the LG beams are the corresponding solutions in cylindrical coordinates. Among them, LG beams have attracted particular interest because their transverse amplitude exhibits phase singularities, a direct consequence of the nonzero orbital angular momentum (OAM) they possess. In cylindrical polar coordinate (r, ϕ, z) the wave equation can be written as

$$\frac{1}{r}\frac{\partial}{\partial r}\left(r\frac{\partial\mathcal{E}}{\partial r}\right) + \frac{1}{r^2}\frac{\partial^2\mathcal{E}}{\partial\phi^2} + 2ik\frac{\partial\mathcal{E}}{\partial z} = 0. \tag{1.119}$$

The solution of the above wave equation are called the LG modes which is given as

$$\mathcal{E}_m^l(r,\phi,z) = \mathcal{E}_0\sqrt{\frac{2m!}{\pi(m+|l|)!}}\frac{w_0}{w(z)}\left(\frac{r\sqrt{2}}{w(z)}\right)^{|l|} e^{-\frac{r^2}{w(z)^2}} L_m^{|l|}\left[\frac{2r^2}{w(z)^2}\right] e^{il\phi}$$
$$\times \exp\left(\frac{ikr^2z}{2(z^2+z_R^2)}\right) e^{-i(2m+|l|+1)\eta(z)}, \tag{1.120}$$

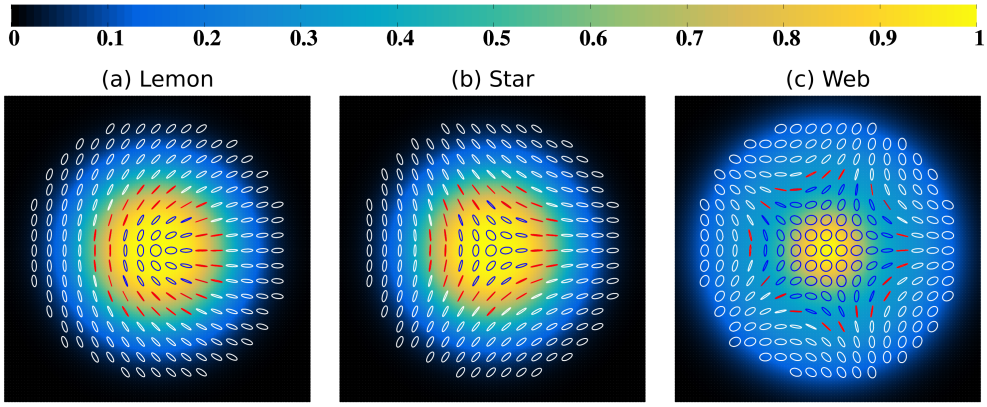

Figure 1.9: Transverse intensity and polarization distribution of (a) Lemon ($l_L = 0, l_R = 1$), (b) Star ($l_L = 0, l_R = -1$), and (c) Web ($l_L = 0, l_R = -3$) VB with $\theta = 0$, and $\alpha = \pi/4$ or all the three cases. The white, red, and blue colour polarization represent right circular, linear and left circular polarization respectively.

where $\mathcal{E}_0$ is the field amplitude, $L_m^{|l|}$ is the generalized Lagurre polynomial with m being the radial index, and l is the OAM index. The beam radius at a propagation length z is denoted by $w(z) = w_0\sqrt{1 + z^2/z_R^2}$, where w_0 is the beam waist at $z = 0$. The free space Rayleigh length is $z_R = kw_0^2/2$, with k being the free space wave number, the Gouy phase can be expressed as $(2m + |l| + 1)\eta(z)$, where $\eta(z) = \tan^{-1}(z/z_R)$. We consider $m = 0$ throughout our thesis. The VBs are generated by vector superposition of two orthogonally polarized LG modes. In circular polarization basis VB is written as

$$\vec{E}(r, \phi, z) = \mathcal{E}_L(r, \phi, z)\hat{e}_L + \mathcal{E}_R(r, \phi, z)\hat{e}_R, \tag{1.121}$$

where,

$$\mathcal{E}_L(r, \phi, z) = \cos(\alpha)LG_0^{l_L}, \text{ and } \mathcal{E}_R(r, \phi, z) = e^{i\theta}\sin(\alpha)LG_0^{l_R}, \tag{1.122}$$

$\mathcal{E}_L$, and $\mathcal{E}_R$ are the left and right circularly polarized component of the VB. Variables α, and θ are the relative amplitude and phase of the two modes, respectively. The spatial modes, $LG_0^{l_i}(i = L, R)$ are the LG polynomial, with the radial index zero is given by

$$\begin{aligned} LG_0^{l_i}(r, \phi, z) =& \mathcal{E}_0\sqrt{\frac{2}{\pi|l_i|!}}\left(\frac{r\sqrt{2}}{w(z)}\right)^{|l_i|} e^{-\frac{r^2}{w(z)^2}} e^{il_i\phi + ik_i n_i z}\exp\left(\frac{ik_i n_i r^2 z}{2(z^2 + n_i^2 z_R^2)}\right) \\ & \times e^{-i(|l_i|+1)\eta(z)}. \end{aligned} \tag{1.123}$$

where the n_i correspond to the refractive index for both the components. If the OAM indices satisfy $l_l \neq l_R$, and $l_l \neq -l_R$, it represents a hybrid-order VB [77] also known as full Poincaré (FP) beams [78] as shown in Fig. 1.9. In contrast, the two LG modes have equal amplitudes but carry opposite orbital angular momenta ($l_L = -l_R$), the resulting field forms a pure vector beam. Such beams can exhibit radial, azimuthal, or spiral polarization distributions, depending on the relative phase between the two components. They are called cylindrical vector (CV) beams [79] because their polarization distribution has rotational symmetry around the beam axis as shown in Fig. 1.10.

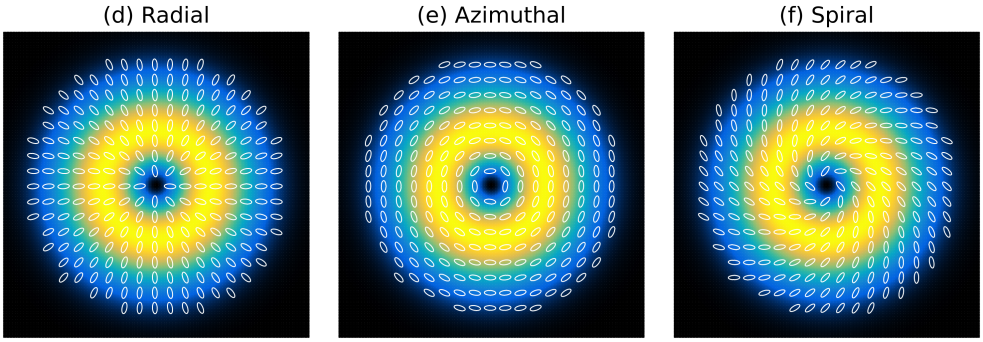

Figure 1.10: Transverse intensity and polarization distribution of (d) Radial ($\theta = 0$), (e) Azimuthal ($\theta = \pi$), (f) Spiral ($\theta = -\pi/2$) CV beam with $\alpha = 3\pi/8$, and $l_L = -1, l_R = 1$ for all the three cases.

Experimentally, VBs can be generated by two main methods: intra-cavity and extra-cavity techniques [80]. Intra-cavity method uses birefringent elements, conjugate Brewster lenses, or multilayer polarization gratings [81, 82], while the extra-cavity method employs cone mirrors, gratings, liquid crystal spatial optical modulators, and radial analyzers with spiral phase elements [83, 84]. The extra-cavity technique is more flexible and widely adopted. In an extra-cavity setup as in Fig. 1.11, a linearly polarized Gaussian beam from an Ar^+ laser is first cleaned and expanded using a spatial filter and lenses [2]. A quarter-wave plate converts it into circular polarization, which then passes through a radial analyzer. The radial analyzer then transforms the circular polarization to azimuthal or radial, depending on the input's handedness. For left-circularly polarized input, it produces an azimuthally polarized beam. Two half-wave plates, oriented at an angle θ with respect to each other, rotate an input linear polarization by 2θ. A radially polarized beam can be achieved by passing an azimuthally polarized beam through these plates with

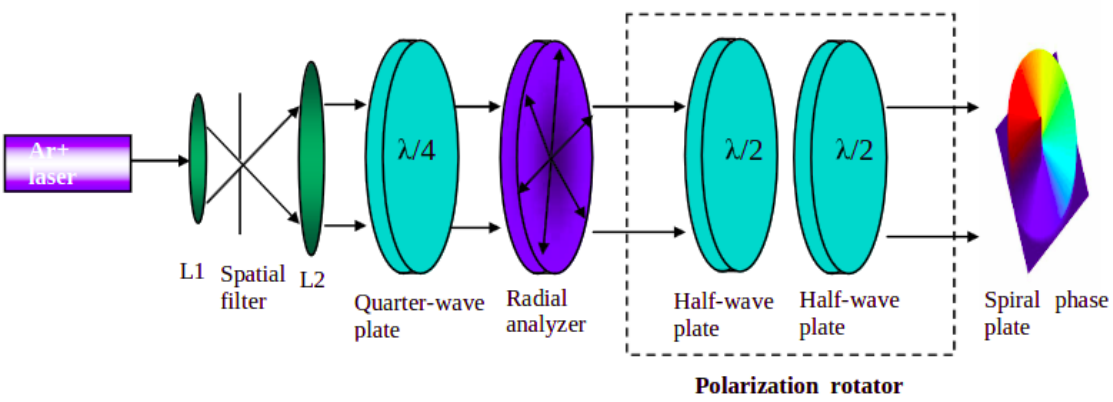

Figure 1.11: Experimental set up to generate radial and azimuthal VB [2].

$\theta = 45^0$. However, this process introduces a geometric phase (Pancharatnam–Berry phase), which is compensated by a spiral phase element of opposite helicity, achieving a true radially polarized VB.

1.8.2 State of polarization of light

The most general way to express a homogeneous plane wave propagation in the direction z is

$$E(z,t) = (\hat{e}_x \mathcal{E}_1 + \hat{e}_y \mathcal{E}_2)\, e^{i(kz-\omega t)} + c.c., \tag{1.124}$$

where $\hat{e}_x$, and $\hat{e}_y$ are the unit vectors along the transverse plane, $\mathcal{E}_1$, and $\mathcal{E}_1$ are complex field amplitude. The electric field in Eq. (1.124) is defined in the linear polarization basis. We can also define two complex orthogonal unit vectors corresponding to right and left-circular polarizations in the circular polarization basis as

$$\hat{e}_R = \frac{1}{\sqrt{2}}(\hat{e}_x + i\hat{e}_y), \quad \hat{e}_L = \frac{1}{\sqrt{2}}(\hat{e}_x - i\hat{e}_y), \tag{1.125}$$

where $\hat{e}_R$, and $\hat{e}_L$ denote the unit vector for right and left circular polarization. The electric field in the circular polarization basis now can be defined as

$$E(z,t) = (\hat{e}_R \mathcal{E}_R + \hat{e}_L \mathcal{E}_L)\, e^{i(kz-\omega t)} + c.c., \tag{1.126}$$

where $\mathcal{E}_R$, and $\mathcal{E}_L$ are complex field amplitude of the right and left circular components. There arises three cases depending on the amplitude and phase associated with both the components [31]:

- An equal superposition of right and left circular components in phase (or π out of phase) form linear polarization.
- A pure circular state has only one circular component.
- Unequal superposition or phase delay between $\mathcal{E}_R$, and $\mathcal{E}_L$ forms elliptical polarization.

A convenient and comprehensive way to describe any state of light polarization is through the four Stokes parameters. These parameters are especially significant as they form a bridge between the theoretical description of polarization and experimentally measurable quantities. The Stokes parameters are defined as follows

$$\begin{aligned} S_0 &= |\mathcal{E}_R|^2 + |\mathcal{E}_L|^2, \;\; S_1 = 2\mathrm{Re}[\mathcal{E}_R^* \mathcal{E}_L], \\ S_2 &= 2\mathrm{Im}[\mathcal{E}_R^* \mathcal{E}_L], \;\; S_3 = |\mathcal{E}_L|^2 - |\mathcal{E}_R|^2. \end{aligned} \tag{1.127}$$

It is important to note that in the Eq. (1.127), the Stokes parameter S_0 represents the total intensity, while S_1 and S_2 denote the coherence between the right and left circular components of polarization. Additionally, the parameter S_3 quantifies the predominance of left-circular polarization over right-circular polarization. The complete set of polarization states can be represented on a unit sphere known as the Poincaré sphere. This representation provides a geometric framework for understanding the state of polarization and its evolution as shown in Fig. 1.12. The surface of the sphere corresponds to fully polarized light, while points within the sphere, excluding the center, indicate partially polarized light. The center itself represents unpolarized light. Linear polarization is depicted along the equator of the sphere. The north and south poles represent right and left circular polarization,

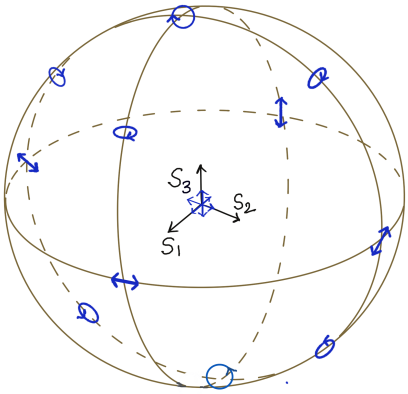

Figure 1.12: Representation of different states of polarization on the Poincaré sphere.

respectively. Intermediate points on the sphere signify elliptical polarization, where latitude indicates ellipticity and longitude denotes the orientation of the ellipse. We can calculate the ellipticity, ζ, and the orientation, ξ, of polarization at each point in the transverse plane as

$$\frac{S_1}{S_0} = \cos(2\zeta)\cos(2\xi), \quad \frac{S_2}{S_0} = \cos(2\zeta)\sin(2\xi), \quad \frac{S_3}{S_0} = \sin(2\zeta), \tag{1.128}$$

which give

$$\zeta = \frac{1}{2}\sin^{-1}\left(\frac{S_3}{S_0}\right), \quad \xi = \frac{1}{2}\tan^{-1}\left(\frac{S_2}{S_1}\right). \tag{1.129}$$

These two quantities ellipticity and orientation are essential because they provide the minimum complete description of the polarization ellipse at each point in a VB, where polarization varies across the transverse plane.

1.8.3 Application of vector beam

In recent years, VBs have been successfully utilized across various fields as light sources characterized by a spatially varying polarization profile. In the case of FP beams, the polarization encompasses entire Poincaré sphere throughout their transverse profile, as all states of polarization are represented in the transverse plane [78]. One significant application of FP beams belongs to the exploration of polarization singularities and the topological structures of light. Given that their polarization field includes all possible states, FP beams inherently feature C-points (points of circular polarization) and L-lines (lines of linear polarization) [85]. These singularities serve as foundational elements in the domain of singular optics and facilitate multidimensional information encoding. Unlike scalar beams, information can be stored not only in intensity and phase but also in the local polarization distribution, giving rise to unique propagation behaviors and unprecedented sensitivity to optical anisotropy and birefringence in various materials. It acts as polarization multiplexed probes, where each spatial position interrogates the material with a different state of polarization. This provides an intrinsic multidimensional encoding not possible with scalar beams. FP beam allows the extraction of rich structural information in liquid crystals, metasurfaces, and birefringent fibers [86, 87].

In addition to FP beams, considerable attention has been directed toward the optical properties of CV beams. The principal applications of CV beams pertain to tight focusing [76]. A radially polarized beam, when focused through a high numerical aperture objective lens, generates a strong longitudinal field at the focus. This results in a diminished focal spot and an increased intensity along the optical axis in comparison to a linearly polarized Gaussian beam. Consequently, CV beams hold considerable promise for applications in high-resolution optical microscopy [88]. Their spatially varying polarization distribution leads to polarization-dependent optical forces, making them highly effective in optical trapping and manipulation of microscopic particles [89]. It is also used in laser machining [90], magnetometry, and spatially structured transparency [91, 80]. OAM beams tend to break up into multiple soliton peaks (twice the OAM) during nonlinear propagation. This fragmentation can be suppressed by utilizing VBs instead of scalar beams [92].

The next three chapters are devoted to three distinct research problems. Chapters 2 and 3 address problems formulated within an atomic system, while Chapter 4 explores a related but separate problem in a QD system.

TH-3976_186121017

Chapter 2

Linear and nonlinear propagation of cylindrical vector beams

2.1 Introduction

The growing ability to engineer light–matter interaction has created new opportunities for studying coherence-driven optical effects. Recent advances have highlighted the importance of spatially varying polarization in shaping these interactions [93]. In this chapter, we investigate these ideas by examining the propagation of CV beams through a four-level atomic medium. Early investigations mainly considered uniform polarization states to study quantum coherence, which plays a vital role in producing interference effects [26, 94, 95, 96, 97, 98]. Although three-level systems in the Ξ, V, Λ, and Δ configurations have traditionally served as standard models, double two-level systems are now receiving significant attention because of the rich interference features they support. Notable phenomena observed in the double two-level atomic system include spontaneously generated interference in resonance fluorescence [99], efficient modulation of the medium gain for the probe pulse due to interference between the absorption and the stimulated emission paths [100], slowing light through Zeeman coherence oscillations [101], and recovery of interference in resonance fluorescence by relative phase control [102]. The coherent control of the effective susceptibility of a duplicated two-level system has been reported in [103]. The control can be achieved for a linearly polarized weak field due to the application of a significantly stronger orthogonally polarized field. Furthermore, optical bistability and multistability [104], three-dimensional atom localization [105], and anisotropic nonlinear response through quantum interference [106] involves closed-loop double two-level atomic systems.

Interest has steadily grown in VBs, whose polarization varies across the transverse plane, making them fundamentally different from scalar beams. In this work, we have presented phase-induced susceptibilities for both the components of CV beams inside an atomic vapor. The medium is composed of a non-degenerate four-level system which is excited by a strong control field and the two orthogonal polarization components of a PVB. This non-degenerate system is more realistic as the Zeeman splitting of magnetic sublevels lifts the degeneracy of a duplicated two-level system. After propagating inside the medium, the output probe beam experiences absorption or gain depending on the phase shift between the weak probe and the strong control field. Hashmi *et al.*, have achieved the control of susceptibility through

TH-3976_186121017

wave mixing[103]. The variation in the refractive index of the two components of the CV beam induces polarization rotation. The external magnetic field can control this polarization rotation [107]. Furthermore, when the intensity of the probe beam and control field are of comparable magnitude, self-focusing and defocusing in the medium can be achieved by appropriately selecting the detunings of the probe beam and control field transitions. The longitudinal profile of radial, azimuthal, and spiral CV beams show quasiperiodic nature along propagation. In several systems, self-focusing has been observed with scalar beams, including in alkali-metal vapor cell[108], condensate[109], the air on the ground[110], and waveguide arrays[111]. However, in our work, self-focusing with CV beams controls the polarization, which is deficient in scalar beams.

The arrangement of this chapter is as follows. Section 2.1 provides a succinct introduction to the importance of VB and four-level system, and our research findings. The theoretical formalism adopted in this study is presented in Sec. 2.2. Section 2.3 presents the results of our work, accompanied by comprehensive explanations. Lastly, Sec. 2.4 includes the conclusion of our work.

2.2 Theoretical formulation

2.2.1 Level system

In this work, we present a scheme based on non-electromagnetically induced gain or absorption arising from manipulating phases of the two components of a vector

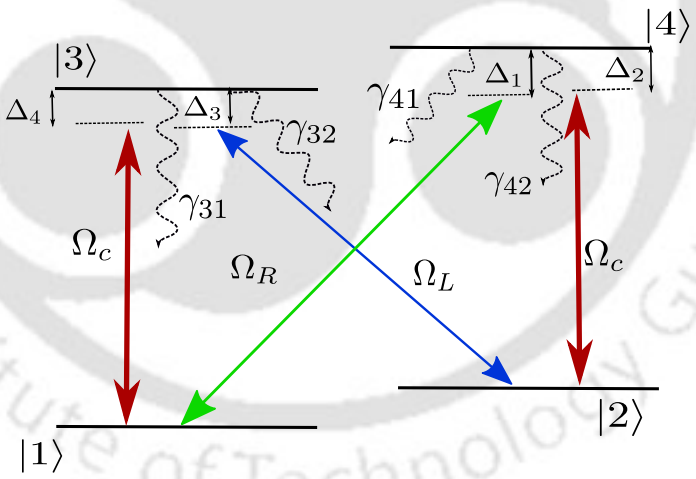

Figure 2.1: Schematic diagram of a non-degenerate four level atomic system. The right circularly polarized component, E_R, and the left circularly polarized component, E_L, of a weak probe VB drives the transitions, $|1\rangle \leftrightarrow |4\rangle$ and $|2\rangle \leftrightarrow |3\rangle$ respectively. The transition $|1\rangle \leftrightarrow |3\rangle$ and $|2\rangle \leftrightarrow |4\rangle$ are coupled by a strong control field E_c. The spontaneous emission decay rate from $|3\rangle$ and $|4\rangle$ states are given by γ_{3j} and γ_{4j} $(j \in 1, 2)$. The detunings of the transitions are denoted by Δ_i $(i \in 1, 2, 3, 4)$.

beam. The system under consideration is a non-degenerate four-level closed-loop system where the relative phase shift between various applied fields can effectively modulate the response for the probe fields. Control fields allow various quantum interference of the electronic excitation pathways that effectively compensate or overcome the linear absorptive spatial response by the non-linear response of the medium.

Previous studies on the double two-level system have garnered significant attention due to its wide range of quantum interference phenomena through the application of scalar fields [99, 100, 101, 102, 103, 104, 105, 106]. Motivated by the various aspects of the closed-loop system, we have considered a non-degenerate four-level atomic system driven by two orthogonally polarized components of a PVB and a π polarized control field as in Fig. 4.1. This configuration can be realized in ^{6}Li $D_1(2^2S_{1/2} \rightarrow 2^2P_{1/2})$ transition hyperfine structure as: $|1\rangle = |2^2S_{1/2}, F = 1/2, m_F = -1/2\rangle, |2\rangle = |2^2S_{1/2}, F = 1/2, m_F = 1/2\rangle, |3\rangle = |2^2P_{1/2}, F = 1/2, m_F = -1/2\rangle$, and $|4\rangle = |2^2P_{1/2}, F = 1/2, m_F = 1/2\rangle$. The transitions $|1\rangle \leftrightarrow |3\rangle$, and $|2\rangle \leftrightarrow |4\rangle$ are coupled by a π-polarized control field $\vec{E}_c$, which is defined as,

$$\vec{E}_c(r,t) = \hat{e}_\pi \mathcal{E}_c(r) e^{-i(\omega_c t - k_c z)} + c.c., \tag{2.1}$$

where $\hat{e}_\pi$, $\mathcal{E}_c(r)$, ω_c, k_c are the polarization vector, spatial envelop, central frequency and wavevector respectively. We can decompose a linear polarized vector probe field $\vec{E}_p$, into two orthogonally polarized basis states $\hat{\sigma}_i (i \in R, L)$ as,

$$\vec{E}_p(r,t) = \hat{e}_x \mathcal{E}_p(r) e^{-i(\omega_p t - k_p z + \beta)} + c.c. \tag{2.2a}$$

$$= \sum_{i=R,L} \hat{\sigma}_i \mathcal{E}_i(r) e^{-i(\omega_p t - k_p z + \beta)} + c.c., \tag{2.2b}$$

where $\hat{\sigma}_{R(L)}$ are the right (left) circular polarization unit vector, the right(left) circular polarized component $\mathcal{E}_{R(L)}$ components couples with the $|1\rangle \leftrightarrow |4\rangle$ ($|2\rangle \leftrightarrow |3\rangle$). The phase shift among the probe and the control fields is β.

The time-dependent Hamiltonian describing the interaction of the model system as shown in Fig. 4.1, can be written under dipole approximation as

$$\boldsymbol{H} = \boldsymbol{H}_0 + \boldsymbol{H}_I, \tag{2.3a}$$

$$\boldsymbol{H}_0 = \hbar(\omega_{21}|2\rangle\langle 2| + \omega_{31}|3\rangle\langle 3| + \omega_{41}|4\rangle\langle 4|), \tag{2.3b}$$

$$\begin{aligned} \boldsymbol{H}_I &= -\hat{d}.\vec{E} \\ &= -[\vec{d}_{41}.(\hat{e}_R \mathcal{E}_R e^{-i\omega_p t - i\beta} + c.c.)|4\rangle\langle 1| + \vec{d}_{32}.(\hat{e}_L \mathcal{E}_L e^{-i\omega_p t - i\beta} + c.c.)|3\rangle\langle 2| \\ &\quad + \vec{d}_{31}.(\hat{e}_\pi \mathcal{E}_c e^{-i\omega_c t} + c.c.)|3\rangle\langle 1| + \vec{d}_{42}.(\hat{e}_\pi \mathcal{E}_c e^{-i\omega_c t} + c.c.)|4\rangle\langle 2|] + \text{H.c.}, \end{aligned} \tag{2.3c}$$

where $\omega_{j1} (j = 2, 3, 4)$ correspond to the frequency separation between the state $|j\rangle$ and the ground state $|1\rangle$ and $\vec{d}_{ik}$ $(i = 3, 4;\ k = 1, 2)$ are the matrix elements of the induced dipole moments for the transitions $|i\rangle \leftrightarrow |k\rangle$. In order to eliminate the explicit time dependence in the Hamiltonian, we perform the following unitary transformation

$$U = \exp[-i\omega_c t|3\rangle\langle 3| - i\omega_p t|4\rangle\langle 4| - i(\omega_p - \omega_c)t|2\rangle\langle 2|]. \tag{2.4}$$

Now the effective Hamiltonian in the interaction picture is given as, $\mathcal{H} = \hat{U}^\dagger H \hat{U} - i\hbar \hat{U}^\dagger \partial_t \hat{U}$. We impose the condition $\omega_p - \omega_c = 0$, so that the time dependence is completely eliminated from the effective Hamiltonian. Under the RWA it gives

$$\begin{aligned} \mathcal{H} &= -\hbar[(\Delta_1 - \Delta_2)|2\rangle\langle 2| + \Delta_4|3\rangle\langle 3| + \Delta_1|4\rangle\langle 4|] - \hbar[\Omega_c|3\rangle\langle 1| - \Omega_L e^{-i\beta}|3\rangle\langle 2| \\ &\quad + \Omega_R e^{-i\beta}|4\rangle\langle 1| - \Omega_c|4\rangle\langle 2|] + \text{H.c.} \end{aligned} \tag{2.5}$$

The single photon detunings of the probe and control field for their respective transitions are defined as

$$\Delta_1 = \omega_p - \omega_{41},\ \Delta_2 = \omega_c - \omega_{42},\ \Delta_3 = \omega_p - \omega_{32},\ \Delta_4 = \omega_c - \omega_{31}, \tag{2.6}$$

and the Rabi frequencies of probe field components and control field is written as

$$\Omega_R = \frac{\vec{d}_{41}.\hat{e}_R}{\hbar}\mathcal{E}_R,\ \ \Omega_L = \frac{\vec{d}_{32}.\hat{e}_L}{\hbar}\mathcal{E}_L,\ \ \Omega_c = \frac{\vec{d}_{31}.\hat{e}_\pi}{\hbar}\mathcal{E}_c. \tag{2.7}$$

Note that $\vec{d}_{32} = -\vec{d}_{41}$, and $\vec{d}_{42} = -\vec{d}_{31}$ according to the Clebsch-Gordan coefficient for the $F = 1/2 \leftrightarrow F = 1/2$ level scheme. To find the population dynamics and the atomic coherence we use the following Liouville equation

$$\frac{\partial \rho}{\partial t} = -\frac{i}{\hbar}[\mathcal{H}, \rho] + \mathcal{L}\rho. \tag{2.8}$$

The second term on the right hand side of the above equation represents all the radiative and nonradiative decay processes which can be determined by

$$\mathcal{L}\rho = -\sum_{i=3}^{4}\sum_{j=1}^{2}\frac{\gamma_{ij}}{2}(|i\rangle\langle i|\rho - 2|j\rangle\langle j|\rho_{ii} + \rho|i\rangle\langle i|), \tag{2.9}$$

where γ_{ij} are the radiative decay rates from the excited state $|i\rangle$ to $|j\rangle$.

Now, the dynamics of the model system can be obtained from the following density matrix equations

$$\dot{\rho}_{11} = -i(\Omega_c\rho_{13} + \Omega_R e^{-i\beta}\rho_{14} - \Omega_c^*\rho_{31} - \Omega_R^* e^{i\beta}\rho_{41}) + \gamma_{31}\rho_{33} + \gamma_{41}\rho_{44}, \tag{2.10a}$$
$$\dot{\rho}_{22} = -i(\Omega_L e^{-i\beta}\rho_{23} - \Omega_c\rho_{24} - \Omega_L^* e^{i\beta}\rho_{32} + \Omega_c^*\rho_{42}) + \gamma_{32}\rho_{33} + \gamma_{42}\rho_{44}, \tag{2.10b}$$
$$\dot{\rho}_{33} = i(\Omega_c\rho_{13} + \Omega_L e^{-i\beta}\rho_{23} - \Omega_c^*\rho_{31} - \Omega_L^* e^{i\beta}\rho_{32}) - (\gamma_{31} + \gamma_{32})\rho_{33}, \tag{2.10c}$$
$$\dot{\rho}_{31} = i(\Omega_L e^{-i\beta}\rho_{21} + \Delta_{31}\rho_{31} + \Omega_c(\rho_{11} - \rho_{33}) - \Omega_R e^{-i\beta}\rho_{34}), \tag{2.10d}$$
$$\dot{\rho}_{32} = -i(\Delta_{32}\rho_{32} + \Omega_L e^{-i\beta}(\rho_{33} - \rho_{22}) - \Omega_c(\rho_{12} + \rho_{34})), \tag{2.10e}$$
$$\dot{\rho}_{41} = i(\Delta_{41}\rho_{41} - \Omega_c(\rho_{21} + \rho_{43}) + \Omega_R e^{-i\beta}(\rho_{11} - \rho_{44})), \tag{2.10f}$$
$$\dot{\rho}_{42} = i(\Omega_R e^{-i\beta}\rho_{12} - \Omega_L e^{-i\beta}\rho_{43} + \Delta_{42}\rho_{42} + \Omega_c(\rho_{44} - \rho_{22})), \tag{2.10g}$$
$$\dot{\rho}_{34} = i(\Omega_c\rho_{14} + \Omega_L e^{-i\beta}\rho_{24} - \Omega_R^* e^{i\beta}\rho_{31} + \Omega_c^*\rho_{32} + \Delta_{34}\rho_{34}), \tag{2.10h}$$
$$\dot{\rho}_{12} = -i(\Delta_{12}\rho_{12} + \Omega_L e^{-i\beta}\rho_{13} - \Omega_c\rho_{14} - \Omega_c^*\rho_{32} - \Omega_R^* e^{i\beta}\rho_{42}), \tag{2.10i}$$

where the overdots signify time derivatives and star $(*)$ denotes the complex conjugates. The remaining density matrix equations are derived from the population conservation law $\sum_{i=1}^{4}\rho_{ii} = 1$ and their complex conjugate expressions $\dot{\rho}_{ij} = \dot{\rho}_{ji}^*$. In Eq.(3.10), $\Delta_{31} = \Delta_4 + i\Gamma_{31}$, $\Delta_{32} = (\Delta_1 - \Delta_2 - \Delta_4) - i\Gamma_{32}$, $\Delta_{41} = \Delta_1 + i\Gamma_{41}$, $\Delta_{42} = \Delta_2 + i\Gamma_{42}$, $\Delta_{34} = (\Delta_4 - \Delta_1) + i\Gamma_{34}$, $\Delta_{12} = (\Delta_1 - \Delta_2) - i\Gamma_{12}$ and Γ_{ij} are the decoherence rates of the system.

2.2.2 Linear Response of the medium

In this section, we present an analytical expression for the atomic coherence to validate the linear response of the PVB within the medium. The PVB is to be

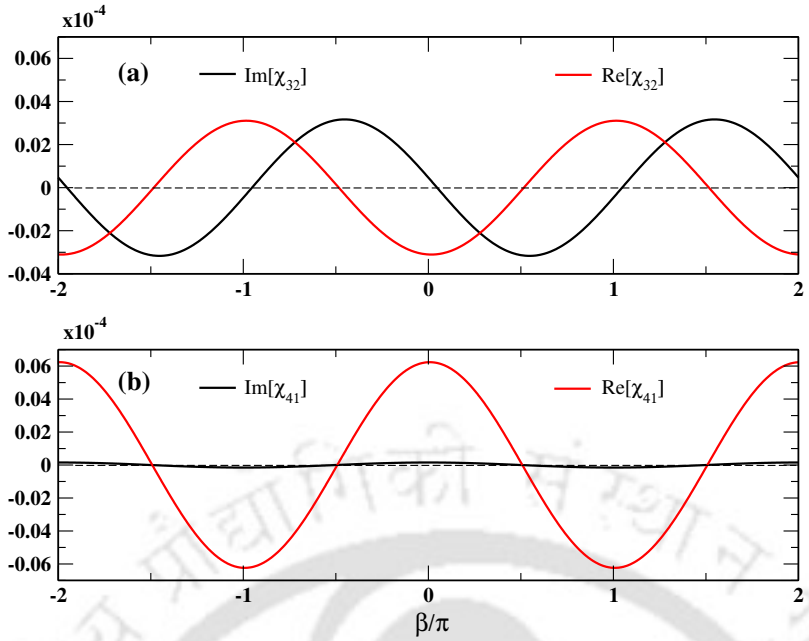

Figure 2.2: (a) Real and imaginary part of χ_{32} vs. phase shift β. (b) Real and imaginary part of χ_{41} vs. phase shift β. Parameter used: $|\Omega_{R,L}| = 0.02\gamma, \Omega_c = 2\gamma$. $\gamma_{31} = \gamma_{42} = \gamma/3$, $\gamma_{41} = \gamma_{32} = 2\gamma/3$. $\Delta_L = 0, \Delta_R = 10\gamma$. The density of atoms, $\mathcal{N} = 2 \times 10^{10}\text{cm}^{-3}$, and the free space wavenumber $k = 9.4 \times 10^4\text{rad/cm}$.

sufficiently weak ($|\Omega_{L,R}| << |\Omega_c|$) to consider it as a peturbation to a system of linear order under the steady state condition. The perturbative expansion of the density matrix upto the first order in the probe beam can be expressed as [112]

$$\rho_{ij} = \rho_{ij}^{(0)} + \Omega_L \rho_{ij}^{(1L)} + \Omega_L^* \rho_{ij}^{(1L^*)} + \Omega_R \rho_{ij}^{(1R)} + \Omega_R^* \rho_{ij}^{(1R^*)}, \tag{2.11}$$

where $\rho_{ij}^{(0)}$ describes the solution in absence of the PVB, and $\rho_{ij}^{(1k)}$ $(k \in L, L^*, R, R^*)$ represent the linear order solutions in presence of the PVB. To find the coherence, we substitute Eq. (2.11) in Eqs. (2.10) and equate the coefficients of Ω_L, Ω_L^*, Ω_R, Ω_R^*. Thus we obtain four sets of fifteen coupled linear equations. We then solve these algebraic equations to obtain the coherence which is given as

$$\rho_{32}^{1L} = -\frac{ie^{-i\beta}(A+B)}{CD}, \tag{2.12a}$$

$$\rho_{32}^{1R^*} = -\frac{ie^{i\beta}E}{CD}, \tag{2.12b}$$

$$\rho_{41}^{1R} = -\frac{ie^{-i\beta}(F+G)}{DC^*}, \tag{2.12c}$$

$$\rho_{41}^{1L^*} = -\frac{ie^{i\beta}H}{DC^*}. \tag{2.12d}$$

In Eqs. (2.12) the detailed expressions for $A - H$ are provided in the Appendix. It is pertinent to note that in the original frame of reference, the off-diagonal density matrix element ρ_{32} and ρ_{41} must be multiplied by $e^{-i\omega_p t}$. The steady-state values of ρ_{32} and ρ_{41} determine the linear susceptibility χ_{32} and χ_{41} of the medium at the frequency ω_p, respectively. We consider both the probe components are at two photon resonance, with $\Delta_1 = \Delta_2 = \Delta_R$ and $\Delta_3 = \Delta_4 = \Delta_L$. The decay rates,

$\gamma_{31} = \gamma_{42} = \gamma/3$, $\gamma_{41} = \gamma_{32} = 2\gamma/3$, and coherence decay between the states $|2\rangle$ and $|1\rangle$ being negligible, the medium's susceptibility can be expressed as follows:

$$\chi_{32}(\omega_p) = \frac{\mathcal{N}|d_{32}|^2}{\hbar}\frac{ie^{i\beta}}{\Gamma_2}\left[\Gamma_1\left(\frac{\Omega_c}{\Omega_c^*}\right)\left(\frac{\Omega_R^*}{\Omega_L}\right)+\Gamma_3 e^{-2i\beta}\right], \tag{2.13a}$$

$$\chi_{41}(\omega_p) = \frac{\mathcal{N}|d_{41}|^2}{\hbar}\frac{ie^{i\beta}}{\Gamma_5}\left[\Gamma_4\left(\frac{\Omega_c}{\Omega_c^*}\right)\left(\frac{\Omega_L^*}{\Omega_R}\right)+\Gamma_6 e^{-2i\beta}\right], \tag{2.13b}$$

where,

$$\Gamma_1 = \Gamma_R^* - \Gamma_L\Gamma_L^*;\ \ \Gamma_2 = -(\Gamma_L + \Gamma_R^*)(4|\Omega_c|^2 + \Gamma_L\Gamma_L^* + \Gamma_R\Gamma_R^*);\ \ \Gamma_3 = i\Gamma_R^*(\Delta_R - \Delta_L); \tag{2.14a}$$

$$\Gamma_4 = \Gamma_L^* - \Gamma_R\Gamma_R^*;\ \ \Gamma_5 = -(\Gamma_R + \Gamma_L^*)(4|\Omega_c|^2 + \Gamma_L\Gamma_L^* + \Gamma_R\Gamma_R^*);\ \ \Gamma_6 = i\Gamma_L^*(\Delta_L - \Delta_R); \tag{2.14b}$$

$$\Gamma_R = (i\Delta_R - 1/2);\ \ \Gamma_L = (i\Delta_L - 1/2). \tag{2.14c}$$

Here $\mathcal{N}$ is the atomic density of the medium. The expression for the susceptibilities of the transitions $|2\rangle \leftrightarrow |3\rangle$, and $|1\rangle \leftrightarrow |4\rangle$, as described herein, provide valuable insights into the physics of phase-dependent interference. Under two-photon resonance conditions, the real and imaginary parts of susceptibility for both the VB components are exhibited in Figs. 2.2(a) and 2.2(b). The positive and negative value of $\mathrm{Im}[\chi_{32}]$, and $\mathrm{Im}[\chi_{41}]$ signifies absorption and gain of the medium, respectively. This oscillatory nature as a function of the phase shift β corresponds to different quantum pathways in the closed-loop system. On the other hand, the difference in the $\mathrm{Re}[\chi_{32}]$ and $\mathrm{Re}[\chi_{41}]$ has a direct impact on the polarization rotation of the CV beam. In the latter part of this chapter, the phase shift $\beta = 0$ and $\beta = \pi/2$ are adopted. The phase shift β significantly impacts the redistribution of population and consequential changes in atomic coherence within our closed-loop system. As such, it serves as a control mechanism, resulting in either constructive or destructive interference among various excitation pathways. This feature effectively acts as a control knob for the system, enabling precise regulation of absorption and dispersion. To investigate the medium's nonlinear response, we use the Gaussian elimination method to find the relevant coherences for a probe field in all orders of probe and control fields at higher intensity limits.

2.2.3 Variation of ellipticity and orientation

We have already defined the electric field of the VB and the Stokes parameters associated with both the components in Sec. 1.8. Now, we substitute Eqs. (1.122), (1.123), and (1.127) in Eq. (1.129) assuming that the free space wave vector $k_R = k_L = k$, gives

$$\xi(z) = -\frac{1}{2}\Bigg[\theta + \phi\Delta(l_{L,R}) + kz\Delta(n_{R,L}) + \eta(z)\Delta(|l_{L,R}|) + \frac{kzr^2}{2}\Bigg\{\frac{n_R}{z^2 + n_R^2 z_R^2} - \frac{n_L}{z^2 + n_L^2 z_R^2}\Bigg\}\Bigg], \tag{2.15}$$

where $\Delta(l_{L,R}) = l_L - l_R$, $\Delta(|l_{L,R}|) = |l_L| - |l_R|$, and $\Delta(n_{R,L}) = n_R - n_L$. The two components of a CV beam have equal and opposite OAM index, which implies

$|l_R| = |l_L|$. Therefore, after propagating a distance z through the medium, the polarization of a CV beam at each point on the transverse plane rotates by an amount which is given by

$$\Delta\xi(z) = -\frac{1}{2}\left[\frac{kzr^2}{2}\left\{\frac{n_R}{z^2+n_R^2z_R^2} - \frac{n_L}{z^2+n_L^2z_R^2}\right\} + kz\Delta(n_{R,L})\right]. \tag{2.16}$$

According to the Eq. (2.16), it is evident that the polarization rotation inside the medium in the case of CV beams is attributed solely to the difference in the refractive index of the two components of the probe beam. Additionally, we can also express the variation of ellipticity for the CV beam as

$$\Delta\zeta(z) = \frac{1}{2}\left[\sin^{-1}\left\{\frac{1-a\tan^2\alpha}{1+a\tan^2\alpha}\right\} - \sin^{-1}\left\{\frac{1-\tan^2\alpha}{1+\tan^2\alpha}\right\}\right], \tag{2.17}$$

where,

$$a = \exp\left[-\frac{2r^2}{w_0^2}\left(\frac{n_R^2z_R^2}{z^2+n_R^2z_R^2} - \frac{n_L^2z_R^2}{z^2+n_L^2z_R^2}\right)\right]\left\{\frac{n_R^2(z^2+n_L^2z_R^2)}{n_L^2(z^2+n_R^2z_R^2)}\right\}. \tag{2.18}$$

2.2.4 Propagation equation

The study of beam propagation equations is crucial to explore the effect of absorption, diffraction, dispersion, and anisotropicity on VB propagation. Under the slowly varying envelope and paraxial wave approximations, the propagation equations for the right and left circularly polarized components of the probe VB can be expressed as

$$\frac{\partial\Omega_R}{\partial z} = \frac{i}{2k_R}\nabla_\perp^2\Omega_R + \frac{2\pi ik_R\mathcal{N}|d_{14}|^2}{\hbar}\rho_{41}, \tag{2.19a}$$

$$\frac{\partial\Omega_L}{\partial z} = \frac{i}{2k_L}\nabla_\perp^2\Omega_L + \frac{2\pi ik_L\mathcal{N}|d_{23}|^2}{\hbar}\rho_{32}. \tag{2.19b}$$

The first term on the right-hand side of the above equation is accountable for diffraction, and the second term represents the dispersion and absorption of the probe VB. Moderate gain or low absorption is required to propagate a VB through the medium so that the gain or absorption of the medium cannot distort the beam's spatial profile. The propagation dynamics of the strong control fields $\vec{E}_c$ are ignored due to their geometrical structure and polarisation characteristics. The split-step Fourier method (SSFM) has been chosen to study the Eqs. (2.19a) and (2.19b) numerically. In instances with a weak probe and a strong control field, the resulting outcomes align perfectly with the coherences calculated via the perturbation technique, as outlined in Eq. (2.11).

2.3 Numerical Results

2.3.1 Control of linear susceptibility

In this section, we have explored phase-induced medium susceptibilities for both components of the probe field that involve two-photon resonance conditions as in

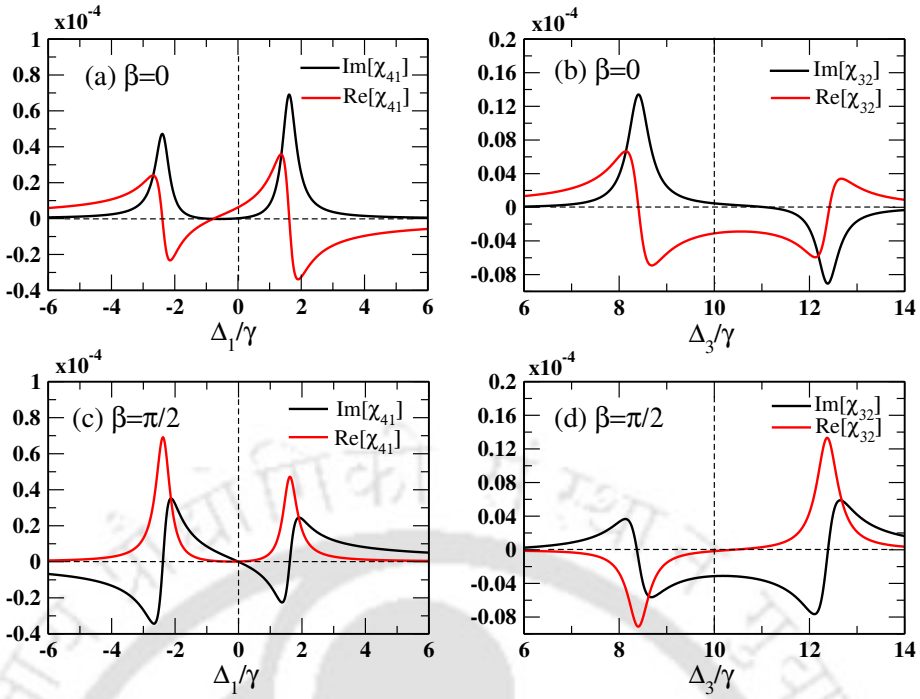

Figure 2.3: Real and imaginary part of χ_{41} and χ_{32} is plotted against the corresponding transition detunings. (a), (b) correspond to $\beta = 0$, plotted against Δ_1/γ and Δ_3/γ respectively. Similarly (c), (d) correspond to $\beta = \pi/2$, plotted against Δ_1/γ and Δ_3/γ respectively. Parameter used: $|\Omega_{R,L}| = 0.02\gamma, \Omega_c = 2\gamma$. $\gamma_{31} = \gamma_{42} = \gamma/3$, $\gamma_{41} = \gamma_{32} = 2\gamma/3$. $\Delta_2 = 0, \Delta_4 = 10\gamma$. The density of atoms, $\mathcal{N} = 2 \times 10^{10}\text{cm}^{-3}$.

Fig. 2.2. It is evident from Figs. 2.3(a)-(d) how the absorption (or gain), and dispersion are sensitive due to the phase shift between the probe and control field at two different values of $\beta = 0$, and $\beta = \pi/2$. The susceptibility at two-photon resonance for both VB components precisely matches our analytical result presented in Fig. 2.2. The asymmetric nature at the two-photon resonance condition ($\Delta_1 = 0$ or $\Delta_3 = 10\gamma$) comes from significant positive detuning Δ_4 of the control field. Depending on the phase shift, the response of the medium on the CV beams is shown in Figs. 2.4(a) and 2.4(b) at a distance z_R. Note that we work in the paraxial regime throughout the work, which is valid since our beam waist is much larger than the wavelength. Moreover, the vector superposition of the LG beam corresponds to the solution of the paraxial wave equation in cylindrical coordinates. In the case of $\beta = 0$, we observe absorption for the CV beams such as radial, azimuthal and spiral, which is illustrated in Fig. 2.4(a). Certainly, the destructive interference between the quantum pathways causes this phenomenon. However, for $\beta = \pi/2$, the medium shows substantial gain for all three kinds of CV beams, as shown in Fig. 2.4(b). This is attributed to the constructive interference phenomena. Therefore, the coupling between the dispersion and gain is shown in Figs. 2.3(a)-(d) allows a phase control of the response of the medium. Thus, it is possible that we can turn an absorber at $\beta = 0$ into an amplifier at $\beta = \pi/2$.

We further investigate the SOP of input at $z = 0$ and the output beam at a distance z_R as shown in Figs. 2.5(a)-(i). As stated earlier, achieving the desired polarization state relies on the spatial intensity distribution of both components of the vector beam. Figures 2.5(a)-(c) exhibit the initial transverse intensity and polarization distribution of radial, azimuthal, and spiral CV beams, respectively.

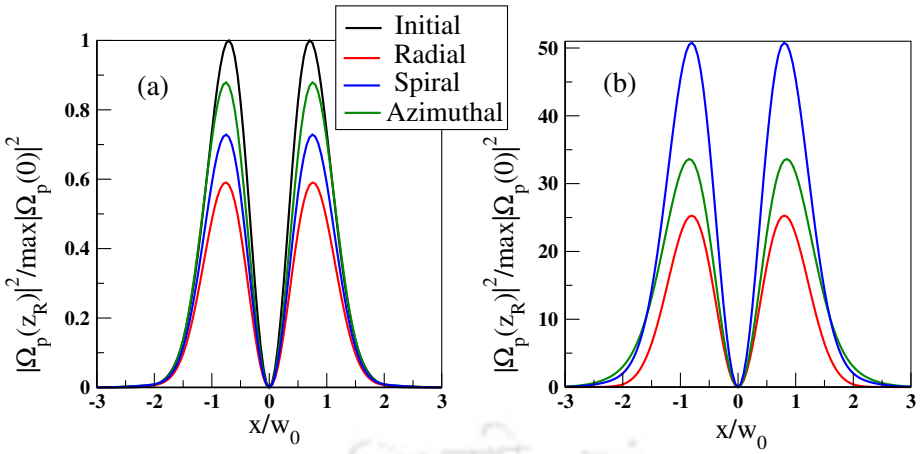

Figure 2.4: Normalized probe intensity is plotted against the transverse coordinate for different values of β. (a) For $\beta = 0$ the medium shows absorption, and (b) for $\beta = \pi/2$ it exhibits gain. The work maintains a consistent beam waist of $w_0 = 60\mu$m, throughout. The definitions of CV beam ($l_L = -1, l_R = 1$): Radial($\alpha = \pi/8, \theta = 0$), (b) azimuthal($\alpha = \pi/8, \theta = \pi$), (c) spiral($\alpha = \pi/8, \theta = -\pi/2$). We choose $\Delta_1 = 0$ and the other parameters are same as Fig. 2.3.

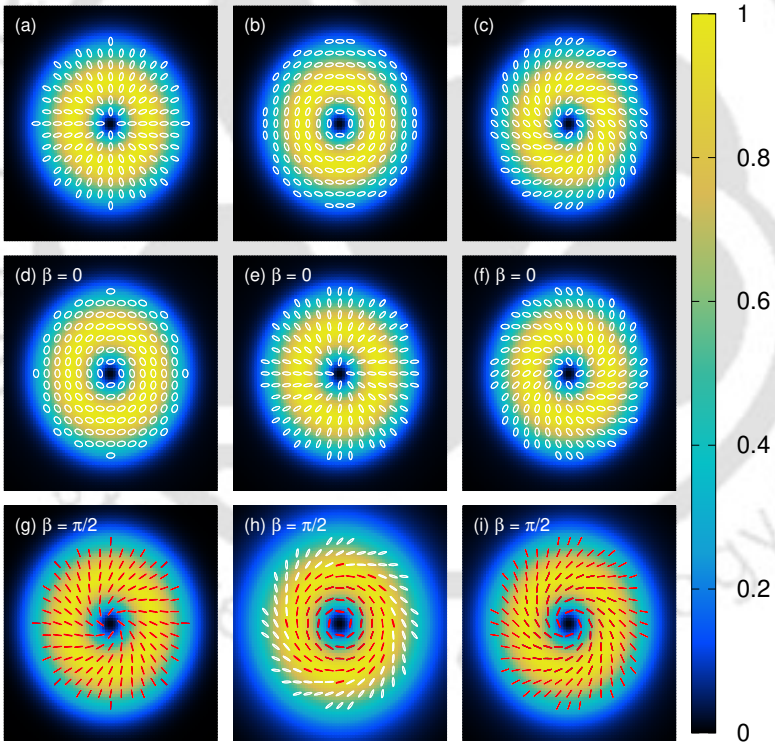

Figure 2.5: Transverse intensity and polarization distribution of CV beams. (a) Radial, (b) azimuthal, (c) spiral at $z = 0$. (d)-(f) For $\beta = 0$ (radial, azimuthal, and spiral respectively) at $z = z_R$. (g)-(i) For $\beta = \pi/2$ (radial, azimuthal, and spiral respectively) at $z = z_R$. The colors white, and red correspond to left circular, linear polarizations, respectively. The other parameters are same as Fig. 2.3.

The intensity distribution has been normalized with its maximum intensity for all figures, enabling us to visualize the diffraction it poses. It is noticed from the Figs. 2.5(d)-(f) that under the condition of $\beta = 0$, the change in the polarization state

is a consequence of the difference between Re[χ_{41}] and Re[χ_{32}]. We also observed that after propagating a length z_R inside the medium, the radial CV beam was transformed into azimuthal and vice versa. However, the clockwise spiral CV beam changed to an anticlockwise spiral. This phenomenon arises because at each point in the transverse plane, the polarization rotates $\pi/2$. So, it is certain that the second term in Eq. (2.16) dominates. On the other hand, when $\beta = \pi/2$, the polarization rotation is smaller than in the former case, although there is a variation in ellipticity as shown in Figs. 2.5(g)-(i). For the case of radial and spiral CV beams, the ellipticity decreases and forms linear polarization along the transverse plane. Meanwhile, we also notice a variation of ellipticity along the radial direction for azimuthal VB. This variation of ellipticity can be connected to Eqs. (2.17) and (2.18). As can be seen from Eq. (2.18) for $z \neq 0$, the variation of ellipticity is a function of spatial coordinates. Therefore, we showed how the polarization and ellipticity change due to the choice of the phase shift among the input fields.

2.3.2 Focusing of CV beams

In this section, we discuss the focusing of CV beams that result from the nonlinear ef-

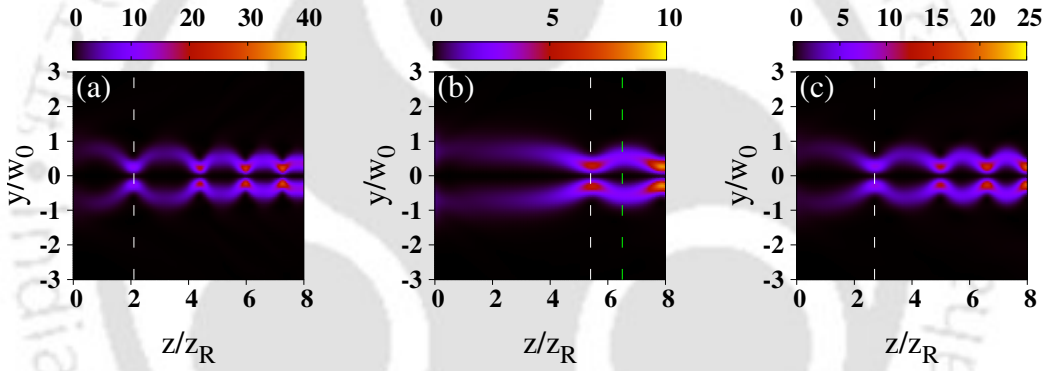

Figure 2.6: Longitudinal intensity profile of (a) radial, (b) azimuthal, and (c) sprial CV beams. Parameter used: $|\Omega_{R,L}| = 3\gamma, \Omega_c = 4\gamma$. $\Delta_1 = -1.8\gamma, \Delta_2 = 0.15\gamma, \Delta_4 = 13\gamma$, $\beta = 0$, $\mathcal{N} = 4 \times 10^{11}\text{cm}^{-3}$. White dashed vertical line denotes the first focal point for each beam, and the green dashed line represents a typical defocused point for azimuthal CV beam.

fect of the medium. The calculation of coherences, as stated earlier, is no longer valid under weak probe approximation at the strong intensity of CV beams. Therefore, a full numerical solution is desirable. Figures 2.6(a)-(c) illustrate the longitudinal profile of radial, azimuthal, and spiral CV beams, respectively. At strong probe intensities, a phenomenon referred to as "self-focusing" emerges due to the dominant character of the medium's third-order nonlinearity. The white vertical dotted line in Figs. 2.6(a)-(c) indicates the lengths at which the first focal spots for radial, azimuthal, and spiral CV beams are formed. These lengths are $2.1z_R$, $5.3z_R$ and $2.7z_R$ for radial, azimuthal and spiral CV beams, respectively. However, the distance of the focal spots may vary depending on the detunings Δ_1 and Δ_2. These detunings are the controlling parameters for the refractive index with optimal gain experienced by the beam propagating through the medium. As the beam propagates through the medium, its intensity increases at the consecutive focal points. Therefore, the beams get distorted at a larger distance due to high gain in the medium. This unique

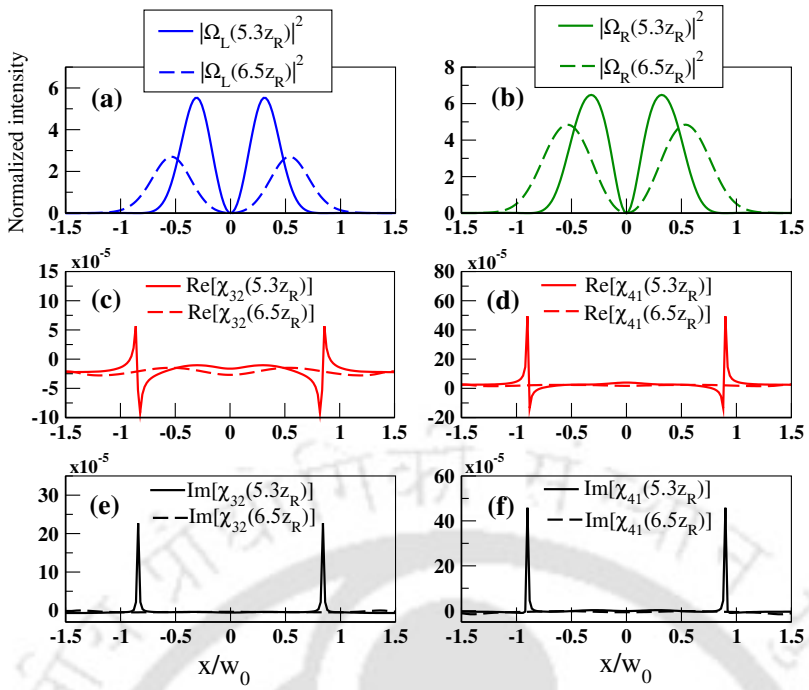

Figure 2.7: (a)-(b) Illustrate the transverse intensity profile of left and right circular components of azimuthal CV beam (at $z = 5.3z_R$, and $z = 6.5z_R$) respectively which are normalized to the respective peak intensity at $z = 0$. (c)-(d) Shows the Re$[\chi_{32}]$, and Re$[\chi_{41}]$ for both the two components (at $z = 5.3z_R$, and $z = 6.5z_R$) respectively. (e)-(f) Represent the Im$[\chi_{32}]$, and Im$[\chi_{41}]$ for both the two components (at $z = 5.3z_R$, and $z = 6.5z_R$) respectively. Parameters remain same as Fig. 2.6.

chain-like focusing pattern holds significance in optical trap chains in an optical trap system. To comprehend the mechanism behind such focusing, we have plotted the spatial susceptibilities of azimuthal CV beams for two different distances, as shown in Figs. 2.7(c)-(f). Figures 2.7(a) and 2.7(b) depict the intensity distribution of the left and right circularly polarized components of the azimuthal CV beam at the first focusing and defocusing point marked by the dashed vertical lines (white and green respectively) in Fig. 2.6(b). The intensities are normalized with the peak intensities at the input for both probe components. We have observed that both components of the probe VB have been first focused at a distance of $z = 5.3z_R$ and defocused at $z = 6.5z_R$. This phenomenon of focusing and defocusing can be elucidated by referring to Figs. 2.7(c)-(f). Figures 2.7(c) and 2.7(d), delineate that the Re$[\chi_{32}]$ and Re$[\chi_{41}]$ for both probe components display higher values at the central region around $x = 0$ for $5.3z_R$ compared to $6.5z_R$. This small difference in the refractive index is adequate to cause beam focusing and defocusing. Additionally, in Figs. 2.7(e)-(f), the small negative value of Im$[\chi_{32}]$, and Im$[\chi_{41}]$ around $x = 0$ resembles gain. This explanation for beam focusing and defocusing also applies to radial and spiral CV beams. Figures 2.8(a)-(c) demonstrate the SOP at the first focal point for the radial, azimuthal, and spiral CV beam; respectively. It is observed that the focused beams at different propagation distances experience polarization rotation. The three types of CV beams all transform a spiral, resulting in a change in handedness for the initial spiral beam. This observed polarization rotation occurs due to the refractive index disparity between two components as described in Eq. (2.16). To visualize the beam narrowing, all figures in Figs. 2.8(a)-(c) have been normalized with their respective

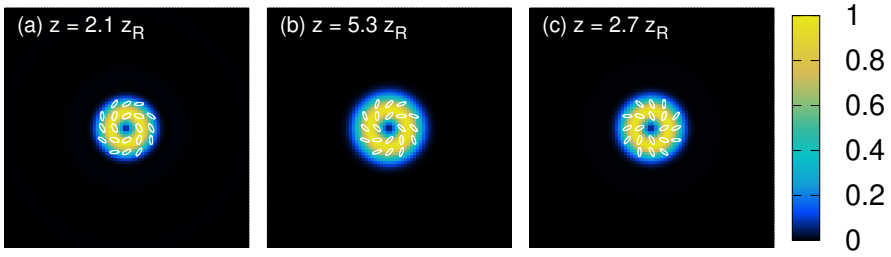

Figure 2.8: (a)-(c) Transverse intensity and polarization distribution at the first focal point for radial, azimuthal, and spiral CV beams respectively. The intensity is normalized by its maximum intensity for each VB. Parameters remain same as Fig. 2.6.

maximum peak intensity. It is evident that the spot size of the first focal spot varies for the radial, azimuthal and spiral CV beams. Figures. 2.9(a)-(c) illustrate the spot size of the radial, azimuthal, and spiral CV beams at the input and their respective first focal points. As the consecutive focal points have almost the same beam narrowing for each type of beam, we have chosen to measure the spot size only at the first focal point for all three CV beams. At $z = 0$, the spot size at full width half maxima (FWHM) of the central dark region is $0.68w_0$ for the input beam. Upon focusing, the spot size of the radial, azimuthal, and spiral CV beams have reduced to $0.28w_0$, $0.32w_0$, and $0.30w_0$, respectively, at FWHM. Therefore, the suitable choice of intensity and detunings are indispensable to induce a suitable refractive index in the medium to achieve nonlinear focusing.

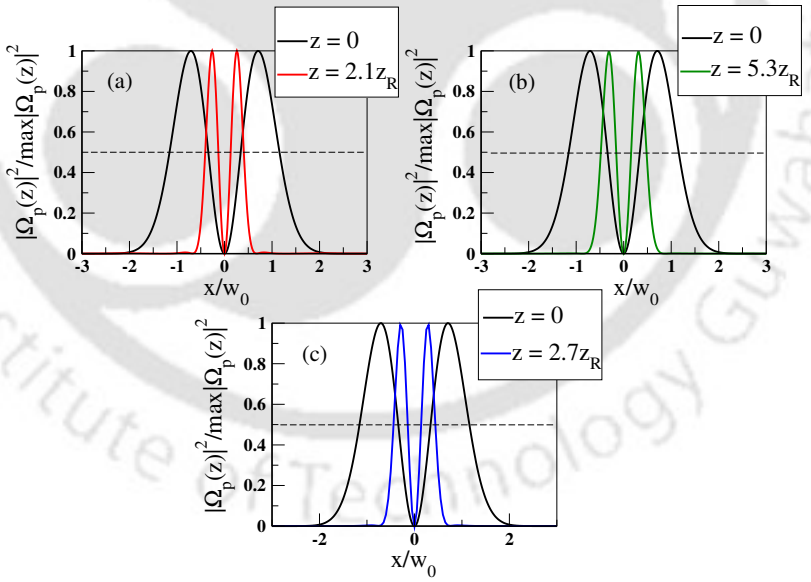

Figure 2.9: (a)-(c) Transverse intensity profile of radial, azimuthal, and spiral CV beams respectively at $z = 0$ and at first focal point. The black dotted line corresponds to half of the maximum intensity. Parameters remain same as Fig. 2.6.

2.4 Discussion

The significance of a nondegenerate four-level closed-loop atomic system lies in its capability to control light–matter interaction through quantum interference governed

by the relative phases of the applied laser fields. In contrast to open systems, such closed-loop configurations provide multiple excitation pathways that can interfere with each other, enabling precise tuning of the medium's optical response, including absorption, dispersion, and nonlinear effects [106, 113]. In the context of singular optics, a major challenge is preserving the integrity of complex field topologies, such as the spatially varying polarization of CV beams during propagation through dispersive or lossy media [114]. The present study addresses this challenge by examining CV beam propagation in a multilevel atomic system where phase-dependent control and nonlinear interactions are explicitly incorporated. This helps bridge an important gap in the existing literature, where such effects have not been comprehensively explored. Our analysis shows that the chosen nondegenerate four-level configuration serves as a highly tunable platform for manipulating CV beams. Moreover, the results provide experimentally relevant predictions and practical parameter regimes, thereby strengthening the link between theoretical modeling and potential laboratory implementation. The findings highlight the usefulness of such systems for applications in advanced microscopy, optical manipulation, and controlled propagation of the CV beams [88, 92].

2.5 Conclusion

In summary, we have developed a theoretical framework to manipulate the susceptibility of a medium to achieve gain or loss depending on the phase shift between a probe beam and a control field. Additionally, we have observed self-focusing of different CV beams at higher densities of the medium and higher intensities of the probe and control fields in a non-degenerate four-level atomic system. The system is characterized by coupled transitions via the left and right circularly polarized components of the PVB and the π polarized control field. By adjusting the phase shift between the probe beam and the control field, we can modify the susceptibility of the medium to exhibit loss at $\beta = 0$ and gain at $\beta = \pi/2$. We have also studied the polarization rotation for these two cases and found that for $\beta = 0$, the polarization ellipse rotates 90 degrees at each point in the transverse plane after propagating one Rayleigh length. Moreover, for $\beta = \pi/2$, we notice a change in ellipticity is accompanied by polarization rotation. Furthermore, we investigated the medium response when the probe beam intensity became comparable to the control field intensity. At higher atomic density, we have observed self-focusing behaviour for all three types of CV beams due to the emergence of third-order nonlinearity. Upon propagation by a couple of Rayleigh lengths, the beams exhibit a chain-like self-focusing and defocusing pattern. The SOP is described at the first focal point of each beam. The application of self-focusing has resulted in a reduction in the spot size of the beams, which could prove beneficial in enhancing resolution. Additionally, the chain-like pattern observed may hold significance in the realm of optical trap systems.

Chapter 3

Comparative study of focusing with scalar and vector beams

3.1 Introduction

The self-focusing dynamics identified in the preceding chapter emphasize the significant role of nonlinear optical effects in shaping the propagation of CV beams. Motivated by these observations, the present chapter focuses on the characteristics for light focusing with scalar and VB in a four level system. Precise control over light focusing is essential for minimizing diffraction, dispersion, and absorption—key factors that limit performance in image processing, high-resolution imaging, and optical lithography. The dispersive properties can be effectively manipulated by applying a coherent field to an unoccupied transition [115, 116, 117]. This method of dispersion engineering has yielded significant advancements and has fostered compelling applications in the field of nonlinear optics [118, 119]. The phenomenon of self-focusing of light within a nonlinear medium has emerged as a topic of considerable significance [36, 120, 121]. Typically, the self-focusing of an optical beam is attributed to the nonlinear optical Kerr effect, representing a universal nonlinear phenomenon observed across a wide range of optical domains. Kerr induced self-focusing in plasmas was first proposed in 1962 [122], with its theoretical model soon established [123, 124]. It was later confirmed experimentally by Lallemand *et al.* and analytically explained by Vlasov *et al.* [125, 126, 127]. In a Kerr nonlinear system, an optical beam can undergo evolution resulting in spikes of infinite amplitude over a finite propagation distance. This phenomenon is referred to as wave collapse. The physical phenomenon of wave collapse has been observed in various contexts such as plasma waves [128, 129], Bose-Einstein condensates or matter waves [130], capillary-gravity waves in deep water [131], and astrophysics [132]. Moreover, self-focusing and filamentation of the optical field have been observed in transparent media as well as in absorptive resonance gases [133, 134]. It is noteworthy that during focusing, a high-power laser beam may experience stimulated Raman scattering (SRS), resulting in the majority of its energy being transferred to a Stokes wave [135]. The concept of gain-focusing associated with propagation in water is discussed in further detail in [136].

Kerr nonlinearity, which is crucial for the majority of nonlinear processes, has traditionally been realized in passive optical media, such as glass-based optical fibers [137]. In passive optical media, nonlinear effects are relatively weak. Achieving

TH-3976_186121017

sufficient nonlinear phase shifts requires a long propagation distance or high light intensities. Electromagnetically induced transparency (EIT) has garnered significant attention in highly resonant optical media [138]. Quantum coherence and interference, induced by a control field, drastically reduce the absorption of a weak probe field. A strong one-photon resonance tuning mitigates the medium's opacity. This effect makes an otherwise opaque optical medium transparent [135, 136, 137]. The propagation of electromagnetic pulse in EIT systems demonstrates both a substantial reduction in group velocity and an enhancement of Kerr nonlinearity. These characteristics have prompted to explore soliton-pair solutions within EIT systems [139, 140]. Additionally, contemporary theoretical investigations have predicted a diverse array of fractional solitons [141, 142, 143]. The enhancement of Kerr nonlinearity at various transparency frequencies has been examined [144, 145]. Moreover, Mukherjee *et al.* have conducted investigations into the impact of quintic nonlinearity on modulation instability in multiple coupled quantum wells [146]. They have also analyzed modulation instability influenced by the relative phase of applied optical fields in the EIT regime [147]. Numerous theoretical efforts have been made to exploit the robust interactions of Rydberg atoms for the realization of Kerr nonlinearity [148, 149, 150, 151]. In contrast to the absorptive characteristics of the EIT framework, the Active Raman Gain (ARG) approach has attracted substantial theoretical and experimental focus [152, 135, 153]. The fundamental principle underlying the ARG scheme involves the amplification of the probe field through stimulated absorption facilitated by the control field. This system is operationally effective at ambient temperatures, which reduces both signal attenuation and distortion [154]. Significant attention has been devoted to the study of third-order self-Kerr [155, 156, 157] and cross-Kerr nonlinear responses [158, 159]. The anisotropic Kerr nonlinearity may be utilized in nonlinear optical characterization techniques and applications for light manipulation [160, 161]. Among other nonlinear process, the physical mechanism for nonlinear trapping has been recently reported [162, 163]. Following its successful application in atomic systems, the exploration of nonlinear optical properties has seamlessly progressed into the domain of semiconductor quantum wells and quantum dots [164, 165, 166].

In this study, we present an investigation into the focusing properties of scalar and VBs within a four-level arrangement that employs an ARG scheme. A comparative analysis is performed on the focusing effects associated with probe scalar beams and VBs. It has been observed that cross-Kerr-induced focusing occurs with scalar beams, while VBs experience gain-induced narrowing. Importantly, under conditions of two-photon resonance, the probe beam can achieve focusing or narrowing within the medium through a careful selection of input beam intensity. To substantiate our findings, we employ the probability-amplitude method for the calculation of both linear and third-order nonlinear susceptibilities of the probe beams. Additionally, we investigate the polarization state of the VB at the point of minimum beam radius. The resultant narrowing of the VB leads to a reduction in spot size, indicating significant potential for applications aimed at enhancing resolution.

This chapter is organized as follows. Section 3.1 provides a concise introduction to the concepts of light focusing, Kerr nonlinearity, their applications, and the findings from our research. The theoretical framework utilized in this study is outlined in Sec. 3.2. Section 3.3 details the results obtained from the investigation of probe scalar beam, supplemented by thorough explanations. In Sec. 3.4, we conduct a

comparative analysis with vector probe beam, offering clarifying insights throughout. Finally, Sec. 3.5 presents the conclusions drawn from our study.

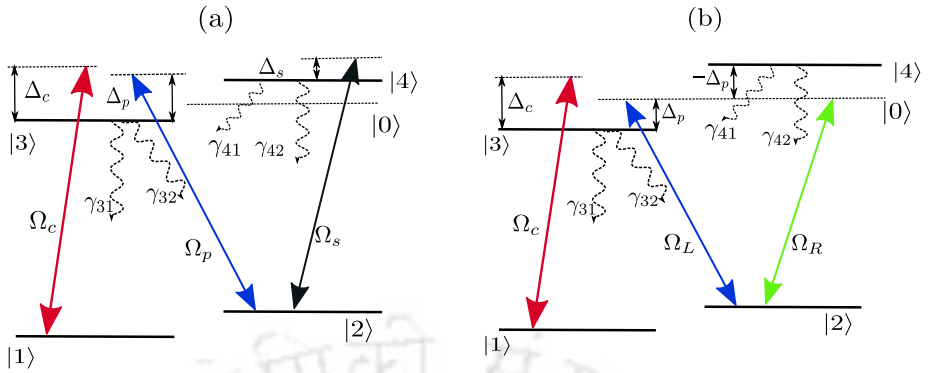

Figure 3.1: Schematic diagram of a four-level active-Raman-gain system. (a) Corresponds to the scalar probe connected to $|2\rangle \leftrightarrow |3\rangle$, and a signal field to $|2\rangle \leftrightarrow |4\rangle$ transition with a strong control field coupled to $|1\rangle \leftrightarrow |3\rangle$ transition. The probe, control, and signal detunings are denoted by Δ_p, Δ_c, and Δ_s respectively. (b) The probe beam is a VB. The right circularly polarized component, E_R, and the left circularly polarized component, E_L, of a weak probe VB drives the transitions, $|2\rangle \leftrightarrow |4\rangle$ and $|2\rangle \leftrightarrow |3\rangle$ respectively. The transition $|1\rangle \leftrightarrow |3\rangle$ is coupled by a strong control field E_c. The spontaneous emission decay rate from $|3\rangle$ and $|4\rangle$ states are given by γ_{3j} and γ_{4j} $(j \in 1, 2)$.

3.2 Theoretical formulation

3.2.1 Level system

In this work, we conduct a systematic theoretical investigation of the focusing characteristics of scalar and VBs within a four-level ARG system. We demonstrate that both the linear and nonlinear properties of the probe beam significantly influence its propagation within the medium. Previous research has revealed intriguing phenomena associated with wave propagation in resonant optical media that feature an ARG core, supported by both theoretical and experimental findings [167, 168, 169]. Inspired by these investigations, this work focuses on an ARG scheme involving two distinct configurations, utilizing a scalar probe beam and a VB, as illustrated in Figs. 3.1(a) and 3.1(b), respectively. We first address the scenario involving the scalar probe beam, followed by a discussion of the vector counterpart, concluding with a comparative analysis of the results from both configurations.

The implementation of the ARG scheme can be realized effectively in ^{87}Rb $D_2(5^2S_{1/2} \rightarrow 5^2P_{3/2})$ transition hyperfine structure as: $|1\rangle = |5^2S_{1/2}, F = 1, m_F = 0\rangle, |2\rangle = |5^2S_{1/2}, F = 2, m_F = 0\rangle, |3\rangle = |5^2P_{3/2}, F = 1, m_F = -1\rangle$, and $|4\rangle = |5^2P_{3/2}, F = 1, m_F = 1\rangle$. The probe, control and the signal field is denoted as

$$\vec{E}_j(r,t) = \hat{e}_j \mathcal{E}_j(r) e^{-i(\omega_j t - k_j z)} + c.c., \tag{3.1}$$

where $\hat{e}_j$, $\mathcal{E}_j(r)$, ω_j, k_j are the polarization vector, spatial envelop, carrier frequency and wavevector respectively. The index $j \in p, c, s$ represents probe, control, and signal field respectively.

The time-dependent Hamiltonian describing the interaction of the model system as shown in Fig. 3.1(a), can be written under dipole approximation as

$$\begin{aligned}
\boldsymbol{H} =& \boldsymbol{H}_0 + \boldsymbol{H}_I, && \text{(3.2a)}\\
\boldsymbol{H}_0 =& \hbar(\omega_{21}|2\rangle\langle 2| + \omega_{31}|3\rangle\langle 3| + \omega_{41}|4\rangle\langle 4|), && \text{(3.2b)}\\
\boldsymbol{H}_I =& -\hat{d}.\vec{E}\\
=& -[\vec{d}_{42}.(\hat{e}_s\mathcal{E}_s e^{-i\omega_s t} + c.c.)|4\rangle\langle 2| + \vec{d}_{32}.(\hat{e}_p\mathcal{E}_p e^{-i\omega_p t} + c.c.)|3\rangle\langle 2|\\
&+ \vec{d}_{31}.(\hat{e}_c\mathcal{E}_c e^{-i\omega_c t} + c.c.)|3\rangle\langle 1|] + \text{H.c.}, && \text{(3.2c)}
\end{aligned}$$

where $\omega_{j1}(j = 2, 3, 4)$ correspond to the frequency separation between the state $|j\rangle$ and the ground state $|1\rangle$ and $\vec{d}_{3k}$ $(k = 1, 2)$, $\vec{d}_{42}$ are the matrix elements of the induced dipole moments for the transitions $|3\rangle \leftrightarrow |k\rangle$, and $|4\rangle \leftrightarrow |2\rangle$ respectively. In order to eliminate the explicit time dependence in the Hamiltonian, we perform the following unitary transformation

$$U = \exp[-i\omega_c t|3\rangle\langle 3| - i(\omega_c - \omega_p)t|2\rangle\langle 2| - i(\omega_s + \omega_c - \omega_p)t|4\rangle\langle 4|]. \quad \text{(3.3)}$$

Now the effective Hamiltonian in the interaction picture is given as, $\mathcal{H} = \hat{U}^\dagger H\hat{U} - i\hbar\hat{U}^\dagger\partial_t\hat{U}$. Under the RWA it gives

$$\begin{aligned}
\mathcal{H} =& -\hbar[(\Delta_c - \Delta_p)|2\rangle\langle 2| + \Delta_c|3\rangle\langle 3| + (\Delta_c + \Delta_s - \Delta_p)|4\rangle\langle 4|] - \hbar[\Omega_c|3\rangle\langle 1|\\
&+ \Omega_p|3\rangle\langle 2| + \Omega_s|4\rangle\langle 2|] + \text{H.c.} && \text{(3.4)}
\end{aligned}$$

The single photon detunings of the probe and control field for their respective transitions are defined as

$$\Delta_c = \omega_c - \omega_{31},\ \Delta_p = \omega_p - \omega_{32},\ \Delta_s = \omega_s - \omega_{42}, \quad \text{(3.5)}$$

and the Rabi frequencies of probe field components and control field is written as

$$\Omega_c = \frac{\vec{d}_{31}.\hat{e}_c}{\hbar}\mathcal{E}_c,\ \ \Omega_p = \frac{\vec{d}_{32}.\hat{e}_p}{\hbar}\mathcal{E}_p,\ \ \Omega_s = \frac{\vec{d}_{42}.\hat{e}_s}{\hbar}\mathcal{E}_s. \quad \text{(3.6)}$$

The dynamics of the system can be determined by the subsequent equations of motion [170]

$$\begin{aligned}
&i\dot{C}_1 + \Omega_c^* C_3 = 0, && \text{(3.7a)}\\
&i\dot{C}_2 + d_2 C_2 + \Omega_p^* C_3 + \Omega_s^* C_4 = 0, && \text{(3.7b)}\\
&i\dot{C}_3 + d_3 C_2 + \Omega_c C_1 + \Omega_p C_2 = 0, && \text{(3.7c)}\\
&i\dot{C}_4 + d_4 C_4 + \Omega_s C_2 = 0, && \text{(3.7d)}
\end{aligned}$$

where, $\sum_{i=1}^{4}|C_i|^2 = 1$, $C_i(i \in 1 \text{ to } 4)$ is the probability amplitude of the bare state. In Eqs.(3.7a)-(3.7d), $d_2 = (\Delta_c - \Delta_p + i\gamma_2)$, $d_3 = (\Delta_c + i\gamma_3)$, $d_4 = (\Delta_c + \Delta_s - \Delta_p + i\gamma_4)$ with $\gamma_j(j \in 2 \text{ to } 4)$ being the atomic decay rates from the states $|j\rangle$.

3.2.2 Giant cross-Kerr nonlinearity

In central symmetric materials, all even-order nonlinearities are identically equal to zero, resulting in the third-order nonlinearity being the lowest-order nonvanishing

nonlinear optical susceptibility [32]. Specifically, Kerr nonlinearity pertains to the third-order nonlinear optical susceptibility ($\chi^{(3)}$), which gives rise to the Kerr effect. The optical Kerr nonlinearity facilitates the propagation of ultrashort soliton-type pulses without temporal spreading. There is a strong preference for large third-order nonlinear susceptibilities under conditions of low optical power and high sensitivity. These properties can be effectively harnessed for the realization of single-photon nonlinear devices [171, 172]. To achieve this, it is essential for the linear susceptibilities to be minimized in comparison to the nonlinear susceptibilities. The Kerr effect manifests as an intensity-dependent alteration in the refractive index of a material, and is characterized by the real part of third order optical susceptibilities. The probe field susceptibility is precisely defined as

$$\chi_{32} = \frac{\mathcal{N}|d_{23}|^2}{\hbar}\left(\frac{C_3 C_2^*}{\Omega_p}\right) \simeq \chi_p^{(1)} + \chi_{pp}^{(3)}|\Omega_p|^2 + \chi_{ps}^{(3)}|\Omega_s|^2, \tag{3.8}$$

where, the linear probe susceptibility is denoted as $\chi_p^{(1)}$, while the third order self and cross Kerr susceptibilities are represented as $\chi_{pp}^{(3)}$ and $\chi_{ps}^{(3)}$ respectively. We solve Eqs. (3.7a)-(3.7d) under steady-state conditions. The probability amplitudes are obtained by satisfying the condition $\sum_{i=1}^{4}|C_i|^2 = 1$. Hence

$$C_1 = \left[1 + |\Omega_c|^2 \frac{|D_s|^2 + |\Omega_p|^2\left(|\Omega_s|^2 + |d_4|^2\right)}{|D|^2}\right]^{-1/2}, \tag{3.9}$$

where, $D_s = |\Omega_s|^2 - d_2 d_4$, and $D = d_4|\Omega_p|^2 + d_3|\Omega_s|^2 - d_2 d_3 d_4$. The other probability amplitudes can be written in terms of C_1 as

$$C_2 = -\frac{d_4\Omega_p^*\Omega_c}{D}C_1, \tag{3.10a}$$

$$C_3 = -\frac{D_s\Omega_c}{D}C_1, \tag{3.10b}$$

$$C_4 = \frac{\Omega_p^*\Omega_c\Omega_s}{D}C_1. \tag{3.10c}$$

In order to derive the linear and nonlinear susceptibilities as defined in Eq. (3.8), a Taylor expansion is performed around $|\Omega_p|^2 = |\Omega_s|^2 = 0$, resulting in the following expressions:

$$\chi_p^{(1)} = -\frac{\mathcal{N}|d_{23}|^2}{\hbar}\frac{|\Omega_c|^2}{d_2^*\left(|d_3|^2 + |\Omega_c|^2\right)}, \tag{3.11a}$$

$$\chi_{pp}^{(3)} = -\frac{\mathcal{N}|d_{23}|^2}{\hbar}\frac{|\Omega_c|^2\left(d_2^* d_3^* + d_2 d_3 - |\Omega_c|^2\right)}{d_2^*|d_2|^2\left(|d_3|^2 + |\Omega_c|^2\right)^2}, \tag{3.11b}$$

$$\chi_{ps}^{(3)} = -\frac{\mathcal{N}|d_{23}|^2}{\hbar}\frac{|\Omega_c|^2 d_2 d_4}{d_2^*|d_2|^2|d_4|^2\left(|d_3|^2 + |\Omega_c|^2\right)}. \tag{3.11c}$$

At the two photon resonance condition, *i.e.*, $\Delta_p - \Delta_c$=0, we get

$$\chi_p^{(1)} = -\frac{\mathcal{N}|d_{23}|^2}{\hbar}\frac{i|\Omega_c|^2}{\gamma_2\left(\Delta_c^2 + \gamma_3^2 + |\Omega_c|^2\right)}, \tag{3.12a}$$

$$\chi_{pp}^{(3)} = \frac{\mathcal{N}|d_{23}|^2}{\hbar}\frac{i|\Omega_c|^2\left(2\gamma_2\gamma_3 + |\Omega_c|^2\right)}{\gamma_2^3\left(\Delta_c^2 + \gamma_3^2 + |\Omega_c|^2\right)^2}, \tag{3.12b}$$

$$\chi_{ps}^{(3)} = \frac{\mathcal{N}|d_{23}|^2}{\hbar}\frac{|\Omega_c|^2\left(\Delta_s + i\gamma_4\right)}{\gamma_2^2\left(\Delta_s^2 + \gamma_4^2\right)\left(\Delta_c^2 + \gamma_3^2 + |\Omega_c|^2\right)}. \tag{3.12c}$$

From Eqs. (3.12a)-(3.12c), it is observed that $\chi_p^{(1)}$ and $\chi_{pp}^{(3)}$ are entirely imaginary. The negative sign associated with $\mathrm{Im}[\chi_p^{(1)}]$ indicates linear gain, while $\mathrm{Im}[\chi_{pp}^{(3)}]$ reflects nonlinear absorption. This nonlinear absorption, arising from the self-Kerr effect, increases with the intensification of the probe field intensity. Conversely, $\chi_{ps}^{(3)}$ comprises both real and imaginary components. Notably, only $\mathrm{Re}[\chi_{ps}^{(3)}]$ at two-photon resonance results in significant cross-Kerr nonlinearity. Moreover, $\mathrm{Im}[\chi_{ps}^{(3)}]$ characterizes the nonlinear absorption induced by the cross-Kerr effect, which also escalates with an increase in the intensity of the signal field.

3.2.3 Beam propagation equation with paraxial approximation

The investigation of beam propagation equations plays a pivotal role in examining the influence of absorption, diffraction, dispersion on probe beam propagation. By employing the slowly varying envelope and paraxial wave approximations, the propagation equations governing the probe beam can be written as

(i) *For scalar probe, and control beam:*

$$\frac{\partial \Omega_p}{\partial z} = \frac{i}{2k_p}\nabla_\perp^2 \Omega_p + 2\pi i k_p \chi_{32}\Omega_p, \tag{3.13a}$$

$$\frac{\partial \Omega_c}{\partial z} = \frac{i}{2k_c}\nabla_\perp^2 \Omega_c + 2\pi i k_c \chi_{31}\Omega_c, \tag{3.13b}$$

and (ii) *For vector probe beam:*

$$\frac{\partial \Omega_R}{\partial z} = \frac{i}{2k_R}\nabla_\perp^2 \Omega_R + 2\pi i k_R \chi_{42}\Omega_R, \tag{3.14a}$$

$$\frac{\partial \Omega_L}{\partial z} = \frac{i}{2k_L}\nabla_\perp^2 \Omega_L + 2\pi i k_L \chi_{32}\Omega_L. \tag{3.14b}$$

Note that Eqs. (3.13a), and (3.13b) refer to scalar beams and Eqs. (3.14a), and (3.14b) correspond to VB propagation. The right-hand side of the equations consists of two terms: the first term accounts for diffraction, while the second term denotes the dispersion and absorption of the probe, through its susceptibility. Throughout our work, we consistently operate within the paraxial regime, a framework that is appropriate given that the beam waist is considerably larger than the wavelength of the light used. It is crucial to consider the dynamics of the strong control field, as it is associated with both the ground state and the excited state, thus impacting the propagation of the probe beam. Given that the signal field E_s is a strong plane wave connected with $|2\rangle \leftrightarrow |4\rangle$ transition, its propagation effects are negligible and have been validated through detailed simulation analysis. To numerically analyze Eqs. (3.13a), (3.13b), and Eqs. (3.14a), (3.14b), the split-step Fourier method (SSFM) has been selected for the study.

3.3 Numerical results

3.3.1 Linear and nonlinear susceptibilities

In this section, we delve into the analysis of both linear and nonlinear susceptibilities observed in the probe beam. Figures 3.2 (a) and 3.2(b) effectively illustrate the

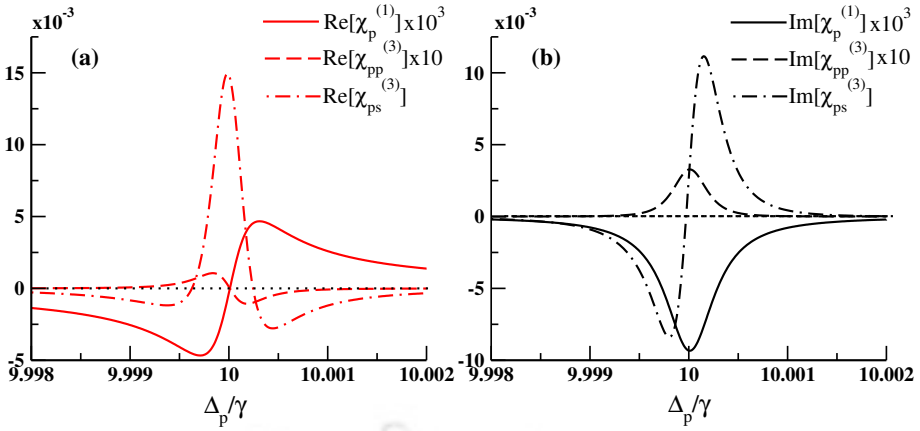

Figure 3.2: Real and imaginary part of both linear and third-order nonlinear χ_{32} are plotted against the probe detuning. (a), (b) correspond to real, and imaginary part of χ_{32} respectively. Parameter used: $\Omega_p = 0.001\gamma, \Omega_c = 0.7\gamma$, $\Omega_s = 0.05\gamma$. $\gamma_2 = 3 \times 10^{-4}\gamma, \gamma_3 = 5 \times 10^2\gamma$, $\gamma_4 = 0.5\gamma$. $\Delta_c = 10\gamma, \Delta_s = 2\gamma$. Normalized frequency $\gamma = 10^6$ s^{-1}. The density of atoms, $\mathcal{N} = 5 \times 10^{11}$cm^{-3}.

behavior of these susceptibilities by showcasing the real and imaginary components of both the linear susceptibility and the third order Kerr nonlinear susceptibility. In Fig. 3.2 (a), we can see that the real part of the linear susceptibility, denoted as Re$[\chi_p^{(1)}]$, along with the real part of the third order susceptibility, Re$[\chi_{pp}^{(3)}]$, both approach zero at the point of two-photon resonance. In contrast, Re$[\chi_{ps}^{(3)}]$ exhibits a significant nonzero value, indicating a notable response under these conditions. This distinct behavior suggests that while the linear susceptibility is minimal at resonance, the cross-Kerr nonlinear response is greatly enhanced. In Fig. 3.2(b), it is observed that Im$[\chi_p^{(1)}]$ exhibits a negative value at the two-photon resonance, which is indicative of linear gain. The strong control field interacts with the ground state $|1\rangle$ and the excited state $|3\rangle$, facilitating a significant population transfer from the initially populated ground state $|1\rangle$ to the excited state $|3\rangle$. This transfer of population leads to gain in the $|1\rangle \rightarrow |3\rangle$ transition. Consequently, the gain in the probe field can be modulated by appropriately selecting the one-photon detuning of the control field. Additionally, the continuous wave (CW) signal field, which is coupled to the $|2\rangle \leftrightarrow |4\rangle$ transition, contributes to the cross-Kerr nonlinearity of the system. It is important to note that at two-photon resonance, both Im$[\chi_{pp}^{(3)}]$ and Im$[\chi_{ps}^{(3)}]$ are positive, indicating the presence of nonlinear absorption in the probe field.

3.3.2 Beam propagation inside medium

In order to achieve the focusing of the probe beam, it is crucial to meticulously select the transverse spatial profile of the control beam. This selection involves ensuring that the intensity at the center of the control beam significantly exceeds that of its outer regions. For this purpose, we have opted for a Gaussian-shaped control beam. This choice is made to effectively support the propagation of both Gaussian and Laguerre-Gaussian (LG) probe beams. The control field is defined as follows:

$$\Omega_c(r, \phi, 0) = \Omega_{c0} \exp\left[-\left(\frac{r^2}{w_0^2}\right)^{l_c}\right]. \tag{3.15}$$

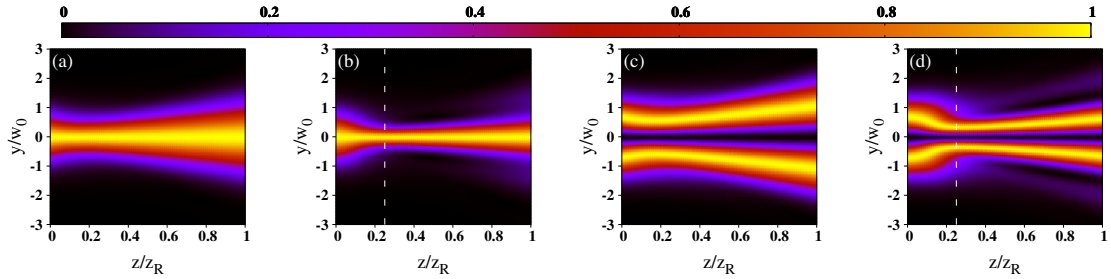

Figure 3.3: Longitudinal intensity profile of (a) Gaussian, and (c) LG beam propagating inside the medium without taking the effect of cross-Kerr nonlinearity. (b), and (d) corresponds to including the effect of cross-Kerr nonlinearity respectively. The value of l_c for the propagation of probe beam is taken as 1. The probe and the control beam have a waist, $w_0 = 50\mu m$ and is maintained consistently. Other parameters are same as Fig. 3.2.

The input amplitude of the control beam is represented by Ω_{c0}, and l_c is a positive integer. The value $l_c \neq 1$ corresponds to a super-Gaussian or flat-top beams. In Figs. 3.3(b) and 3.3(d), we provide a detailed illustration of the behavior of Gaussian and LG probe beams as they propagate through the medium, taking into account the effects of cross-Kerr nonlinearity. For comparative purposes, we have also depicted the beam propagation in the absence of cross-Kerr nonlinearity, as illustrated in Figs. 3.3(a) and 3.3(c). In Figs. 3.3(a) and 3.3(c), it is evident that the probe beams undergo significant diffraction as they propagate through the medium. Initially, the probe beam converges towards the center due to rapid energy transfer from the control beam, resulting in a gain-narrowed region. However, subsequent to this process, the medium is unable to counterbalance the diffraction, as both $\mathrm{Re}[\chi_p^{(1)}]$ and $\mathrm{Re}[\chi_{pp}^{(3)}]$ are zero as depicted in Fig. 3.2(a). In contrast, an examination of Fig. 3.2(a) reveals that $\mathrm{Re}[\chi_{ps}^{(3)}]$ displays a significant cross-Kerr nonlinearity at resonance. The introduction of a three-photon off-resonance condition, specifically $\Delta_s \neq 0$, is essential for attaining a marked cross-Kerr effect. This noteworthy nonlinearity serves to mitigate the diffraction, thereby facilitating the focusing of the probe beams, as illustrated in Figs. 3.3(b) and 3.3(d). However, as the beam converges, diffraction gradually increases due to the positive value of $\mathrm{Im}[\chi_{pp}^{(3)}]$, which has a defocusing effect. Consequently, the contrasting effects of the presence and absence of cross-Kerr interactions are prominently emphasized, highlighting their essential significance in beam manipulation within the medium.

3.4 Comparative study with probe VB

Till now, we have examined the model presented in Fig. 3.1(a), in which the scalar beam is coupled to the transition between states $|2\rangle$ and $|3\rangle$. An alternative perspective is now considered, wherein a VB serves as a weak probe beam, as illustrated in Fig. 3.1(b). The two orthogonal components of the VB are associated with the transitions $|2\rangle \leftrightarrow |3\rangle$ and $|2\rangle \leftrightarrow |4\rangle$, corresponding to left and right circular polarizations, respectively. Unlike scalar beams, VBs exhibit an inhomogeneous polarization distribution across the transverse plane. This polarization distribution can be classified into two categories. A cylindrical vector (CV) beam is characterized by radial,

azimuthal, and spiral profiles with respect to the axial symmetry of the beam. Conversely, a full Poincaré (FP) beam displays a transverse polarization distribution that varies in both azimuthal and radial directions, resulting in configurations such as lemon, star, and web. The change in the ellipticity of the VB beam can be described using Eqs.(1.127), and (1.129) as

$$\Delta\zeta(z) = \frac{1}{2}\left[\sin^{-1}\left\{\frac{1-a\tan^2\alpha}{1+a\tan^2\alpha}\right\} - \sin^{-1}\left\{\frac{1-b\tan^2\alpha}{1+b\tan^2\alpha}\right\}\right], \tag{3.16}$$

where

$$a = \exp\left[-\frac{2r^2}{w_0^2}\left(\frac{n_R^2 z_R^2}{z^2+n_R^2 z_R^2} - \frac{n_L^2 z_R^2}{z^2+n_L^2 z_R^2}\right)\right]\left\{\frac{r\sqrt{2}}{w_0\sqrt{1+z^2/n_R^2 z_R^2}}\right\}^{2|l_R|} \times \left\{\frac{r\sqrt{2}}{w_0\sqrt{1+z^2/n_L^2 z_R^2}}\right\}^{-2|l_L|}, \tag{3.17}$$

and

$$b = \left(\frac{r\sqrt{2}}{w_0}\right)^{2(|l_R|-|l_L|)}. \tag{3.18}$$

3.4.1 Suceptibilities of the probe VB

The VB constitutes a superposition of two orthogonal components, leading to distinct susceptibilities for the probe VB. These susceptibilities for each component can be defined as follows:

$$\chi_{32} \equiv \chi_L = \frac{\mathcal{N}|d_{23}|^2}{\hbar}\left(\frac{C_3 C_2^*}{\Omega_L}\right) \simeq \chi_L^{(1)} + \chi_{LL}^{(3)}|\Omega_L|^2 + \chi_{LR}^{(3)}|\Omega_R|^2, \tag{3.19a}$$

$$\chi_{42} \equiv \chi_R = \frac{\mathcal{N}|d_{24}|^2}{\hbar}\left(\frac{C_4 C_2^*}{\Omega_R}\right) \simeq \chi_R^{(1)} + \chi_{RR}^{(3)}|\Omega_R|^2 + \chi_{RL}^{(3)}|\Omega_L|^2. \tag{3.19b}$$

The linear probe susceptibility is denoted as $\chi_{L,R}^{(1)}$, while the third order self and cross Kerr susceptibilities are represented as $\chi_{LL,RR}^{(3)}$ and $\chi_{LR,RL}^{(3)}$ respectively. As before we perform a Taylor expansion around $|\Omega_L|^2 = |\Omega_R|^2 = 0$, resulting in the following expressions:

$$\chi_L^{(1)} = -\frac{\mathcal{N}|d_{23}|^2}{\hbar}\frac{|\Omega_c|^2}{d_2^*\left(|d_3|^2+|\Omega_c|^2\right)}, \tag{3.20a}$$

$$\chi_{LL}^{(3)} = -\frac{\mathcal{N}|d_{23}|^2}{\hbar}\frac{|\Omega_c|^2\left(d_2^* d_3^* + d_2 d_3 - |\Omega_c|^2\right)}{d_2^*|d_2|^2\left(|d_3|^2+|\Omega_c|^2\right)^2}, \tag{3.20b}$$

$$\chi_{LR}^{(3)} = -\frac{\mathcal{N}|d_{23}|^2}{\hbar}\frac{|\Omega_c|^2 d_2 d_4'}{d_2^*|d_2|^2|d_4'|^2\left(|d_3|^2+|\Omega_c|^2\right)}, \tag{3.20c}$$

$$\chi_R^{(1)} = \chi_{RR}^{(3)} = 0, \tag{3.20d}$$

$$\chi_{RL}^{(3)} = -\frac{\mathcal{N}|d_{24}|^2}{\hbar}\frac{|\Omega_c|^2}{|d_2|^2 d_4'\left(|d_3|^2+|\Omega_c|^2\right)}. \tag{3.20e}$$

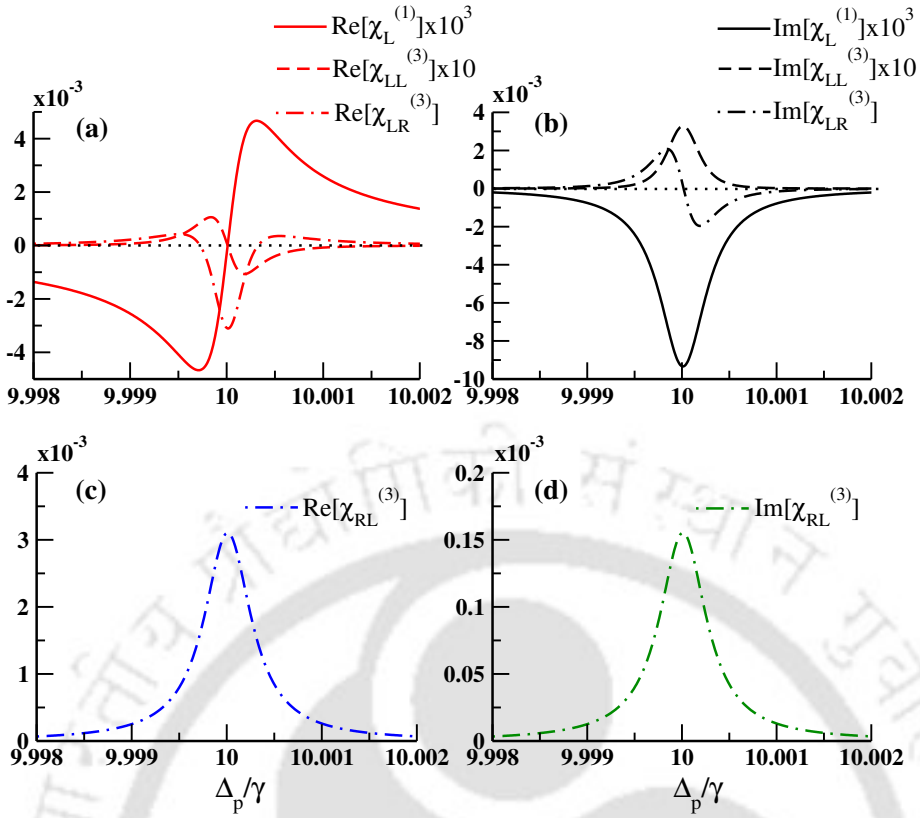

Figure 3.4: Real and imaginary part of both linear and third-order nonlinear χ_L and χ_R are plotted against the corresponding transition detunings. (a), (b) correspond to real, and imaginary part of χ_L plotted against Δ_p/γ respectively. Similarly (c), (d) correspond to real, and imaginary part of χ_R plotted against Δ_p/γ respectively. Parameter used: $\Omega_{R,L} = 0.001\gamma, \Omega_c = 0.7\gamma$. Other parameters are same as Fig. 3.2

At the two photon resonance condition, we get

$$\chi_L^{(1)} = -\frac{\mathcal{N}|d_{23}|^2}{\hbar} \frac{i|\Omega_c|^2}{\gamma_2\left(\Delta_c^2 + \gamma_3^2 + |\Omega_c|^2\right)}, \tag{3.21a}$$

$$\chi_{LL}^{(3)} = \frac{\mathcal{N}|d_{23}|^2}{\hbar} \frac{i|\Omega_c|^2\left(2\gamma_2\gamma_3 + |\Omega_c|^2\right)}{\gamma_2^3\left(\Delta_c^2 + \gamma_3^2 + |\Omega_c|^2\right)^2}, \tag{3.21b}$$

$$\chi_{LR}^{(3)} = \frac{\mathcal{N}|d_{23}|^2}{\hbar} \frac{|\Omega_c|^2\left(-\Delta_p + i\gamma_4\right)}{\gamma_2^2\left(\Delta_p^2 + \gamma_4^2\right)\left(\Delta_c^2 + \gamma_3^2 + |\Omega_c|^2\right)}, \tag{3.21c}$$

$$\chi_R^{(1)} = \chi_{RR}^{(3)} = 0, \tag{3.21d}$$

$$\chi_{RL}^{(3)} = \frac{\mathcal{N}|d_{23}|^2}{\hbar} \frac{|\Omega_c|^2\left(\Delta_p + i\gamma_4\right)}{\gamma_2^2\left(\Delta_p^2 + \gamma_4^2\right)\left(\Delta_c^2 + \gamma_3^2 + |\Omega_c|^2\right)}, \tag{3.21e}$$

where, $d_4' = (\Delta_c - 2\Delta_p + i\gamma_4)$. In the preceding equations, it is interesting to note that the right component of the probe VB, connected to the transition $|2\rangle \leftrightarrow |4\rangle$, exhibits only cross-Kerr susceptibility.

From Eqs. (3.21a)-(3.21e), it can be observed that $\chi_L^{(1)}$ and $\chi_{LL}^{(3)}$ are entirely imaginary quantities. The negative sign associated with $\mathrm{Im}[\chi_L^{(1)}]$ indicates a linear gain, while $\mathrm{Im}[\chi_{LL}^{(3)}]$ reflects nonlinear absorption phenomena. In contrast, $\chi_{LR}^{(3)}$ exhibits both real and imaginary components. It is determined that the left circular component of the probe beam contributes to both linear gain and nonlinear absorption,

with nonlinear absorption increasing in response to higher probe beam intensities. For the right circular component, both the linear and self-Kerr terms are found to be zero. This phenomenon arises because the coherence in the transition $|4\rangle \leftrightarrow |2\rangle$ develops solely in the presence of the left circular component. However, there is a contribution from the term $\chi^{(3)}_{RL}$, which results in absorption due to cross-Kerr nonlinearity. In Figs. 3.4(a)-(d) we plot the linear and nonlinear responses of both the components of the probe beam which illustrate the above facts. It is noteworthy that the two components of the VB are not separable, leading to an enhancement of nonlinear interactions as the probe beam intensity increases.

3.4.2 Gain induced narrowing

In this section we demostrate the VB propagation inside the atomic medium. In Figs. 3.5(a)-(d), we illustrate the propagation of VBs in both free space and within the Raman gain medium. During the initial narrowing phase, the control beam facilitates energy transfer to the probe beam. The energy transfer is more pronounced in regions with higher control beam intensity, resulting in a gain-narrowed probe profile that achieves a minimum spot radius. In the illustrations labeled Fig. 3.5(a) and Fig. 3.5(c), the longitudinal profile of lemon and radial VB propagation in free space is depicted. Conversely, Fig. 3.5(b) and Fig. 3.5(d) characterize the propagation of lemon and radial VB inside the medium. Although the consequence of cross-Kerr nonlinearity is not evident here, the linear gain of the system supports the narrowing of the VBs. This phenomenon is known as gain-induced narrowing. Refractive focusing is attributed to the real part, while gain narrowing is linked to the imaginary part of the susceptibility of the probe beam. The control beam has a significant influence on the propagation of the probe beam. In Fig. 3.6 we have plotted the profile of the control beam that affects the propagation of the lemon VB at various distances. The beam width at the full width at half maximum (FWHM) for propagation distances of $z = 0$, $0.25z_R$, $0.5z_R$, and z_R is measured to be $1.16w_0$, $1.22w_0$, $1.32w_0$, and $1.66w_0$, respectively. In the inset of Fig. 3.6, we present the normalized intensity of the control beam at the specified distances. It is evident that the gain-assisted narrowing of the probe beam results from the transfer of energy

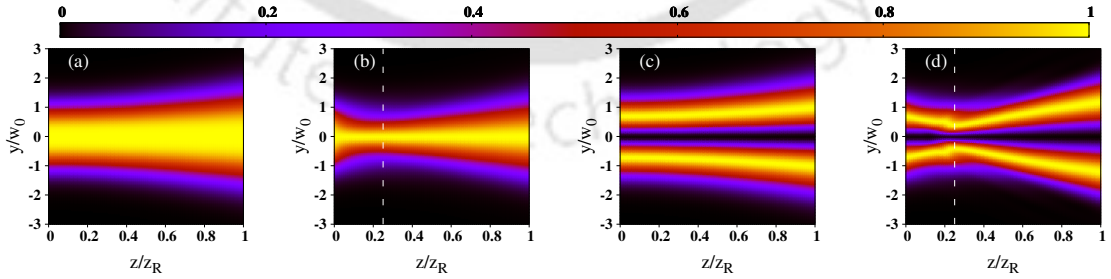

Figure 3.5: Longitudinal intensity profile of (a) lemon ($l_L = 0, l_R = 1, \alpha = \pi/4, \theta = 0$), (c) radial ($l_L = -1, l_R = 1, \alpha = \pi/8, \theta = 0$) VB propagating in free space, and inside the gain medium (b), and (d) respectively. The value of l_c for the propagation of lemon and radial VB is taken as 1, and 4 respectively. The probe and the control beam have a waist, $w_0 = 50\mu m$ and is maintained consistently. White dashed vertical line denotes the minimum spot size achieved due to gain-induced narrowing. Other parameters are same as Fig. 3.4.

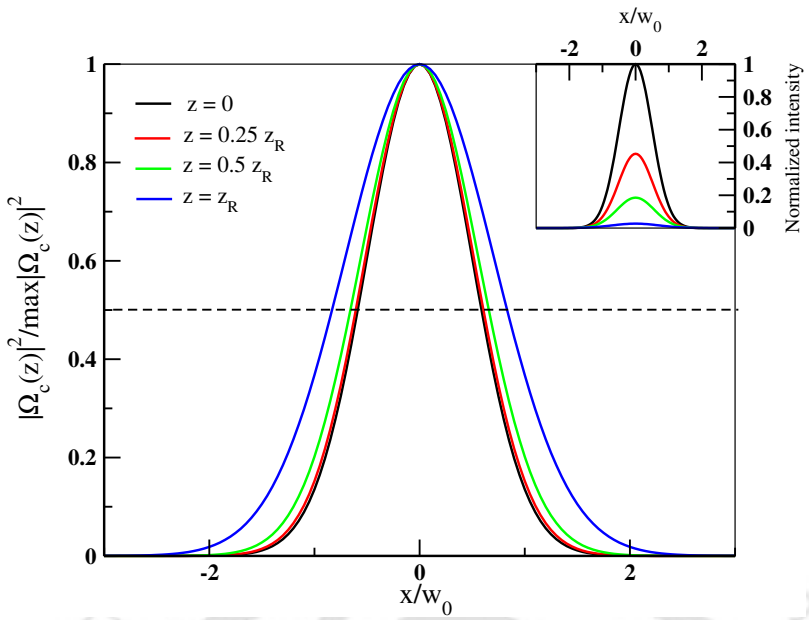

Figure 3.6: The beam waist of the control field is measured at different propagation distances. The variation of its intensity is presented in the inset. The control beam have a waist, $w_0 = 50\mu m$, $l_c = 1$ and other parameters are same as Fig. 3.4.

from the control beam to the probe beam. Consequently, as the energy transfer diminishes, the probe beam begins to diverge. These observations highlight the necessity of carefully controlling the intensities of both the probe and control beams in order to achieve a moderate gain regime, which in turn facilitates the narrowing of VBs. The discussed gain-induced narrowing phenomenon is expected to be a pervasive occurrence, applicable to any medium supporting nonlinear focusing and stimulated Raman scattering.

Further, we examine the state of polarization (SOP) of the probe VBs as it poses inhomogeneous polarization distribution unlike scalar beam. As depicted in Fig. 3.7(a) and Fig. 3.7(b), we display the SOP at input $z = 0$ for the lemon and radial VBs, respectively. Subsequently, after the beam narrowing, the SOP of the lemon and radial VBs at $z = 0.25z_R$ is illustrated by Fig. 3.7(c) and Fig. 3.7(d) correspondingly. Our findings indicate that the SOP of the lemon VB at $z = 0.25z_R$ has undergone a clockwise rotation by an angle of $\pi/4$ with a variation in ellipticity. The disparity between the refractive indices n_R and n_L is central to this phenomenon. In contrast, the radial VB exhibits an ellipticity mostly unchanged. Moreover, we observe that the FWHM of the lemon VB at the input is $1.84w_0$, which subsequently becomes $0.98w_0$ upon narrowing at z = $0.25z_R$. Likewise, at the input, the FWHM of the central dark region of the radial VB is $0.68w_0$, reduced to $0.36w_0$ upon narrowing. Furthermore, as the VB propagates and diverges within the medium, its SOP gradually becomes more homogeneous across the transverse plane, resembling the behavior of a scalar beam. This phenomenon becomes evident when there exists an insufficient difference between the refractive indexes n_R and n_L.

Finally, we present a concise overview of the optical properties associated with two configurations employing scalar and vector probe beams. In Table 3.1, we provide the values of the real and imaginary components of linear and nonlinear susceptibilities under two-photon resonance conditions, along with details regarding the nature of focusing or narrowing, and the reduction in spot size at the minimum beam waist

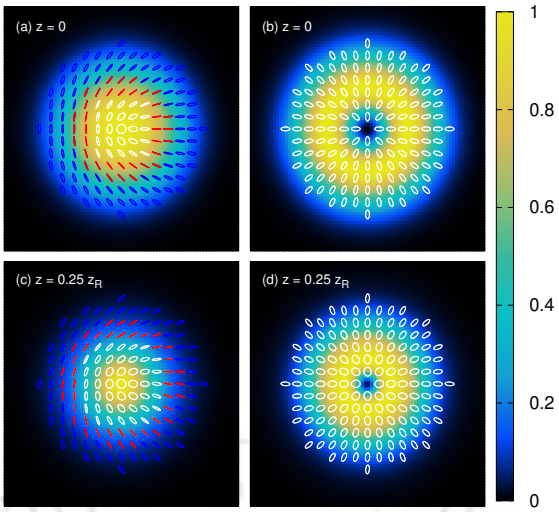

Figure 3.7: Transverse intensity and polarization distribution at the $z = 0$ for (a) lemon, (b) radial and at minimum beam radius $z = 0.25z_R$ for (c) lemon, (d) radial VB respectively. The intensity is normalized by its maximum intensity for each VB. The colors white, red, and blue correspond to left circular, linear, and right circular polarizations, respectively. Parameters remain same as Fig. 3.5.

for both scenarios. It is observed that the scalar probe beam exhibits cross-Kerr-induced focusing due to the significant magnitude of the real part of its cross-Kerr susceptibility. Conversely, in the case of the vector probe beam, the real part of the cross-Kerr susceptibility for the left and right circular components is equivalent in magnitude but opposite in sign. Notably, the nonlinear absorption for the vector probe beam is considerably lower than that of the scalar probe beam. However, the linear gain remains consistent for both configurations. Consequently, gain-assisted narrowing is discerned in the VB scenario.

Table 3.1: Comparison of linear and nonlinear susceptibilities at two photon resonance, type of beam focusing or narrowing and spot size reduction between the scalar (Fig. 3.1(a)), and vector (Fig. 3.1(b)) probe beam in ARG scheme.

	Scalar probe		Vector probe
$\mathrm{Re}[\chi_p^{(1)}]$	0	$\mathrm{Re}[\chi_L^{(1)}]$	0
$\mathrm{Re}[\chi_{pp}^{(3)}]$	0	$\mathrm{Re}[\chi_{LL}^{(3)}]$	0
$\mathrm{Re}[\chi_{ps}^{(3)}]$	14.6×10^{-3}	$\mathrm{Re}[\chi_{LR}^{(3)}]$	-3.11×10^{-3}
		$\mathrm{Re}[\chi_{RL}^{(3)}]$	3.11×10^{-3}
$\mathrm{Im}[\chi_p^{(1)}]$	-9.34×10^{-6}	$\mathrm{Im}[\chi_L^{(1)}]$	-9.34×10^{-6}
$\mathrm{Im}[\chi_{pp}^{(3)}]$	0.328×10^{-3}	$\mathrm{Im}[\chi_{LL}^{(3)}]$	0.328×10^{-3}
$\mathrm{Im}[\chi_{ps}^{(3)}]$	3.66×10^{-3}	$\mathrm{Im}[\chi_{LR}^{(3)}]$	0.16×10^{-3}
		$\mathrm{Im}[\chi_{RL}^{(3)}]$	0.16×10^{-3}
Focusing	Cross-kerr induced	Narrowing	Gain-induced
Spot size reduction	56% (for gaussian) 53% (for LG)	Spot size reduction	46.7% (for Lemon) 47% (for radial)

3.5 Discussion

Unlike the four-level EIT-based absorptive scheme, we adopt the ARG scheme to investigate the focusing behavior of the beam [138, 152]. As shown in the Appendix, the $\mathrm{Re}[\chi_{ps}^{(3)}]$ is nearly eighteen times larger in the ARG system compared to the EIT case. This significantly enhanced cross-Kerr nonlinearity enables stronger modulation of the medium's refractive index, which in turn facilitates efficient focusing of the beam toward the propagation axis. In addition, the linear gain in the ARG configuration is higher than the nonlinear gain typically obtained in the EIT scheme, making ARG more suitable for controlled beam manipulation. These features suggest potential applications in areas such as Tip-Enhanced Raman Spectroscopy (TERS), where VBs improve the interaction between light and the plasmonic tip by generating a strong longitudinal electric field component under tight focusing [173, 174]. Furthermore, the system offers prospects for compact, mode-selective optical amplifiers. By coupling specific scalar or VB profiles with a suitably tuned ARG medium, selective amplification based on spatial mode structure can be achieved, which is particularly useful in integrated photonic circuits requiring precise mode control [175]. From an experimental perspective, such a system could be implemented using four-level media based on alkali atoms (e.g., rubidium or cesium) or rare-earth ions in crystal hosts. Raman transitions can be driven by pump and control lasers, while scalar and VBs may be generated using spatial light modulators, q-plates, or polarization-conversion optics [176, 177]. The output can then be characterized using heterodyne detection, OAM analysis, and high-resolution CCD imaging. Nevertheless, practical realization requires careful control of experimental conditions, as maintaining coherence in the ARG scheme, especially for spatially structured VBs, demands precise beam alignment, stable detuning, temperature control, and minimal atomic dephasing.

3.6 Conclusion

In conclusion, this study conducts a theoretical examination of the focusing characteristics of scalar and VBs within the framework of a four-level active Raman gain system. In both configurations utilizing scalar and vector probe beams, the ground state is coupled with a strong control field characterized by high detuning, which is indicative of a gain system. The CW signal field, with a nonzero detuning, serves to enhance the cross-Kerr nonlinearity of the system. With a precise selection of input field intensities and the spatial profile of the control beam, both scalar and vector probe beams exhibit a focusing or narrowing phenomena. However, it is observed that the medium's susceptibility varies distinctly between the scalar and vector probe beams. While the combination of linear and self-Kerr nonlinearity can focus the scalar probe beam to a certain degree, the impact of cross-Kerr nonlinearity allows for focusing of the beam into a significantly smaller spot. Conversely, the vector probe beam showcases gain-assisted narrowing as a result of energy transfer from the control beam. Furthermore, an analysis of the SOP of the VB is conducted at the minimum beam waist. The focusing or the narrowing effects observed in both scalar and VBs lead to a reduction in spot size, which has the potential to substantially enhance optical resolution.

Chapter 4

Super-resolution in quantum dots via rapid adiabatic passage

4.1 Introduction

The previous chapter showed that cross-Kerr nonlinearity and gain-assisted narrowing can compress optical beams into smaller focal spots, offering a path toward enhanced resolution. Such reductions in spot size are particularly valuable for imaging applications where finer spatial detail is required. In light of these implications, this chapter focuses on rapid adiabatic–passage–based super-resolution in a QD system. Conventional optics fail to resolve the spot size of an image beyond a value comparable to the probing light wavelength. Ernst Abbe first realized that the primary constraint of resolution imaging comes from diffraction [62]. Later it was mathematically formulated using Fourier transform theory [178]. Defeating the diffraction barrier has been the key to achieving high-resolution imaging. The use of super-resolution microscopy techniques can overcome the diffraction limit. In STED microscopy [63, 179], excitation and depletion light beams with Gaussian and doughnut intensity profiles are used to illuminate the sample simultaneously. The excitation beam excites the fluorescent molecules to the bright state, and the depletion beam turns them back to the dark state by stimulated emission. As a result, the central zero intensity area of the doughnut beam fluorophores stays in a bright state and produces a tighter focused image. The transition probability between bright and dark states depends on the intensity of the laser beam. STED microscopy has opened up a new platform for imaging at the nanoscale in material science and medical biology [67, 180]. In particular, STED involves fluorescence depletion, which is an incoherent process. There are also other contemporary techniques [181, 73] which give an incoherent response to the laser.

RAP based imaging can further improve the shortfall of STED microscopy. The RAP exploits the coherent response of the laser [182], which indicates coherent manipulation of quantum states to achieve efficient population transfer. It uses a time-advance strong RAP positive chirping pulse that transfers the population from the ground to the excited state. A second time-delayed RAP pulse with negative chirping can de-excite the population from the excited state to the ground state. Hence, the intensity-dependent RAP in a two-level system acts like a nearly ideal 'on' and 'off' switch, which qualifies the critical criterion of super-resolution microscopy. With the advent of short, intense pulse and pulse-shaping technology, selective population

TH-3976_186121017

transfer has become efficient [183]. Population transfer through a chirp pulse is much more effective than the pulse without chirping [184, 185]. Moreover, a frequency-swept pulse-induced excitation is immune from Rabi oscillation [186, 187]. Under the adiabatic condition, a strong Rabi frequency can transfer the population at the desired level without decay and decoherence inducing losses [188].

Semiconductor QDs allow precise control over their size, shape, and composition, enabling more tailored RAP implementation than atomic systems [189]. The above mentioned scheme explores the effect of coherent control under decoherence in solid-state systems. Experiments on optically driven InGaAs/GaAs QDs found the intensity damping of Rabi rotation (RR) due to longitudinal acoustic (LA) phonons [190, 191]. These self-assembled QDs interact with the phonons, limiting the excitonic transition's coherence [192, 193, 194, 167, 168, 169, 170]. Various theoretical approaches have been proposed for investigating phonon interaction's role in the excited state's coherent population distribution. This includes the ME using perturbative expansion of the exciton phonon coupling in Markovian [190, 191, 167, 195] and non-Markovian limit [192, 196, 197], numerical techniques with path integral method [194], and correlation expansion [193, 198, 199].

In this work, we have studied the RAP-based super-resolution microscopy technique in a semiconductor quantum dot. The QDs are made of InGaAs and embedded in GaAs wetting layers. Due to their strong carrier confinement, energy levels become discrete like atoms. Here, we consider the QD an effective two-level system by considering large biexciton binding energy. Similar to the STED technique, two oppositely chirped structured lights with super-Gaussian and doughnut intensity are coupled to the two QD levels. The system also incorporates phonon interaction with the QD due to lattice vibration associated with the environmental temperature. Therefore, investigating phonon-mediated dephasing is mandatory for image formation. To illustrate the effect of temperature on imaging, we study the variational ME. We also consider a truncated spatial envelope of the Bessel-modulated SG and Bessel-modulated LG beam to improve the spot size resolution by stopping residual ground state population excitation in the form of an additional unwanted ring. The system shows an excellent super-resolved image for the QD, which is beyond the capability of the conventional imaging system. Therefore, this scheme's tunable optical properties of QD have potential applications in sensors, drug delivery, biomedical imaging [200, 201], quantum communication, and quantum information [202].

The chapter is organized as follows. Section 4.1 contains a brief introduction to super-resolution and its application in the QD medium. Section 4.2 presents the level system and theoretical formalism considering the phonon contribution using the variational ME. In Section 4.3, we discuss the numerical results regarding super-resolution image formation with various controlling parameters such as light intensity, and temperature by removing the unwanted low-intensity ring around the central bright spot image. Finally, in section 4.4, we give a conclusion of the work.

4.2 Theoretical formulation

Controllable population transfer at the excited state is the essence behind super-resolution imaging [61]. A variety of methods, such as stimulated Raman adiabatic passage (STIRAP) [203], super-adiabatic STIRAP (saSTIRAP) [204], and RAP [184], have been used to transfer the population to the desired state. The popu-

lation inversion is beyond reach for a two-level system due to the thermodynamic limit. RAP can overcome this limitation [50]. The two-level system can achieve an efficient and robust time-dependent population inversion under the RAP. We study a detailed theoretical explanation for forming super-resolution imaging beyond the diffraction limit based on variational ME. The charge confinement of electron-hole pairs leads to semiconductor QD manifests an atom-like discrete energy level structure. A left-handed circularly polarized light that drives the excited (exciton) state $|1\rangle$ and ground state $|2\rangle$ with energy separation $\hbar\omega_{QD}$ produces a two-level configuration as shown in Fig. 4.1. The incident light consists of two spatiotemporal beams of opposite chirping interacting with the two-level quantum dot by the induced dipole moment.We have adopted a semi-classical treatment of light-matter interaction where the field is classical, and the energy levels of QD are discrete. The excitation and de-excitation of two beams which couple the states $|1\rangle$ and $|2\rangle$ are respectively given as

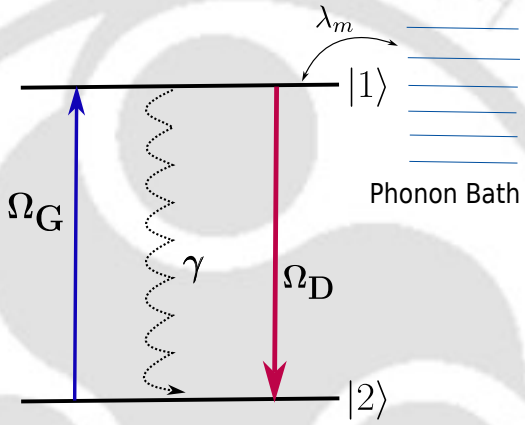

Figure 4.1: Schematic diagram of two-level quantum dot interacting with phonon bath. Two spatiotemporal beams interact with the system of Rabi frequencies Ω_G and Ω_D. The spontaneous emission decay rate from $|1\rangle$ to $|2\rangle$ is given by γ. The two beams interact resonantly with both the levels.

$$\vec{E}_G(r,t) = \hat{\sigma}_- \mathcal{E}_G(r) e^{-\frac{t^2}{2\tau^2} - i\omega_G t - i\alpha_G \frac{t^2}{2}} + c.c., \tag{4.1a}$$

$$\vec{E}_D(r,t) = \hat{\sigma}_- \mathcal{E}_D(r) e^{-\frac{t^2}{2\tau^2} - i\omega_D t - i\alpha_D \frac{t^2}{2}} + c.c., \tag{4.1b}$$

where $\hat{\sigma}_-$ is the left circular polarization unit vector, τ is chirped pulse width, ω_G and ω_D are the corresponding carrier frequencies, α_G and α_D are the linear temporal chirp of the first and second pulse respectively. Specifically, the linear temporal chirp denotes the sweep rate of the laser from a negative detuning to a positive detuning or vice-versa. The spatial profiles of the two beams $E_G(r)$ and $E_D(r)$ are taken to be a SG and LG_0^1, respectively, expressed as

$$\mathcal{E}_G(r) = \mathcal{E}_G^0 e^{-\left(\frac{r}{\sqrt{2}w_G}\right)^{2n}}, \tag{4.2a}$$

$$\mathcal{E}_D(r) = \mathcal{E}_D^0 \left(\frac{r}{w_D}\right) e^{-\frac{r^2}{2w_D^2} + im\phi}, \tag{4.2b}$$

where $\mathcal{E}_G^0$ and $\mathcal{E}_D^0$ are the amplitude, n is an integer which denotes the flatness of the Gaussian top. The value $n > 1$ resembles the super-Gaussian or flat top beams and we have taken $n = 2$. The beam waist of each beam is denoted by w_G and w_D, the orbital angular momentum index $l = 1$, and ϕ is the phase difference between the two beams, which we have taken $\pi/2$. The SG beam transfers the population from the ground state to the excited state, and the LG beam depletes the excited state population to the ground state.

4.2.1 System Hamiltonian

The total Hamiltonian of the system in the presence of the two beams under electric dipole approximation can be written as

$$\boldsymbol{H} = \hbar\omega_{QD}|1\rangle\langle 1| - \vec{d}_{12}.\left(\vec{E}_G(r,t) + \vec{E}_D(r,t)\right)|1\rangle\langle 2| + H.c., \tag{4.3}$$

where $\vec{d}_{12} = \langle 1|\hat{d}|2\rangle$ is the matrix elements of the induced dipole moment operator $\hat{d}$ for the transition $|1\rangle \leftrightarrow |2\rangle$. We make a unitary transformation as

$$\mathbf{U} = e^{-i\nu(t)t|1\rangle\langle 1|}, \tag{4.4}$$

where $\nu(t) = \omega_D + \alpha_D t/2$. Note that the time-dependent frequency signifies the characteristics of the chirp pulse. Now, the effective Hamiltonian in the interaction picture is given by

$$\mathcal{H}_{eff} = \mathbf{U}^\dagger \boldsymbol{H}\mathbf{U} - i\hbar\mathbf{U}^\dagger\frac{\partial\mathbf{U}}{\partial t}. \tag{4.5}$$

Under RWA the above Hamiltonian gives

$$\mathcal{H}_{eff} = -\hbar\Delta(t)|1\rangle\langle 1| + \frac{\hbar}{2}(\Omega_G(r,t)e^{i\delta(t)t} + \Omega_D(r,t))|1\rangle\langle 2| + H.c.,$$

where the detunings are defined as

$$\Delta(t) = (\omega_D + \alpha_D t) - \omega_{QD}, \tag{4.6a}$$

$$\delta(t) = (\omega_D - \omega_G) - \frac{t}{2}(\alpha_G - \alpha_D). \tag{4.6b}$$

Both the beams interact resonantly with two-level system *i.e.*, $\omega_D = \omega_G = \omega_{QD}$. The spatiotemporal Rabi frequencies of respective beams are defined as, $\Omega_G(r,t) = \vec{\mathbf{d}}_{12}.\hat{\sigma}_-\mathcal{E}_G e^{-t^2/2\tau^2}/\hbar$, and $\Omega_D^0 = \vec{\mathbf{d}}_{12}.\hat{\sigma}_-\mathcal{E}_D e^{-t^2/2\tau^2}/\hbar$.

The system under consideration is significantly different from the well-studied single-atom emitters due to the solid-state nature of the semiconductor QD emitters. The medium consists of a few InGaAs QDs grown on top of GaAs host material using molecular beam epitaxy. Therefore, the host lattice vibration modifies the QD dynamics depending on the environment temperature. In the literature, the quantized form of the vibrational energy in a periodic structure refers to a phonon. Many theoretical and experimental studies confirm the longitudinal acoustic (LA) phonon coupling with QDs via deformation potential. Therefore, various new quantum phenomena were discovered, like the appearance of new features in Mollow triplets [205, 206], emission line broadening [193, 207, 208], and limiting degree of indistinguishability of photons [209, 210]. On the other hand, the QD-phonon interaction

model explains several quantum features, such as RR [195], RAP [211, 212, 213], and phonon-assisted state preparation [214, 215]. It is pertinent to include the effect of phonon, interacting with the two-level QD configuration. The system is coupled to an acoustic phonon bath represented by as a collection of harmonic oscillators with frequency $\omega_m = c_s k$ where, c_s is the velocity of sound and k is the wavevector, creation and annihilation operator of the m^{th} mode are $b_m^\dagger$ and b_m respectively. The coupling constant for exciton phonon mode is λ_m. The effective Hamiltonian under the phonon consideration in the interaction picture can be written as [49],

$$\boldsymbol{H}'(t) = -\hbar\Delta|1\rangle\langle 1| + \frac{\hbar}{2}(\Omega(t)|1\rangle\langle 2| + \Omega(t)^*|2\rangle\langle 1|) + \sum_m \hbar\omega_m b_m^\dagger b_m + \sum_m \hbar\lambda_m(b_m + b_m^\dagger)|1\rangle\langle 1|, \tag{4.7}$$

where Δ is given by Eq. (4.6a) and the complex Rabi frequency $\Omega(t) = \Omega_D + \Omega_G e^{i\delta t}$. We make a variational transformation

$$H_V = e^V H' e^{-V}, \text{ where } V = |1\rangle\langle 1| \sum_m \frac{f_m}{\omega_m}(b_m^\dagger - b_m). \tag{4.8}$$

In the above equation the set of f_m are the variational parameters. This transformed Hamiltonian gives the freedom to split the total Hamiltonian into system, bath, and interaction parts which are given as [49, 216],

$$H_{SV} = -\hbar\Delta_v|1\rangle\langle 1| + \langle B\rangle X_x(t) \tag{4.9a}$$

$$H_B = \sum_m \hbar\omega_m b_m^\dagger b_m \tag{4.9b}$$

$$H_{IV} = X_x(t)\zeta_x + X_y(t)\zeta_y + |1\rangle\langle 1|\zeta_z, \tag{4.9c}$$

where $\Delta_v = \Delta + R$, and the shift $R = \sum_m f_m(f_m - 2\lambda_m)/\omega_m$ depends on the variational parameters. The phonon-modified system operators can be defined as follows:

$$X_x(t) = \frac{\hbar}{2}(\Omega|1\rangle\langle 2| + \Omega^*|2\rangle\langle 1|)$$

$$X_y(t) = \frac{i\hbar}{2}(\Omega|1\rangle\langle 2| - \Omega^*|2\rangle\langle 1|)$$

The fluctuation operators induced by the bath are $\zeta_x = (B_+ + B_- + 2\langle B\rangle)/2$, $\zeta_y = (B_+ - B_-)/2i$, and $\zeta_z = \sum_m(\lambda_m - f_m)(b_m^\dagger + b_m)$. The phonon displacement operator can be expressed as

$$B_\pm = \exp\left[\pm\sum\frac{f_m}{\omega_m}(b_m^\dagger - b_m)\right]. \tag{4.10}$$

The displacement operators contain summation over all the phonon modes. We need to find the variational parameter f_k, and in order to do so we use the free energy minimization [216] and get the self-consistent form of the free parameter as

$$f_m = \frac{\lambda_m\left[1 - \frac{\Delta_v}{\eta_v}\tanh(\hbar\beta\eta_v/2)\right]}{1 - \frac{\Delta_v}{\eta_v}\tanh(\hbar\beta\eta_v/2)\left[1 - \frac{\Omega_v^2}{2\Delta_v\omega_m}\coth(\hbar\beta\omega_m/2)\right]}, \tag{4.11}$$

where the inverse temperature $\beta = 1/k_B T$, $\Omega_v = \langle B\rangle|\Omega|$, and $\eta_v = \sqrt{\Omega_v^2 + \Delta_v^2}$. We note from Eq. (4.10) that the bath operators are now function of the variational parameters. We can average it out for a particular temperature T as, $\langle B_+\rangle = \langle B_-\rangle \equiv \langle B\rangle$. The expectation value $\langle B\rangle$ and the shift R is given by

$$\langle B\rangle = \exp\left[-\frac{1}{2}\int_0^\infty \frac{J(\omega)F(\omega)^2}{\omega^2}\coth\left(\frac{\hbar\beta\omega}{2}\right)d\omega\right], \tag{4.12a}$$

$$R = \int_0^\infty \frac{J(\omega)F(\omega)}{\omega}\left[F(\omega) - 2\right]d\omega, \tag{4.12b}$$

where $F(\omega_m) = f_m/\lambda_m$, and for the deformation potential coupling of the exciton-phonon we can take the super-Ohmic spectral density $J(\omega) = \alpha_p\omega^3\exp\left[-\omega^2/\omega_b^2\right]$, where α_p and ω_b are the electron-phonon coupling strength and the phonon cutoff frequency, respectively. The set of Eqs. (4.12) is solved numerically in a self-consistent manner.

It is now instructive to examine the behavior of f_m in two limiting cases from Eq. (4.11): (i) In the limit $|\Omega| \ll \omega_m$, we find $f_m \approx \lambda_m$, corresponding to the full polaron transformation [217]. Here, the driving field is sufficiently weak that the bath oscillators can adiabatically follow the excitonic motion, becoming fully displaced when the system occupies its excited state, as dictated by the coupling term in H'. (ii) Conversely, when $|\Omega| \gg \omega_m$, the variational parameter f_m becomes negligibly small, indicating that the transformation induces little to no displacement. In this regime, the excitonic dynamics are too rapid for the relevant phonon modes to respond, and their displacements are therefore strongly suppressed. Later we can observe that this distinction has significant physical implications for driven quantum dots at high driving strengths. The inability of the phonon environment to follow the system dynamics leads to a reduction in phonon-induced damping. This key feature can be captured naturally within the variational framework.

4.2.2 Variational master equation

To study the ME in the variational frame [49], we must first evaluate the relevant correlation functions. From the interaction Hamiltonian Eq. (4.9c), it becomes evident that the variational transformation introduces two distinct types of contributions, one resembling that of the polaron theory, and the other similar to the weak-coupling approach. As a result, the final ME naturally consists of three components: weak-coupling–like terms, polaron-like terms, and cross terms that originate from the interaction between the two kinds of bath operators. In the limiting cases, it smoothly reduces to either the weak-coupling or the polaron description. However, under general conditions, both types of contributions coexist. The cross terms play a crucial role, enabling the theory to interpolate seamlessly between the weak-coupling and polaron regimes. Thus it captures a broader range of physical behavior than either approach alone. We can now obtain the variational ME including the radiative and dephasing rates as

$$\frac{\partial\rho}{\partial t} = -\frac{i}{\hbar}[H_{SV},\rho] + \frac{\gamma}{2}\mathcal{L}[\sigma^-]\rho + \frac{\gamma'}{2}\mathcal{L}[\sigma^+\sigma^-]\rho + \mathcal{L}_{ph}\rho \tag{4.13}$$

where $\sigma^+ = |1\rangle\langle 2|$, $\sigma^- = |2\rangle\langle 1|$ are raising and lowering operators of the system respectively. The Lindblad superoperator, $\mathcal{L}[\hat{O}]\rho = 2\hat{O}\rho\hat{O}^\dagger - \hat{O}^\dagger\hat{O}\rho - \rho\hat{O}^\dagger\hat{O}$ acting

on a operator $\hat{O}$. The radiative decay and dephasing are denoted by γ and γ', respectively. The term $\mathcal{L}_{ph}$ includes phonon bath in system dynamics is given by,

$$\mathcal{L}_{ph} = -\frac{1}{\hbar^2}\int_0^\infty \sum_{ij}\{C_{ij}(\tau)[X_i(t), X_j(t,\tau)\rho(t)] + H.c.\}\, d\tau \tag{4.14}$$

where $i,j \in x,y,z$, $X_j(t,\tau) = e^{-iH_{SV}\tau/\hbar}X_j(t)e^{iH_{SV}\tau/\hbar}$ and the correlation functions are,

$$C_{xx}(\tau) = \langle B\rangle^2\{\cosh[\phi(\tau)] - 1\}, \tag{4.15a}$$
$$C_{yy}(\tau) = \langle B\rangle^2 \sinh[\phi(\tau)], \tag{4.15b}$$

and $C_{xy}(\tau) = C_{yx}(\tau) = 0$. The dependence on the phonon propagator is given by

$$\phi(\tau) = \int_0^\infty \frac{J(\omega)F(\omega)^2}{\omega^2}\left[\coth\left(\frac{\beta\hbar\omega}{2}\right)\cos(\omega\tau) - i\sin(\omega\tau)\right]d\omega. \tag{4.16a}$$

It depends on the variational parameters through the term $F(\omega)$. We can also find the weak-coupling and cross-coupling correlation functions $C_{zz}(\tau)$, and $C_{yz}(\tau)$ as [49]

$$C_{zz}(\tau) = \int_0^\infty J(\omega)\left[1 - F(\omega)\right]^2\left[\coth\left(\frac{\beta\hbar\omega}{2}\right)\cos(\omega\tau) - i\sin(\omega\tau)\right]d\omega, \tag{4.17a}$$
$$C_{yz}(\tau) = -\langle B\rangle\int_0^\infty \frac{J(\omega)F(\omega)}{\omega}\left[1 - F(\omega)\right]\left[\coth\left(\frac{\beta\hbar\omega}{2}\right)\sin(\omega\tau) + i\cos(\omega\tau)\right]d\omega, \tag{4.17b}$$

and also $C_{zy}(\tau) = -C_{yz}(\tau)$, $C_{zx}(\tau) = C_{xz}(\tau) = 0$. Now we can find all the phonon induced decay rates by using Eq. (4.14) shown in the Appendix.

4.2.3 Rapid adiabatic passage in two-level system

Besides spectroscopy, it is of profound importance to prepare a specific quantum state in semiconductors for different fields like quantum computation [218, 219], single and entangled photons [220, 221], Bose-Einstein condensation[222]. RAP is an advantageous way to prepare a state as it remains insensitive to the variation of the laser field intensity or the pulse area beyond the adiabatic threshold. The population change between the two-level atomic states can happen in two distinct adiabatic ways. To understand the two processes, we use the well-known dressed state (adiabatic state) eigenvectors of a time-dependent Hamiltonian of a two-level system interacting with a chirp pulse of Rabi frequency Ω_1 is given as [223]

$$|\psi_+(t)\rangle = \sin\theta(t)\ |2\rangle + \cos\theta(t)\ |1\rangle, \tag{4.18a}$$
$$|\psi_-(t)\rangle = \cos\theta(t)\ |2\rangle - \sin\theta(t)\ |1\rangle, \tag{4.18b}$$

where the instantaneous eigenstates are the linear superposition of the bare states (diabatic state). The mixing angle $\theta(t)$ between the states is defined by

$$\sin 2\theta = \frac{|\Omega_1(t)|}{\sqrt{\Delta_1(t)^2 + |\Omega_1(t)|^2}}, \tag{4.19a}$$
$$\cos 2\theta = \frac{\Delta_1(t)}{\sqrt{\Delta_1(t)^2 + |\Omega_1(t)|^2}}, \tag{4.19b}$$

where $\Delta_1(t)$ is the time-dependent detuning. We can also, obtain the eigenvalues of the dressed state which are given by

$$E_{\pm} = \frac{\hbar}{2}\left[\Delta_1(t) \pm \sqrt{\Delta_1(t)^2 + |\Omega_1(t)|^2}\right]. \tag{4.20}$$

Indeed, we can write the Hamiltonian in the adiabatic basis as

$$H_a = \hbar \begin{bmatrix} E_- & -i\dot{\theta} \\ i\dot{\theta} & E_+ \end{bmatrix}. \tag{4.21}$$

The adiabatic condition requires that the maximum rate of change in the adiabatic states, $|\psi_{\pm}\rangle$ must be smaller than the minimum difference between the eigenvalues [223]. Thus the adiabatic condition reads

$$|\dot{\theta}(t)| \ll |E_+(t) - E_-(t)|. \tag{4.22}$$

Now for the case of (i) constant detuning, we can infer from Eq. (4.20) that the energies of the dressed states remain parallel to each other long before and after the interaction with a pulsed laser. Only during the pulse interaction time, the states are in the superposition of the bare states. Therefore, in this case, the population completely return to its initial state, which is the no-crossing scenario of adiabatic evolution. In another case of (ii) time-dependent detuning, *i.e.*, when the frequency sweeps adiabatically from a large negative value to a large positive value (or vice versa) two limits arise, (a) for large negative detuning ($|\Omega_1(t)| \ll |\Delta_1(t)|$),

$$\begin{aligned} &E_+ \to 0; \quad E_- \to -\hbar\Delta_1, \\ &|\psi_+\rangle \to |2\rangle; \quad |\psi_-\rangle \to -|1\rangle, \end{aligned} \tag{4.23}$$

and (b) for large positive detuning ($|\Omega_1(t)| \ll |\Delta_1(t)|$),

$$\begin{aligned} &E_+ \to \hbar\Delta_1; \quad E_- \to 0, \\ &|\psi_+\rangle \to |1\rangle; \quad |\psi_-\rangle \to |2\rangle. \end{aligned} \tag{4.24}$$

Both the two limits assert that the initial population in state $|2\rangle$ adiabatically follows $|\psi_+\rangle$ during the frequency-swept and finally makes an inversion to state $|1\rangle$. This is called the avoided crossing or anticrossing in adiabatic evolution. It is also called rapid as the process should occur shorter than the lifetime of the excited state.

4.3 Numerical results

4.3.1 RAP-based spot formation

Under the adiabatic condition, a two-level system interacting with a Gaussian chirp pulse can robustly transfer the population from one state to another. We have used two such sequential Gaussian chirp pulses with opposite chirping. To perform the computation with the system parameters, we need to normalize it to a dimensionless quantity. We have chosen the normalized frequency $\gamma_n = 1$ rad ps^{-1} and time $\tau_n = 1/\gamma_n$. In Fig. 4.2, we have plotted the excited state population as a function of the pulse area and chirp (α) of the pulse without taking the interaction with phonon

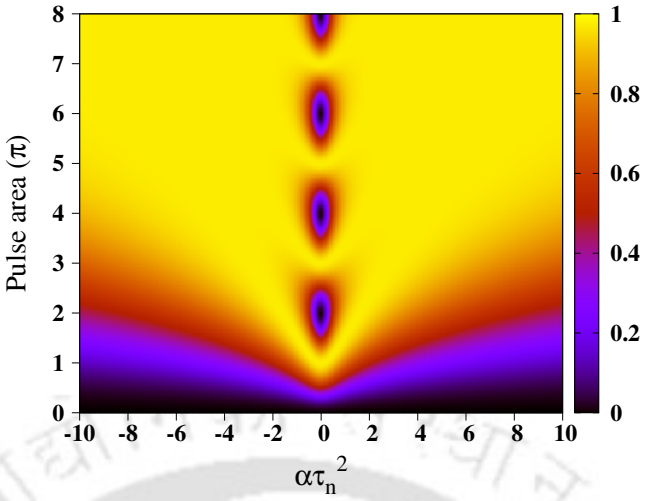

Figure 4.2: Excited state population as a function of pulse area and chirping. The color bar denotes the population of the excited state.

bath. We find if there is no chirp ($\alpha\tau_n^2 = 0$), we get the usual Rabi oscillation *i.e.*, for the odd multiple of π the population transfer to the excited state whereas for even multiple of π it remains in the ground state. Also, we notice that robust population transfer can happen due to RAP for several parameters that satisfy the conditions, $|\alpha|\tau_n^2 >> 1$ and $|\alpha|\tau_n^2 << \Omega_0^2\tau_n^2$. Here Ω_0 is the peak Rabi frequency of the chirped pulse. As in Fig. 4.3, the first pulse peaked at $\gamma_n t = 10$, Rabi frequency $\Omega_G^0 = 4.0\gamma_n$, positive chirp $\alpha_G = 3.24$ ps^{-2} and having pulse area $> \pi$ takes the population to the excited state that was initially in the ground state. The next pulse is peaked at $\gamma_n t$ = 15, Rabi frequency $\Omega_D^0 = 10.4\gamma_n$, with a negative chirp α_D = - 3.24 ps^{-2} which returns back the population to the ground state. As demonstrated in Fig. 4.3, the influence of phonons is negligible at low temperature. However, as the temperature increases, such as at 50K, the efficiency of population transfer becomes hindered due to phonon decoherence effects. We have taken the additional parameters for InGaAs/GaAs QDs which are used in [216]. The phonon cutoff frequency ω_b = 2.2 ps^{-1}, and we choose $\gamma = \gamma' = 1$ μeV. The second pulse is implemented in a short interval of the first to make the population return efficiently so that the two pulses act like an on-off switch. This efficient population transfer and return is crucial for imaging based on this scheme. The frequency-swept is adiabatic so that $\Omega_0^2 >> |d\Delta/dt|$.

Now for RAP-based imaging, the system is driven by two spatiotemporal beams with SG and LG spatial profiles shown in Figs. 4.4(a) and 4.4(b) respectively. The SG and LG beam waists are $1.7l$ and $1.0l$, respectively. Here l is a characteristic length defined by $l = \mathrm{f}/(\mathrm{k}\sigma)$ [182]. The lens f's focal length is 3.7mm., the wavevector $k = 2\pi n/\lambda$. We take the refractive index of the gallium phosphide (GaP) solid emersion lens, $n = 3.5$, and wavelength of the laser $\lambda = 940$ nm. The spatial extent of the beam before focusing on a lens is taken as $\sigma = 1.2$ mm. So, the characteristic length l becomes 131.86 nm. This can be regarded as the beam's spot size when it is focused through a lens for the above parameters. The Rabi frequency of the SG beam is $\Omega_G^0 = 4.0\gamma_n$ and for the LG beam, is $\Omega_D^0 = 10.4\gamma_n$. Successively implementing SG and LG spatiotemporal beams produce a spot size of $\Delta \mathrm{x}_{\mathrm{FWHM}}/l = 0.2$ *i.e.*, 26.37 nm

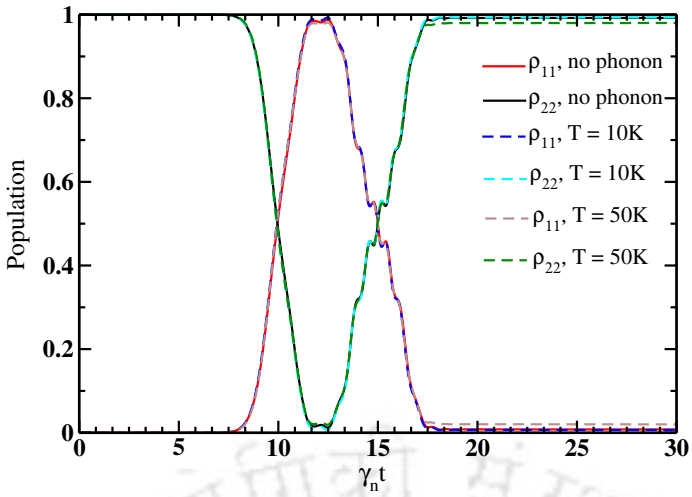

Figure 4.3: Population transfer via RAP. The first pulse with positive chirp of 3.24 ps^{-2} and pulse area greater than π transfers the population to the excited state and the subsequent pulse with chirp -3.24 ps^{-2} and pulse area greater than π bring down the excited state population to ground state. Both the pulse has a width $1.3\tau_n$. The electron-phonon coupling strength $\alpha_p = 0.027$ ps^2.

at T = 4K. In Fig. 4.5, we show the excited state population distribution at $\gamma_n t = 30$. We observe that the central peak is not much distorted at lower temperatures. Other than the central peak, small side peaks appear due to the population transition to the excited state due to the LG beam. At higher temperature T = 50K we find the side peaks as well as the central peak distort considerably. The tail of the SG beam fails to take all the population to the excited state, leaving it partially in the ground

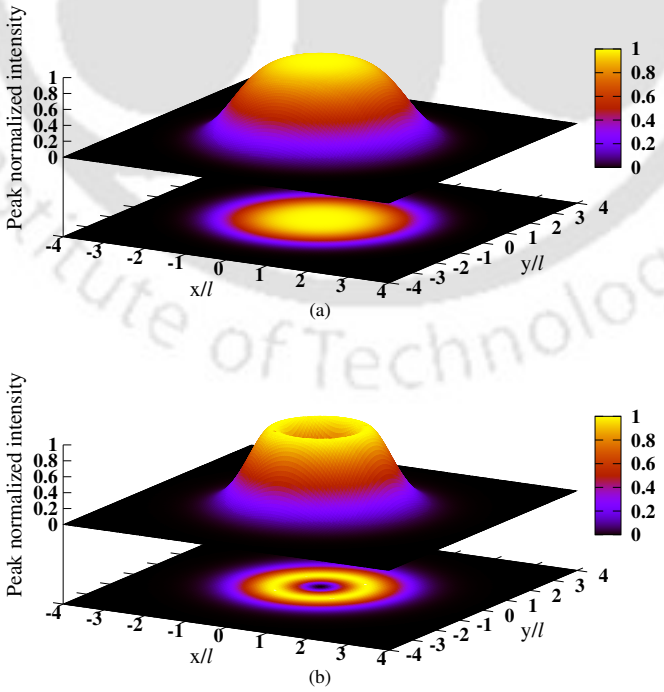

Figure 4.4: The 3-D intensity distribution of (a) SG beam of width $1.7l$ and (b) LG spatiotemporal beam of width l

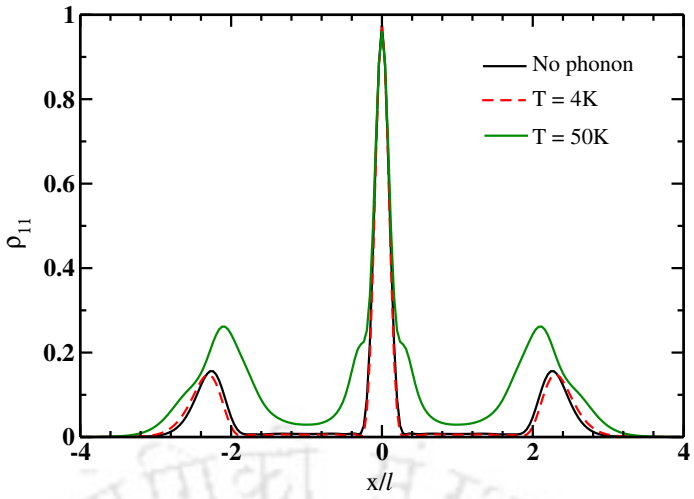

Figure 4.5: Population of the excited state vs. spatial extent in QD system. The applied spatiotemporal beams SG has waist $w_G = 1.7l$, and LG has waist $w_D = l$. The spatial distribution of the excited state population is shown at $\gamma_n t = 30$. Other parameters are the same as in Fig. 4.3.

state. However, the LG beam partially takes this leftover population to an excited state. We choose the beam waist judiciously so that the side peaks remain minimum and far apart from the central maximum. Figure 4.6(a) shows the central spot in the 2d plane. Also, we can detect multiple QDs at different preassigned locations given in Fig. 4.6(b). Thus, applying the SG and LG beams successively give a smaller spot size of the QDs emitters.

As we observe at lower temperature the phonon effect is negligible on spot formation, we next analyzed the dependence of the FWHM of the QD spot with the intensity of the LG beam in Fig. 4.7. The flat top portion of the SG beam, which exists between the spatial range $x/l = \pm 1$, takes all population from the ground state to the excited state. The central peak develops due to the population presence in the excited state at the center $x/l = 0$, where the intensity of the LG beam becomes zero. This is true for taking the orbital angular momentum index as 1 (LG_0^1)

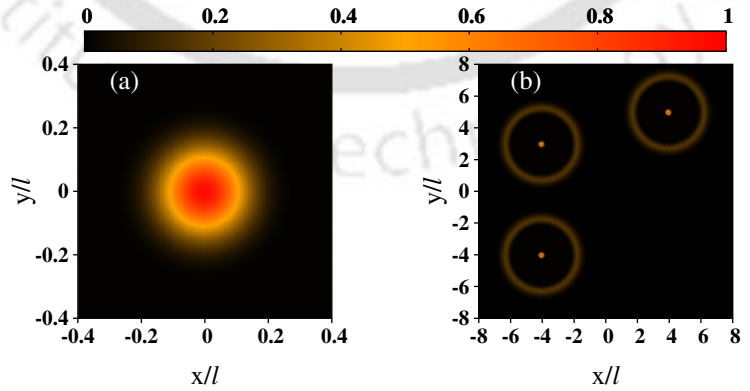

Figure 4.6: The 2-D spot size of (a) single QD emitter at (0,0). The outer ring is at a higher radius which is not shown here, (b) Multiple emitters at a preassigned position (-4,-4) bottom left, (-4,3) top left and (4,5) top right. Here we can see the low intense outer rings. At low temperature as phonon effect is negligible its effect is not considered. The parameters are the same as in Fig. 4.5.

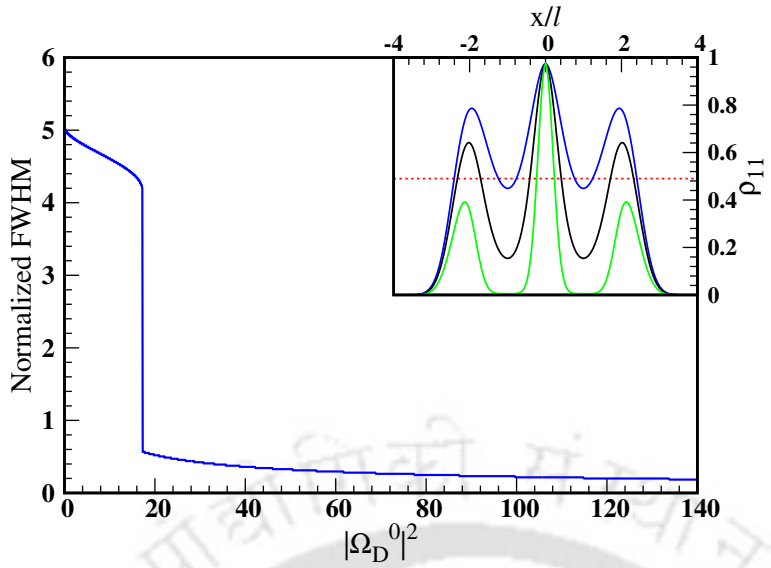

Figure 4.7: FWHM of the spot is plotted against the intensity of the spatiotemporal LG beam. The inset shows the excited state population for different LG intensities. The blue, black, and green solid lines correspond to $|\Omega_D^0|^2 = 4$, 9, 25 respectively. The red dotted line represents half of the central maximum.

in Eq. (4.2b). This point singularity is the key to achieving sharp resolution at the QD center. The intensity peaks of the LG beam appear at $x/l = \pm 1$, leading to stimulated emission from the excited state to the ground state. Subsequently, a dip is observed in the excited state population ρ_{11} as shown in the inset of Fig. 4.7. The central peak accompanied by shallow dips gives rise to a larger FWHM. By increasing the LG beam's intensity, the spatial distribution of the excited state population at $x/l = \pm 1$ goes to zero very sharply. Hence, the inset of Fig. 4.7 reveals the reason behind the narrow spot size formation, which can be made possible by the doughnut beam-assisted complete excited state depopulation. Before the sharp fall of the FWHM the doughnut beam intensity is very low. By slowly increasing the doughnut beam intensity and keeping the SG beam fixed, much of the population transfers to the ground state. In this context, the peak after the dip in the excited state population occurs due to tail of the LG beam where the intensity is lower than $x/l = \pm 1$. The inset of Fig. 4.7 (blue and black solid lines) illustrates these phenomena. The red dotted line in the inset of Fig. 4.7 indicates the intensity level at half of the central maximum, while the green solid line illustrates a typical scenario in which a side peak occurs below this intensity threshold. It is to be noted that arbitrary enhancement of the intensity up to a larger extent is prohibited because of photobleaching or may even damage the live sample [224, 225].

4.3.2 Reduction of side peak

It is evident from the previous analysis that the formation of side peaks around the central maximum of the QD spot is inevitable by considering the fields whose spatial envelopes represent by Eqs. (4.1a) and (4.1b). Even though these side peaks are small, these peaks may degrade the resolution where several QDs emitters are present within the specific range. So, finding the modulated fields which will decrease the side peak nearly to zero is pertinent. A complete suppression of residual ground state

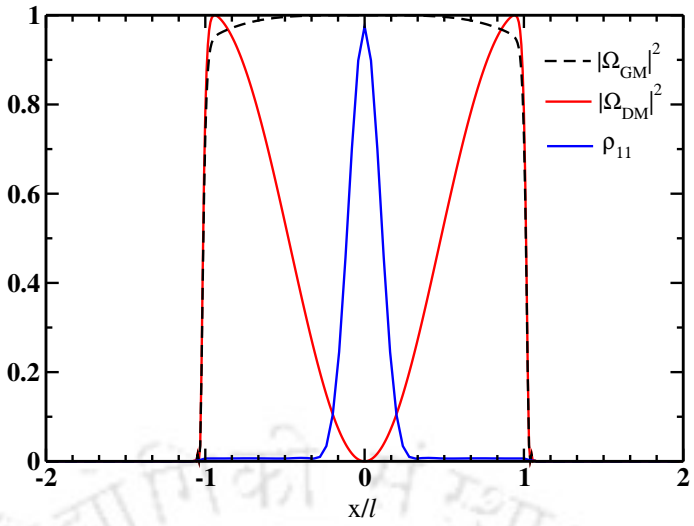

Figure 4.8: Normalized peak intensities of Bessel-modulated SG, Bessel-modulated LG beam and the population of the excited state are plotted against spatial extent. The red solid line, and the black dotted line correspond to the modulated LG and SG beams, respectively. Both the beams are truncated at $x/l = 1.05$. Other parameters are the same as in Fig. 4.4.

population flow is possible by considering the truncated beams which are formed by the Bessel-modulated SG and Bessel-modulated LG beams given as

$$\vec{E}_{GM}(r,t) = \hat{\sigma}_{-}\mathcal{E}_G(r,t)\left[a_1 J_0(r^{36}) + a_2 J_2(r^{36})\right], \tag{4.25a}$$

$$\vec{E}_{DM}(r,t) = \hat{\sigma}_{-}\mathcal{E}_D(r,t)\left[b_1 J_0(r^{36}) + b_2 J_2(r^{36})\right]. \tag{4.25b}$$

Here $J_i(i \in 0,2)$ is the Bessel function of the first kind with order i, a_i and b_i are modulation coefficients (real numbers) which we have chosen, $a_1 = a_2 = 1.5$, $b_1 = b_2 = 1.0$. The modified Rabi frequencies of modulated LG and SG beams are Ω_{DM}, Ω_{GM} respectively. In Fig. 4.8, the two modulated beams are truncated at $x/l = \pm 1.05$, which can be obtained experimentally by finite apertures. The modulated SG beam takes all the population from the ground state to the excited state. Due to the sharp fall of the modulated SG intensity at $x/l = \pm 1.05$, the ground state population beyond the spatial range, $x/l = 0$ to $x/l = \pm 1.05$ cannot be excited to the excited state. Similarly, the excited state population goes through stimulated emission by the modulated LG beam keeping only the population at the center $x/l = 0$. Keeping the spot size of the QD emitter the same as Fig. 4.5, we can reduce the side peak nearly to zero.

4.3.3 Decoupling of phonons

The phonon-induced decay rates will affect the population distribution among the QD states for different temperatures. To study the dependence we have solved the variational ME in Eq. (4.13) where all the decoherence rates are taken into account. The variational ME approach provides a unified and consistent framework for analyzing systems under both strong driving and strong exciton–phonon interactions. Notably, it seamlessly incorporates the weak-coupling and polaron ME as its limiting cases. A Gaussian pulse interacting with a two-level QD system induces Rabi oscillations (RO) of the excited state population. In Fig. 4.9(a), we present the

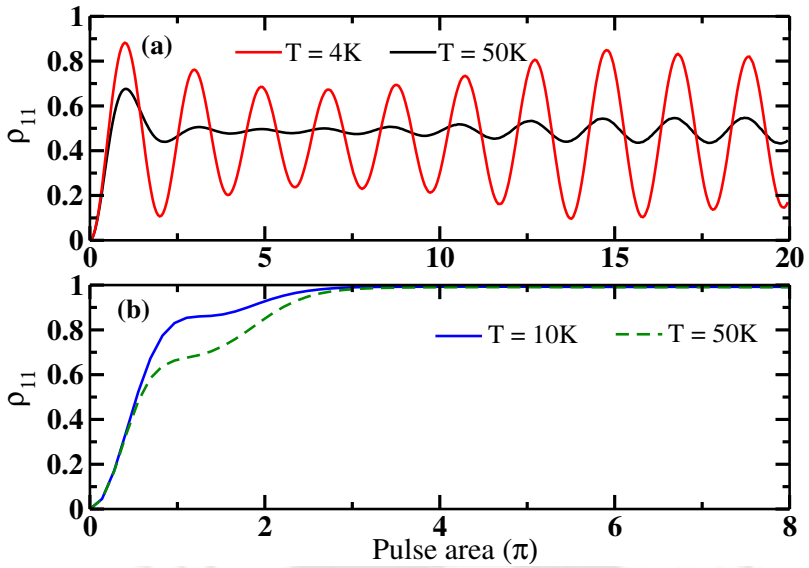

Figure 4.9: QD excited state population as a function of pulse area. (a) Transform-limited (pulse without chirping) Gaussian and (b) Gaussian chirp pulse of chirping 3.24 ps^{-2} and a pulse of width $1.3\tau_n$ is used. The electron-phonon coupling strength $\alpha_p = 0.027$ ps^2.

excited state population as a function of the pulse area of a transform-limited (pulse without chirping) Gaussian pulse. Typically, RO in quantum dots are measured by recording the rotation of the Bloch vector after a pulse of specified duration as a function of the pulse area. In the literature [194], these signals are characterized as Rabi rotations (RR) to differentiate them from the temporal evolution occurring during the pulse, which is referred to as RO. In Fig. 4.9(a), the Gaussian pulse is centered at $\gamma_n t = 0$. Our findings indicate that the damping of RR displays a non-monotonic dependence on the pulse area. For small pulse areas, the amplitude of the RR diminishes with increasing pulse area, reflecting the expected damping behavior due to the interaction between a QD exciton and acoustic phonons. Conversely, for large pulse areas, the amplitude increases again, an observation that resembles un-damping. This behavior is thus termed the 'reappearance of RR'. It is important to note that the reappearance of RR differs from the collapse-and-revival phenomenon [226] associated with the time-dependent RO in the well-known Jaynes-Cummings (JC) model, which exhibits periodic collapse and revival of RO in the time domain. In contrast, the reappearance of RR as a function of pulse area does not experience subsequent decay. We also note that at T = 4K and T = 50K, the amplitude of the RR is higher and lower, respectively, due to temperature-dependent phonon effects. At small pulse areas, the RR can be described using the polaron transformation; however, as the pulse area increases and satisfies the condition $|\Omega| > \omega_b$, the polaron ME no longer remains valid. At higher pulse areas, the variational theory can accurately describe the exciton-phonon decoupling effect observed in weak-coupling dynamics. The damping of the RR is also affected by the size of the quantum dot [227]. Furthermore, the reappearance of the RR is significantly dependent on the pulse width of the excitation [228]. Utilizing positively chirped Gaussian pulse with short pulse width allows for the observation of the reappearance regime at reduced pulse areas. Figure 4.9(b) illustrates the excited state population when a positively chirped Gaussian pulse is used. Our investigation indicates that a pulse area greater

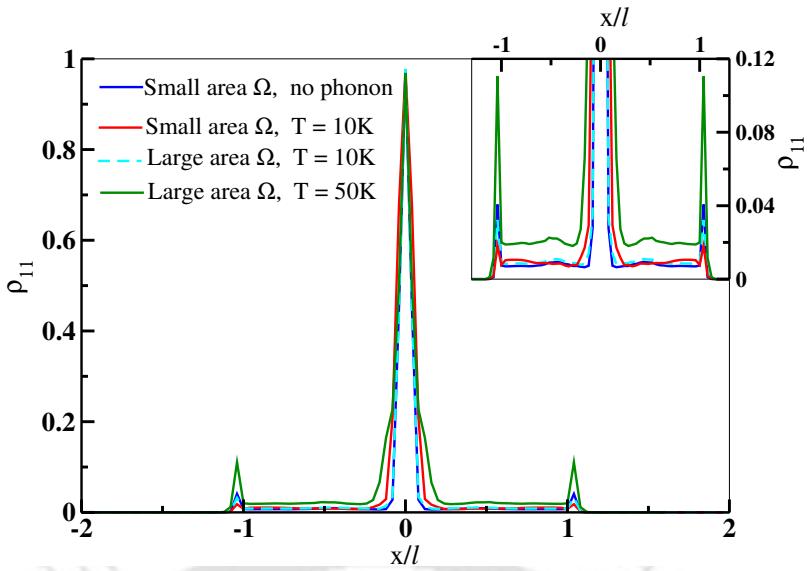

Figure 4.10: Spot size of QD emitter including and without including phonon coupling. Small area $\Omega^0_{SG} = 8\gamma_n$, $\Omega^0_D = 20.8\gamma_n$. Larger $\Omega^0_{SG} = 12\gamma_n$, $\Omega^0_D = 31.2\gamma_n$. Chirping and other parameters remain same as Fig. B.2. The modulation coefficients for truncated beams are $a_1 = a_2 = 1.5$, $b_1 = b_2 = 1.0$. A spot size of $\Delta x_{\mathrm{FWHM}}/\ell = 0.08$ *i.e.*, 10.54 nm is observed at T = 10K.

than 3π can efficiently transfer population to the excited state. Fulfilling the adiabatic condition, as discussed earlier, the population transfer becomes robust, unlike in transform-limited pulses, and is also less sensitive to intensity fluctuations. It is evident that the distortion in QD spot could be reduced by decoupling exciton-phonon interactions when stronger spatiotemporal beams are employed. We plot the excited state population in Fig. 4.10 as a function of spatial extent. This shows that at T = 10K and with a small pulse area, the spatiotemporally modulated beam creates a spot that is subject to distortion. However, as the beam strength increases, a decoupling regime can be achieved where phonon effects are effectively mitigated. Additionally, as the temperature increases, there is a gradual reemergence of distortion. Significant distortion can be identified in the inset of Fig. B.3. At T = 10K, the side peaks remain below 6% of the central maximum, which is negligible. This negligible spike originates from the abrupt truncation of the high-order Bessel-modulated beam profile at $x/l = \pm 1.05$. However, at higher temperatures, such as T = 50K, these side peaks exceed 10% of the central maximum, degrading the resolution in an ensemble of quantum dots. Beyond T = 50 K, the central maximum also experiences significant distortion, severely compromising the sharpness of the spot.

4.4 Discussion

In the present work, we demonstrate that robust population transfer can be achieved through RAP using spatio-temporal chirped pulses. Chirped laser pulses are particularly effective in semiconductor QDs for preparing selected electronic states and enabling controlled excitation processes [185]. However, generating and accurately controlling such chirped pulses in experiments remains technically demanding due to the variety of available methods and the precision required [185, 229]. In addition, the interaction of the two-level QD system with the phonon bath introduces phonon-

TH-3976_186121017

mediated dephasing, which can influence the excitation dynamics and consequently affect the quality of image formation. Therefore, it is important to investigate the impact of temperature and phonon interactions on the system. An experimental demonstration has been reported using a positively chirped Gaussian beam and a negatively chirped doughnut beam [182]. In our study, we further improve the beam structure by employing Bessel-modulated truncated structured LG and SG beams, which effectively suppress the unwanted circular ring surrounding the central spot. To analyze the system dynamics, we adopt a variational ME approach [49], which is well suited for describing both strong driving conditions and strong exciton–phonon interaction regimes. Our results show that at small pulse areas, the image can experience distortion due to phonon-mediated decay. However, as the pulse area increases, the influence of phonons is significantly reduced, leading to improved population transfer and image quality. These findings open a pathway toward coherent control of excitons in semiconductor quantum dots with minimal phonon-induced disturbances [230, 231].

4.5 Conclusion

In conclusion, we have theoretically studied RAP-based imaging in semiconductor QD systems. For this purpose, we have adopted a semi-classical treatment for describing the spatiotemporal beams that interact with the two-level QD system. We use dressed state analysis to understand the RAP-assisted population transfer in the presence of chirping pulses. The phonon vibration in a semiconductor quantum dot system is inevitable at finite temperatures. To encompass the temperature-dependent phonon-induced decoherence rates for super-resolution imaging formation, we explore variational ME. We also show how the QD emitter's spot size depends on the LG field intensity. The compromise of image resolution in an ensemble of dense QDs is because of the circular ring. The dominant character of the LG beam tail over the SG beam tail causes residual population flow from the ground state to the excited state, creating the circular ring. Further, we have used the modulated truncated beams to overcome the image distortion. Our analysis indicates that, although phonon-induced decoherences at finite temperatures adversely affect image resolution, an increase in field strength allows for the mitigation of these decoherences. This can be achieved by entering a regime where the exciton-phonon interaction can be effectively decoupled. Hence, this investigation may have potential applications in nano-scale imaging, with scalability and controllability.

Chapter 5

Conclusions and future outlook

In conclusion, this thesis has explored the tailoring of scalar and vector beams in an atomic medium and investigated super-resolution imaging using structured beams in a QD system. Although these three research problems are distinct in scope, they are unified by a central theme: the coherent control of spatial resolution aimed at minimizing the optical spot size. The pursuit of enhanced optical resolution has far-reaching implications across scientific disciplines. The diffraction limit once appeared as a fundamental barrier imposed by the wave nature of light, advances in nonlinear and coherent-control-based imaging have enabled resolution far beyond this classical boundary. Spatial resolution enhancement through coherent control has profound implications. In biological imaging, it enables visualization of structures previously inaccessible to conventional microscopy, revealing molecular interactions and nanoscale organization inside living cells. In atomic physics and quantum information, it allows site-selective addressing of atoms in optical lattices or tweezer arrays. In the following, we provide a concise summary of the key findings from each research investigation and outline promising directions for future work.

In Chapter 2, we investigated the linear and nonlinear optical response of an atomic medium when illuminated by CV beams. The medium is modelled as a nondegenerate four-level closed-loop system, where the CV beam serves as a weak probe in the presence of a strong control field. The closed-loop configuration plays a key role in enabling phase-dependent modulation of the probe susceptibility. By varying the phase shift between the probe and control fields, we observe that the linear susceptibility of both components of the probe vector beam changes due to interference among multiple quantum pathways. In particular, at a phase shift of $\beta = 0$, the medium exhibits absorption, whereas at $\beta = \pi/2$, it displays gain; the corresponding polarization evolution also differs. For $\beta = 0$, the polarization ellipse undergoes a uniform 90^0 rotation across the transverse plane for radial, azimuthal, and spiral vector beams after propagating one Rayleigh length. In contrast, $\beta = \pi/2$ leads to both polarization rotation and changes in ellipticity. Extending the study to higher atomic densities and stronger probe intensities, we observe that the emergence of third-order nonlinearity induces chain-like self-focusing and defocusing patterns for all three types of CV beams. The associated reduction in spot size highlights potential applications in resolution enhancement, while the observed chain-like propagation structures may prove useful in optical trapping schemes.

In Chapter 3, we examine the focusing behaviour of both scalar and vector beams in an active Raman gain (ARG) atomic medium. In the first configuration, a scalar

TH-3976_186121017

probe beam interacts with a strong control field and a signal field in a four-level system. Using the probability-amplitude method, we analytically derive the linear and third-order Kerr susceptibilities and show that a giant cross-Kerr nonlinearity can be achieved, supported by a finite detuning of the continuous-wave signal field. By choosing appropriate input intensities and tailoring the spatial profile of the control field, we can observe focusing of the scalar probe beam. Although both self-Kerr and cross-Kerr nonlinearities contribute to this behaviour, the cross-Kerr effect produces a substantially smaller beam waist, enabling strong spatial compression. We then compare this configuration with the case where the probe is a VB. For the vector probe, we observe gain-assisted narrowing arising from energy transfer from the strong control beam, and we analyse the state of SOP at the minimum beam waist. Overall, the focusing characteristics revealed in this chapter demonstrate that significant spot-size reduction is achievable, offering promising applications in high-resolution optical microscopy.

In Chapter 4, we shift our focus to a QD system and investigate rapid adiabatic passage (RAP)–based super-resolution imaging using structured light. Two spatiotemporally engineered beams, specifically, SG and LG beams interact with a two-level QD, where an appropriate choice of their temporal delay, chirp, and spatial envelope enables sub-diffraction image formation. To clarify the mechanism of RAP-assisted population transfer, we employ a dressed-state analysis for the two-level system. Furthermore, we incorporate a variational master equation to examine how temperature-dependent phonon-induced decoherence influences super-resolution performance. Our results show that the final QD emitter spot size is determined by the LG beam intensity. We also address the appearance of unwanted circular rings in the image, which arise due to the dominance of the LG beam tail over that of the SG beam. This issue is mitigated by introducing Bessel-modulated truncated beams. Although phonon-induced decoherence at finite temperatures degrades image resolution, increasing the pulse area enhances field strength and we observe decoupling of the exciton from the phonon bath, thereby restoring high resolution. The outcomes of this work highlight the potential of RAP-driven structured-beam protocols for scalable and controllable nanoscale imaging.

In this thesis, the analysis of beam evolution has been carried out within the paraxial approximation, a regime that successfully describes optical fields when the beam waist is much larger than the wavelength of the light. However, many emerging optical applications now operate in regimes where this assumption breaks down. Strong focusing, high-NA objectives, tightly confined vector beams, and nanophotonic structures all introduce inherently nonparaxial behavior. A natural progression of the present work would therefore be to investigate nonparaxial beam propagation [232], which could provide deeper insight into fundamental resolution limits and enable the development of next-generation light–matter interaction schemes. Incorporating full vector Maxwell solvers would enable the study of beam dynamics for more accurate modelling of advanced optical systems [233].

We have introduced the classical Stokes parameters, which give a complete description of the polarization state of light and can be visualized on the Poincaré sphere. To generalize this framework to nonclassical light, one defines quantum Stokes parameters through operator representations of polarization, which are subject to quantum uncertainty relations. A state of light is considered polarization-squeezed when the variance of one or more Stokes operators falls below the corre-

sponding shot-noise level of coherent light [234]. With the rapid progress in quantum information processing, nonclassical polarization states have become increasingly important. Quantum Stokes operators also provide a powerful tool for mapping optical polarization states onto the spin variables of atoms in excited states, offering a route for transferring quantum information from optical carriers to matter [235]. VBs, with their inhomogeneous transverse polarization structure, are particularly promising in this context. In particular, quadrature-squeezed vector beams offer a potential platform for exploring hybrid quantum entanglement between polarization and transverse spatial degrees of freedom [236].

We have so far examined the propagation dynamics of both scalar and vector beams in atomic media, highlighting how nonlinearity and polarization structure govern their evolution. These studies provide a comprehensive understanding of the response of the medium under isotropic conditions. Many contemporary photonic platforms employ chiral materials whose response depends on the handedness of light [237]. The interaction of chiral material with the left and right circularly polarized light is known as optical activity. Initially, it was believed to arise only from circularly polarized light carrying spin angular momentum. However, later studies revealed that light carrying OAM can also interact with chiral matter [238]. Consequently, vortex beams and VBs with OAM emerge as promising candidates for probing chiral media. Their interaction can potentially lead to effects such as asymmetric absorption, optical rotation, circular dichroism, and even directional emission, opening new avenues for exploring chiro-optical phenomena.

Indian Institute of Technology Guwahati

Appendix A

Appendix of chapter 2

The explicit expressions for $A - H$ are as follows

$$A = \Gamma_{12}\Gamma_{14}\Gamma_{24}\left(\Gamma_{13}+\Gamma_{31}\right)\Gamma_{34}\Gamma_{42}, \tag{A.1a}$$

$$B = \left|\Omega_c\right|^2\left[\Gamma_{24}(\Gamma_{13}+\Gamma_{31})(\Gamma_{12}+\Gamma_{34})\Gamma_{42} - \Gamma_{14}(\Gamma_{24}\Gamma_{31}\Gamma_{34} + (\Gamma_{12}(\Gamma_{13}+\Gamma_{31}) + \Gamma_{31}\Gamma_{34})\Gamma_{42})\right], \tag{A.1b}$$

$$C = \left(\Gamma_{14}+\Gamma_{32}\right)\left(\Gamma_{12}+\Gamma_{34}\right)\left|\Omega_c\right|^2 + \Gamma_{12}\Gamma_{14}\Gamma_{32}\Gamma_{34}, \tag{A.1c}$$

$$D = -4\left(\Gamma_{13}+\Gamma_{31}\right)\left(\Gamma_{24}+\Gamma_{42}\right)\left|\Omega_c\right|^2 + \Gamma_{24}\Gamma_{31}\Gamma_{42} + \Gamma_{13}\left(\Gamma_{24}\Gamma_{31} + \left(\Gamma_{24}+\Gamma_{31}\right)\Gamma_{42}\right), \tag{A.1d}$$

$$E = \Omega_c^2[\Gamma_{12}\Gamma_{13}(\Gamma_{14}+\Gamma_{31})(\Gamma_{24}+\Gamma_{42}) + \Gamma_{34}(\Gamma_{14}\Gamma_{24}\Gamma_{31} + \Gamma_{13}(\Gamma_{24}(\Gamma_{14}+\Gamma_{31}) + \Gamma_{31}\Gamma_{42}))], \tag{A.1e}$$

$$F = \Gamma_{13}\Gamma_{21}\Gamma_{23}\Gamma_{31}\left(\Gamma_{24}+\Gamma_{42}\right)\Gamma_{43}, \tag{A.1f}$$

$$G = \left|\Omega_c\right|^2\left[\Gamma_{13}(\Gamma_{21}\Gamma_{31}(\Gamma_{24}+\Gamma_{42}) + (\Gamma_{31}(\Gamma_{24}+\Gamma_{42}) - \Gamma_{23}\Gamma_{42})\Gamma_{43}) - \Gamma_{23}\Gamma_{31}(\Gamma_{21}(\Gamma_{24}+\Gamma_{42}) + \Gamma_{42}\Gamma_{43})\right], \tag{A.1g}$$

$$H = \Omega_c^2[\Gamma_{21}\Gamma_{24}(\Gamma_{13}+\Gamma_{31})(\Gamma_{23}+\Gamma_{42}) + (\Gamma_{24}\Gamma_{31}\Gamma_{42} + \Gamma_{13}(\Gamma_{24}\Gamma_{42} + \Gamma_{23}(\Gamma_{24} + \Gamma_{42})))\Gamma_{43}]. \tag{A.1h}$$

In Eqs. (A.1) the gammas are defined as

$$\Gamma_{31} = \left(i\Delta_4 - \frac{1}{2}\right), \tag{A.2a}$$

$$\Gamma_{32} = \left(i(\Delta_2+\Delta_4-\Delta_1) - \frac{1}{2}\right), \tag{A.2b}$$

$$\Gamma_{41} = \left(i\Delta_1 - \frac{1}{2}\right), \tag{A.2c}$$

$$\Gamma_{42} = \left(i\Delta_2 - \frac{1}{2}\right), \tag{A.2d}$$

$$\Gamma_{34} = \left(i(\Delta_4-\Delta_1) - 1\right), \tag{A.2e}$$

$$\Gamma_{12} = -\left(\gamma_{12} + i(\Delta_1-\Delta_2)\right), \tag{A.2f}$$

and the complex conjugates are $\Gamma_{13} = \Gamma_{31}^*, \Gamma_{23} = \Gamma_{32}^*, \Gamma_{14} = \Gamma_{41}^*, \Gamma_{24} = \Gamma_{42}^*, \Gamma_{43} = \Gamma_{34}^*, \Gamma_{21} = \Gamma_{12}^*$. The decoherence rate between two ground states is denoted by γ_{12}. At

VB intensities, comparable to the control field intensity, the coherences calculated in perturbation method becomes invalid. To account for the impact of high VB intensity on polarization rotation and beam propagation, the pertinent coherences are computed numerically using Gaussian elimination.

Appendix B

Appendix of chapter 3

B.1 Comparison between EIT and ARG system

In this appendix, we present a comparative analysis of four-level EIT and ARG systems. The primary distinction between these two systems is that the EIT configuration operates as an absorptive system, whereas the ARG system functions as a gaining system. In a conventional three-level EIT system, the introduction of the control field induces destructive interference among the quantum pathways at two-photon resonance, resulting in transparency for the probe beam. To augment the nonlinear effect and enhance control over dispersion and absorption, we have employed a four-level EIT system, as illustrated in Fig. B.1. To investigate the

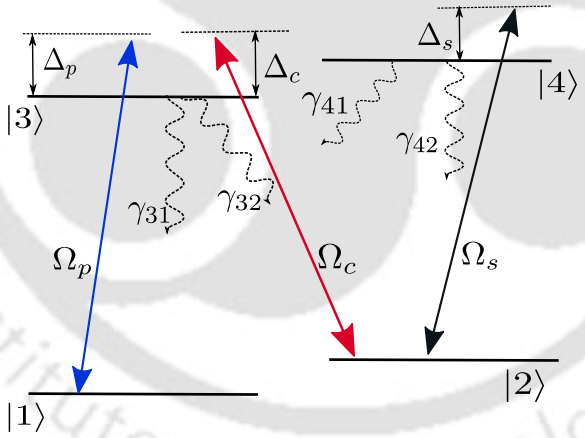

Figure B.1: Schematic diagram of a four-level EIT system. The scalar weak probe connected to $|1\rangle \leftrightarrow |3\rangle$, and a signal field to $|2\rangle \leftrightarrow |4\rangle$ transition with a strong control field coupled to $|2\rangle \leftrightarrow |3\rangle$ transition. The probe, control, and signal detunings are denoted by Δ_p, Δ_c, and Δ_s respectively. The spontaneous emission decay rate from $|3\rangle$ and $|4\rangle$ states are given by γ_{3j} and γ_{4j} $(j \in 1, 2)$.

propagation dynamics of the probe beam, it is essential to comprehend both the linear and nonlinear responses of the medium. Figures B.2(a) and B.2(b) depict the real and imaginary components of the linear and third-order Kerr nonlinear susceptibility. It is observed, $\mathrm{Im}[\chi_p^{(1)}]$ retains a positive value, indicating absorptive behavior. Nevertheless, at two-photon resonance, the discerned dip in absorption demonstrates transparency. In comparison, the ARG system, as shown in Figs. 3.2(a) and 3.2(b), exhibits linear gain as indicated by $\mathrm{Im}[\chi_p^{(1)}]$. Both systems display normal dispersion

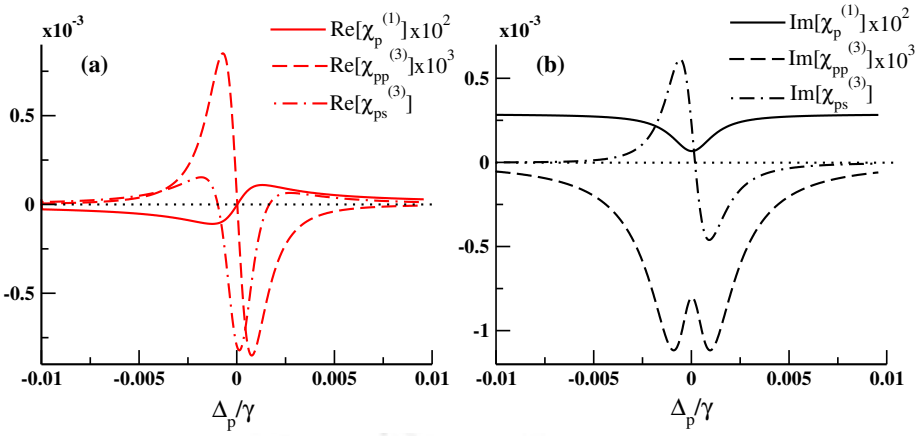

Figure B.2: Real and imaginary part of both linear and third-order nonlinear χ_{31} are plotted against the probe detuning. The control field detuning $\Delta_c = 0$. Other parameters remain same as Fig. 3.2.

characteristics in the linear regime. The $\mathrm{Im}[\chi_{pp}^{(3)}]$, reveals a gain doublet for the EIT system, while the ARG system exhibits nonlinear absorption. Notably, the nonlinear dispersion shows anomalous characteristics for both EIT and ARG systems. Our findings indicate that the self-Kerr nonlinearity is zero at two-photon resonance for both configurations. Due to the three-photon off-resonance condition, specifically denoted as $\Delta_s \neq 0$, a non-zero cross-Kerr nonlinearity has been identified in both EIT and ARG systems. However, upon examining Fig. B.2(a) alongside Fig. 3.2(a), it becomes evident that $\mathrm{Re}[\chi_{ps}^{(3)}]$ has increased by approximately 18 times in the ARG system relative to the EIT system. We present the results for the propagation of Gaussian and LG beams through the medium, considering the influence of cross-Kerr nonlinearity, as shown in Figs. B.3(a) and B.3(b). The nonlinear gain attributable to $\mathrm{Im}[\chi_{pp}^{(3)}]$ is approximately 10 times smaller than the linear gain observed in the ARG scenario at two-photon resonance. Furthermore, as previously mentioned, the non-zero refractive index at two-photon resonance, associated with $\mathrm{Re}[\chi_{ps}^{(3)}]$, is insufficient to modulate the medium's cross-Kerr refractive index adequately to focus the beam along its axis. Prior research indicates that, to effectively guide the weak

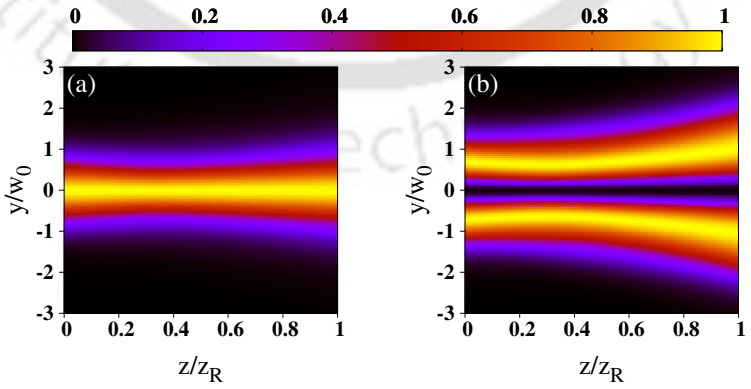

Figure B.3: Longitudinal intensity profile of (a) Gaussian, and (b) LG beam propagating inside the medium including the effect of cross-Kerr nonlinearity respectively. The probe and the control beam have a waist, $w_0 = 50\mu m$. Other parameters are same as Fig. B.2.

probe beam over several Rayleigh lengths, it is crucial to establish a suitable spatial profile for the control and signal beams to create a significant contrast in refractive index modulation within an EIT scheme [119]. Consequently, we find it beneficial to employ a four-level ARG system to investigate the characteristics of beam focusing phenomena.

Appendix C

Appendix of chapter 4

C.1 Derivation of phonon induced decay rates in variational ME

In this Appendix, we give the derivation of analytically obtained scattering rates for the phonon-mediated scattering processes. The variational ME is,

$$\frac{\partial \rho}{\partial t} = -\frac{i}{\hbar}\left[H_{SV}(t), \rho(t)\right] + \frac{\gamma}{2}\mathcal{L}\left[\sigma^{-}\right]\rho + \frac{\gamma'}{2}\mathcal{L}\left[\sigma^{+}\sigma^{-}\right]\rho + \mathcal{L}_{ph}\rho, \tag{C.1}$$

where, $\mathcal{L}_{ph}$ is given by,

$$\mathcal{L}_{ph}\rho = -\frac{1}{\hbar^2}\int_0^\infty \sum_{ij} d\tau\ \{C_{ij}(\tau)[X_i(t), X_j(t,\tau)\rho(t)] + H.c.\}. \quad (i,j \in x,y,z) \tag{C.2}$$

Here, $X_j(t,\tau) = e^{-iH_{SV}(t)\tau/\hbar}X_j(t)e^{iH_{SV}(t)\tau/\hbar}$. Now, the modified system operators are given below. Note that the time dependent field with Rabi frequency, $\Omega(t) = \Omega_D + \Omega_G e^{i\delta t}$ couples with QD system.

$$\begin{aligned} X_x(t) &= \frac{\hbar}{2}(\Omega(t)\sigma^{+} + \Omega(t)^{*}\sigma^{-}) \\ &= \frac{\hbar}{2}\{\mathrm{Re}[\Omega(t)]\sigma_x - \mathrm{Im}[\Omega(t)]\sigma_y\} \end{aligned} \tag{C.3}$$

$$\begin{aligned} X_y(t) &= \frac{i\hbar}{2}(\Omega(t)\sigma^{+} - \Omega(t)^{*}\sigma^{-}) \\ &= -\frac{\hbar}{2}\{\mathrm{Im}[\Omega(t)]\sigma_x + \mathrm{Re}[\Omega(t)]\sigma_y\}. \end{aligned} \tag{C.4}$$

$$X_z(t) = \frac{\hbar}{2}(I + \sigma_z) \tag{C.5}$$

The correlation function has already been defined in Eqs. (4.15) and Eqs. (4.17). The variational system Hamiltonian $H_{SV} = -\hbar\Delta_v|1\rangle\langle 1| + \langle B\rangle X_x(t)$. Using Born-Markov approximation, the two-time phonon system operators can be written in terms of the one-time operators in the variational picture as

$$X_x(t,\tau) = e^{-iH_{SV}(t)\tau/\hbar}X_x(t)e^{iH_{SV}(t)\tau/\hbar}, \tag{C.6}$$

$$X_y(t,\tau) = e^{-iH_{SV}(t)\tau/\hbar}X_y(t)e^{iH_{SV}(t)\tau/\hbar}, \tag{C.7}$$

$$X_z(t,\tau) = e^{-iH_{SV}(t)\tau/\hbar}X_z(t)e^{iH_{SV}(t)\tau/\hbar} \tag{C.8}$$

So, we get the following,

$$X_x(t,\tau) = \frac{\hbar}{2}\Bigg\{\left[\frac{\mathrm{Re}[\Omega(t)](\Delta_v^2\,\cos[\eta(t)\tau]+|\Omega_R(t)|^2)}{\eta(t)^2}-\frac{\mathrm{Im}[\Omega(t)](\Delta_v\,\sin[\eta(t)\tau])}{\eta(t)}\right]\sigma_x$$
$$-\left[\frac{\mathrm{Im}[\Omega(t)](\Delta_v^2\,\cos[\eta(t)\tau]+|\Omega_R(t)|^2)}{\eta(t)^2}+\frac{\mathrm{Re}[\Omega(t)](\Delta_v\,\sin[\eta(t)\tau])}{\eta(t)}\right]\sigma_y$$
$$-\frac{2\Delta_v\langle B\rangle|\Omega(t)|^2(1-\cos[\eta(t)\tau])}{\eta(t)^2}\sigma^+\sigma^-\Bigg\}, \tag{C.9}$$

$$X_y(t,\tau) = -\frac{\hbar}{2}\Bigg\{\left[\frac{\mathrm{Re}[\Omega(t)](\Delta_v\,\sin[\eta(t)\tau])}{\eta(t)}+\mathrm{Im}[\Omega(t)]\cos[\eta(t)\tau]\right]\sigma_x$$
$$+\left[\mathrm{Re}[\Omega(t)]\cos[\eta(t)\tau]-\frac{\mathrm{Im}[\Omega(t)](\Delta_v\,\sin[\eta(t)\tau])}{\eta(t)}\right]\sigma_y$$
$$+\frac{2\langle B\rangle|\Omega(t)|^2\sin[\eta(t)\tau]}{\eta(t)}\sigma^+\sigma^-\Bigg\}, \tag{C.10}$$

$$X_z(t,\tau) = \hbar\Bigg\{\left[1-\frac{|\Omega_R(t)|^2}{\eta^2}+\frac{|\Omega_R|^2\cos(\eta\tau)}{\eta^2}\right]\sigma^+\sigma^-+\left[\frac{\langle B\rangle\Delta_v\cos(\eta\tau)}{2\eta^2}-\frac{\langle B\rangle\Delta_v}{2\eta^2}\right]$$
$$\times(\Omega(t)\sigma^+ + \Omega(t)^*\sigma^-) - \frac{i\langle B\rangle\sin(\eta\tau)}{2\eta}(\Omega^*\sigma^- - \Omega\sigma^+)\Bigg\} \tag{C.11}$$

where $\eta(t) = \sqrt{\Omega_R(t)^2+\Delta_v^2}$, and $\Omega_R(t) = \langle B\rangle|\Omega(t)|$. Now from Eqn (C.2) we get

$$\mathcal{L}_{ph}\rho = -\frac{1}{\hbar^2}\int_0^\infty \{C_{xx}(\tau)[X_x(t),X_x(t,\tau)\rho(t)] + H.c. + C_{yy}(\tau)[X_y(t),X_y(t,\tau)\rho(t)]$$
$$+ H.c. + C_{zz}(\tau)[X_z(t),X_z(t,\tau)\rho(t)] + H.c. + C_{yz}(\tau)[X_z(t),X_z(t,\tau)\rho(t)]$$
$$+ H.c.\}\,d\tau. \tag{C.12}$$

We first solve for polaron theory by putting the values of $X_x(t,\tau)$ and $X_y(t,\tau)$ and then for the weak-coupling and cross-coupling case considering the $X_z(t,\tau)$ term. The following definition of real parameters are used.

$$f(t,\tau) = \frac{\Delta^2\,\cos[\eta(t)\tau]+|\Omega_R(t)|^2}{\eta(t)^2}, \tag{C.13}$$

$$g(t,\tau) = \frac{\Delta\,\sin[\eta(t)\tau]}{\eta(t)}, \tag{C.14}$$

$$h(t,\tau) = \frac{2\Delta\langle B\rangle|\Omega(t)|(1-\cos[\eta(t)\tau])}{\eta(t)^2}, \tag{C.15}$$

$$q(t,\tau) = \cos[\eta(t)\tau], \tag{C.16}$$

$$r(t,\tau) = \frac{2\langle B\rangle|\Omega(t)|^2\,\sin[\eta(t)\tau]}{\eta(t)}, \tag{C.17}$$

$$m(t,\tau) = \frac{\eta(t)^2-|\Omega_R|^2+|\Omega_R|^2\cos(\eta(t)\tau)}{\eta(t)^2}, \tag{C.18}$$

$$n(t,\tau) = \frac{\langle B\rangle\Delta_v}{2\eta(t)^2}\left\{\cos(\eta(t)\tau)-1\right\}, \tag{C.19}$$

$$u(t,\tau) = \frac{\langle B\rangle}{2\eta(t)}\sin(\eta(t)\tau). \tag{C.20}$$

For the polaron theory we get

$$\begin{aligned}\mathcal{L}_{ph}^{polaron}\rho =& -\frac{1}{\hbar^2}\int_0^\infty \{C_{xx}(\tau)[X_x(t),X_x(t,\tau)\rho(t)] + H.c. + C_{yy}(\tau)[X_y(t),X_y(t,\tau)\rho(t)] \\ &+ H.c.\}d\tau \\ =& -\frac{1}{4}\int_0^\infty \Bigg\{G_g(\tau)\Bigg[(\mathrm{Re}[\Omega(t)]\sigma_x - \mathrm{Im}[\Omega(t)]\sigma_y),\Bigg((\mathrm{Re}[\Omega(t)]f(t,\tau) - \mathrm{Im}[\Omega(t)] \\ &\times g(t,\tau))\sigma_x - (\mathrm{Im}[\Omega(t)]f(t,\tau) + \mathrm{Re}[\Omega(t)]g(t,\tau))\sigma_y - h(t,\tau)\sigma^+\sigma^-\Bigg)\rho(t)\Bigg] \\ &+ \ H.c. + G_u(\tau)\Bigg[(\mathrm{Im}[\Omega(t)]\sigma_x + \mathrm{Re}[\Omega(t)]\sigma_y), -\Bigg((\mathrm{Re}[\Omega(t)]g(t,\tau) + \mathrm{Im}[\Omega(t)] \\ &\times q(t,\tau))\sigma_x + (\mathrm{Re}[\Omega(t)]q(t,\tau) - \mathrm{Im}[\Omega(t)]g(t,\tau))\sigma_y + r(t,\tau)\sigma^+\sigma^-\Bigg)\rho(t)\Bigg] \\ &+ \ H.c.\Bigg\}\,d\tau. \end{aligned} \tag{C.21}$$

$$\begin{aligned}\mathcal{L}_{ph}^{polaron}\rho =& \frac{\Gamma^{\sigma^+}}{2}\mathcal{L}[\sigma^+]\rho + \frac{\Gamma^{\sigma^-}}{2}\mathcal{L}[\sigma^-]\rho - \Gamma^{cd}(\sigma^+\rho\sigma^+ + \sigma^-\rho\sigma^-) - i\Gamma^{sd}(\sigma^+\rho\sigma^+ - \sigma^-\rho\sigma^-) \\ &+ i\Delta^{\sigma^+\sigma^-}[\sigma^+\sigma^-,\rho] - [i\Gamma_{gu+}(\sigma^+\sigma^-\rho\sigma^+ + \sigma^-\rho - \sigma^+\sigma^-\rho\sigma^-) + H.c.] \\ &- [\Gamma_{gu-}(\sigma^+\sigma^-\rho\sigma^+ - \sigma^-\rho + \sigma^+\sigma^-\rho\sigma^-) + H.c.], \end{aligned} \tag{C.22}$$

where all the phonon-mediated scattering rates which contributes to the polaron case are

$$\begin{aligned}\Gamma^{\sigma^+} =& -\frac{|\Omega(t)|^2}{2}\int_0^\infty (-\mathrm{Re}[G_g(\tau)]f(t,\tau) + \mathrm{Im}[G_g(\tau) + G_u(\tau)]g(t,\tau) - \mathrm{Re}[G_u(\tau)] \\ &\times q(t,\tau))\ d\tau \\ =& \frac{|\Omega_R(t)|^2}{2}\int_0^\infty \Bigg(\mathrm{Re}\Bigg\{\{\cosh[\phi(\tau)] - 1\}\Bigg\{\frac{\Delta^2\cos[\eta(t)\tau] + |\Omega_R(t)|^2}{\eta(t)^2}\Bigg\} + \sinh[\phi(\tau)] \\ &\times \cos[\eta(t)\tau]\Bigg\} - \mathrm{Im}[e^{\phi(\tau)} - 1]\Bigg\{\frac{\Delta\sin[\eta(t)\tau]}{\eta(t)}\Bigg\}\Bigg)\,d\tau, \end{aligned} \tag{C.23}$$

$$\begin{aligned}\Gamma^{\sigma^-} =& -\frac{|\Omega(t)|^2}{2}\int_0^\infty (-\mathrm{Re}[G_g(\tau)]f(t,\tau) - \mathrm{Im}[G_g(\tau) + G_u(\tau)]g(t,\tau) - \mathrm{Re}[G_u(\tau)] \\ &\times q(t,\tau))\ d\tau \\ =& \frac{|\Omega_R(t)|^2}{2}\int_0^\infty \Bigg(\mathrm{Re}\Bigg\{\{\cosh[\phi(\tau)] - 1\}\Bigg\{\frac{\Delta^2\cos[\eta(t)\tau] + |\Omega_R(t)|^2}{\eta(t)^2}\Bigg\} + \sinh[\phi(\tau)] \\ &\times \cos[\eta(t)\tau]\Bigg\} + \mathrm{Im}[e^{\phi(\tau)} - 1]\Bigg\{\frac{\Delta\sin[\eta(t)\tau]}{\eta(t)}\Bigg\}\Bigg)\,d\tau, \end{aligned} \tag{C.24}$$

$$\begin{aligned}\Gamma^{cd} =& \frac{1}{2}\int_0^\infty ((\mathrm{Re}[G_u(\tau)](\tau)q(t,\tau) - \mathrm{Re}[G_g(\tau)]f(t,\tau))(\mathrm{Re}[\Omega(t)^2] - \mathrm{Im}[\Omega(t)^2]) \\ &- 2\mathrm{Re}[\Omega(t)]\mathrm{Im}[\Omega(t)](\mathrm{Re}[G_u(\tau)] - \mathrm{Re}[G_g(\tau)])g(t,\tau))\ d\tau \\ =& \frac{1}{2}\int_0^\infty \langle B\rangle^2\Bigg(\mathrm{Re}\Bigg\{\sinh[\phi(\tau)]\cos[\eta(t)\tau] - \{\cosh[\phi(\tau)] - 1\} \\ &\times \Bigg\{\frac{\Delta^2\cos[\eta(t)\tau] + |\Omega_R(t)|^2}{\eta(t)^2}\Bigg\}\Bigg\}(\mathrm{Re}[\Omega(t)^2] - \mathrm{Im}[\Omega(t)^2]) - 2\mathrm{Re}[\Omega]\mathrm{Im}[\Omega] \\ &\times \mathrm{Re}[1 - e^{-\phi(\tau)}]\Bigg\{\frac{\Delta\sin[\eta(t)\tau]}{\eta(t)}\Bigg\}\Bigg)\,d\tau, \end{aligned} \tag{C.25}$$

$$\Gamma^{sd} = \frac{1}{2}\int_0^\infty ((\mathrm{Re}[G_u(\tau)] - \mathrm{Re}[G_g(\tau)])g(t,\tau)(\mathrm{Re}[\Omega(t)^2] - \mathrm{Im}[\Omega(t)^2]) + 2\mathrm{Re}[\Omega(t)]$$
$$\times \mathrm{Im}[\Omega(t)](\mathrm{Re}[G_u(\tau)]q(t,\tau) - \mathrm{Re}[G_g(\tau)]g(t,\tau)))\ d\tau$$
$$= \frac{1}{2}\int_0^\infty \langle B\rangle^2 \Bigg(\mathrm{Re}[1 - e^{-\phi(\tau)}]\Bigg\{\frac{\Delta\ \sin[\eta(t)\tau]}{\eta(t)}\Bigg\}(\mathrm{Re}[\Omega(t)^2] - \mathrm{Im}[\Omega(t)^2]) + 2\mathrm{Re}[\Omega(t)]$$
$$\times \mathrm{Im}[\Omega(t)]\mathrm{Re}\Bigg\{\sinh[\phi(\tau)]\cos[\eta(t)\tau] - \{\cosh[\phi(\tau)] - 1\}$$
$$\times \Bigg\{\frac{\Delta^2\ \cos[\eta(t)\tau] + |\Omega_R|^2}{\eta(t)^2}\Bigg\}\Bigg\}\Bigg)\ d\tau, \tag{C.26}$$

$$\Delta^{\sigma^+\sigma^-} = \frac{|\Omega_R(t)|^2}{2}\int_0^\infty \mathrm{Re}([G_g(\tau)] + G_u(\tau))g(t,\tau)\ d\tau$$
$$= \frac{|\Omega_R(t)|^2}{2}\int_0^\infty \mathrm{Re}[e^{\phi(\tau)} - 1]\Bigg(\frac{\Delta\ \sin[\eta(t)\tau]}{\eta(t)}\Bigg)\ d\tau, \tag{C.27}$$

$$\Gamma_{gu+} = \frac{1}{4}\int_0^\infty (\mathrm{Im}[\Omega(t)]G_g(\tau)h(t,\tau) + \mathrm{Re}[\Omega(t)]G_u(\tau)r(t,\tau))\ d\tau$$
$$= \frac{1}{4}\int_0^\infty \Bigg(\mathrm{Im}[\Omega(t)]\{\cosh[\phi(t)\tau] - 1\}\Bigg\{\frac{2\Delta\langle B\rangle|\Omega(t)|^2(1 - \cos[\eta(t)\tau])}{\eta(t)^2}\Bigg\} + \mathrm{Re}[\Omega(t)]$$
$$\times \sinh[\phi(\tau)]\Bigg\{\frac{2\langle B\rangle|\Omega(t)|^2\sin[\eta(t)\tau]}{\eta(t)}\Bigg\}\Bigg)\ d\tau, \tag{C.28}$$

$$\Gamma_{gu-} = \frac{1}{4}\int_0^\infty (\mathrm{Re}[\Omega(t)]G_g(\tau)h(t,\tau) - \mathrm{Im}[\Omega(t)]G_u(\tau)r(t,\tau))\ d\tau$$
$$= \frac{1}{4}\int_0^\infty \Bigg(\mathrm{Re}[\Omega(t)]\{\cosh[\phi(t)\tau] - 1\}\Bigg\{\frac{2\Delta\langle B\rangle|\Omega(t)|^2(1 - \cos[\eta(t)\tau])}{\eta(t)^2}\Bigg\} - \mathrm{Im}[\Omega(t)]$$
$$\times \sinh[\phi(\tau)]\Bigg\{\frac{2\langle B\rangle|\Omega(t)|^2\sin[\eta(t)\tau]}{\eta(t)}\Bigg\}\Bigg)\ d\tau. \tag{C.29}$$

For the weak-coupling case the decay rates are

$$\mathcal{L}_{ph}^{weak}\rho = -\int_0^\infty \Big\{\mathrm{Re}[C_{zz}](\sigma^+\sigma^-\rho + \rho\sigma^+\sigma^- - 2\sigma^+\sigma^-\rho\sigma^+\sigma^-)m(t,\tau) + i\mathrm{Im}[C_{zz}](\sigma^+\sigma^-\rho$$
$$- \rho\sigma^+\sigma^-)m(t,\tau) + \mathrm{Re}[C_{zz}]\Big[(\Omega\sigma^+\rho - \Omega\sigma^+\rho\sigma^+\sigma^- - \Omega^*\sigma^-\rho\sigma^+\sigma^-) + H.c.\Big]$$
$$\times n(t,\tau) + i\mathrm{Im}[C_{zz}]\Big[(\Omega\sigma^+\rho - \Omega\sigma^+\rho\sigma^+\sigma^- - \Omega^*\sigma^-\rho\sigma^+\sigma^-) - H.c.\Big]n(t,\tau)$$
$$+ i\mathrm{Re}[C_{zz}]\Big[\big(\Omega\sigma^+\rho - \Omega\sigma^+\rho\sigma^+\sigma^- + \Omega^*\sigma^-\rho\sigma^+\sigma^-\big) - H.c.\Big]u(t,\tau)$$
$$- \mathrm{Im}[C_{zz}]\Big[\big(\Omega\sigma^+\rho - \Omega\sigma^+\rho\sigma^+\sigma^- + \Omega^*\sigma^-\rho\sigma^+\sigma^-\big) + H.c.\Big]u(t,\tau)\Big\}d\tau, \tag{C.30}$$

and finally for the cross coupling we get

$$\mathcal{L}_{ph}^{cross}\rho = --\frac{1}{2}\int_0^\infty \Big\{i\mathrm{Re}[C_{yz}]\Big[\big(\Omega^*\sigma^-\rho - \Omega^*\sigma^+\sigma^-\rho\sigma^- + \Omega\sigma^+\sigma^-\rho\sigma^+\big) - H.c.\Big]m(t,\tau)$$
$$- \mathrm{Im}[C_{yz}]\Big[(\Omega^*\sigma^-\rho - \Omega^*\sigma^+\sigma^-\rho\sigma^- + \Omega\sigma^+\sigma^-\rho\sigma^+) + H.c.\Big]m(t,\tau) + i\mathrm{Re}[C_{yz}]$$
$$\times \Big[\big(|\Omega|^2\sigma^-\sigma^+\rho - |\Omega|^2\sigma^+\sigma^-\rho\big) - H.c.\Big]n(t,\tau) - \mathrm{Im}[C_{yz}]\Big[(|\Omega|^2\sigma^-\sigma^+\rho$$
$$- |\Omega|^2\sigma^+\sigma^-\rho) + H.c.\Big]n(t,\tau) + i\mathrm{Re}[C_{yz}](-2(\Omega^*)^2\sigma^-\rho\sigma^- + 2\Omega^2\sigma^+\rho\sigma^+)n(t,\tau)$$

$$+ \mathrm{Im}[C_{yz}]\left(2|\Omega|^2\sigma^+\rho\sigma^- - 2|\Omega|^2\sigma^-\rho\sigma^+\right) n(t,\tau) + \mathrm{Re}[C_{yz}]\Big[(-|\Omega|^2\sigma^-\sigma^+\rho$$
$$- |\Omega|^2\sigma^+\sigma^-\rho) + H.c.\Big] u(t,\tau) + i\mathrm{Im}[C_z]\Big[\left(-|\Omega|^2\sigma^-\sigma^+\rho - |\Omega|^2\sigma^+\sigma^-\rho\right) - H.c.\Big]$$
$$\times u(t,\tau) + \mathrm{Re}[C_{yz}](-2(\Omega^*)^2\sigma^-\rho\sigma^+ + 2|\Omega|^2\sigma^-\rho\sigma^+ + 2|\Omega|^2\sigma^+\rho\sigma^-$$
$$- 2\Omega^2\sigma^+\rho\sigma^+)u(t,\tau)\Big\}d\tau. \tag{C.31}$$

The above phonon-induced scattering rates are function of time. At each time t the values are calculated by integrating with respect to τ. These analytically derived scattering rates illustrate the physical picture of electron-phonon coupling in semiconductor QDs.

TH-3976_186121017

Bibliography

[1] G. Vicidomini, P. Bianchini, and A. Diaspro, Nature methods **15**, 173 (2018).

[2] B. Hao and J. Leger, Opt. Express **15**, 3550 (2007).

[3] M. S. Zubairy, A very brief history of light, in *Optics in our time*, pp. 3–24, Springer International Publishing Cham, 2016.

[4] N. Voudoukis and S. Oikonomidis, European Journal of Engineering and Technology Research **2**, 23 (2017).

[5] S. Dupré, Synthese **185**, 501 (2012).

[6] C. A. Cardona Suárez and J. Gutiérrez Valderrama, Archive for History of Exact Sciences **74**, 45 (2020).

[7] F. Bryant, Physics Bulletin **9**, 317 (1958).

[8] C. G. Parazzoli, R. B. Greegor, K. Li, B. E. C. Koltenbah, and M. Tanielian, Phys. Rev. Lett. **90**, 107401 (2003).

[9] B. B. Baker and E. T. Copson *The mathematical theory of Huygens' principle* Vol. 329 (American Mathematical Soc., 2003).

[10] J. J. Thomson, *The corpuscular theory of matter* (A. Constable & Company, Limited, 1907).

[11] T. Young, Philosophical transactions of the Royal Society of London , 1 (1804).

[12] O. Carnal and J. Mlynek, Phys. Rev. Lett. **66**, 2689 (1991).

[13] J. C. Maxwell *The Scientific Letters and Papers of James Clerk Maxwell: Volume 1, 1846-1862* Vol. 1 (CUP Archive, 1990).

[14] R. Flood, M. McCartney, and A. Whitaker, *James Clerk Maxwell: perspectives on his life and work* (OUP Oxford, 2014).

[15] M. Planck, Entropie **144**, 164 (1900).

[16] A. B. Arons and M. B. Peppard, American Journal of Physics **33**, 367 (1965).

[17] A. Einstein, Annalen der physik **4** (1905).

[18] P. A. M. Dirac, Proceedings of the Royal Society of London. Series A, Containing Papers of a Mathematical and Physical Character **133**, 60 (1931), Full publication date: Sep. 1, 1931.

[19] R. P. Feynman, Space-time approach to quantum electrodynamics, in *Quantum electrodynamics*, pp. 178–198, CRC Press, 2018.

[20] J. Schwinger, Phys. Rev. **115**, 721 (1959).

[21] T. H. MAIMAN, Nature **187**, 493 (1960).

[22] E. Arimondo and G. Orriols, Nuovo Cimento Lettere **17**, 333 (1976).

[23] S. E. Harris, J. E. Field, and A. Imamoğlu, Phys. Rev. Lett. **64**, 1107 (1990).

[24] I. I. Rabi, Phys. Rev. **51**, 652 (1937).

[25] D. F. Walls, Nature **306**, 141 (1983).

[26] R. J. Glauber, Phys. Rev. **130**, 2529 (1963).

[27] S. Haroche, Rev. Mod. Phys. **85**, 1083 (2013).

[28] L. Labonté *et al.*, PRX Quantum **5**, 010101 (2024).

[29] S. Zhou, M. Zhang, J. Preskill, and L. Jiang, Nature Communications **9**, 78 (2018).

[30] M. O. Scully and M. S. Zubairy, *Quantum optics* (Cambridge university press, 1997).

[31] J. D. Jackson, *Classical electrodynamics* (John Wiley & Sons, 2021).

[32] R. W. Boyd, *Nonlinear Optics*, 3 ed. (Academic Press, Burlington, 2008).

[33] P. Weinberger, Philosophical Magazine Letters **88**, 897 (2008).

[34] S. Rebić *et al.*, Phys. Rev. A **70**, 032317 (2004).

[35] R. W. Boyd, M. G. Raymer, P. Narum, and D. J. Harter, Phys. Rev. A **24**, 411 (1981).

[36] R. W. Boyd, S. G. Lukishova, and Y. R. Shen*Self-focusing: Past and present: Fundamentals and prospects* Vol. 114 (Springer, 2009).

[37] D. J. Griffiths, *Introduction to electrodynamics* (Cambridge University Press, 2023).

[38] A. M. Fox*Quantum optics: an introduction* Vol. 15 (Oxford university press, 2006).

[39] C. C. Gerry and P. L. Knight, *Introductory quantum optics* (Cambridge university press, 2023).

[40] K. Blum*Density matrix theory and applications* Vol. 64 (Springer Science & Business Media, 2012).

[41] H.-P. Breuer and F. Petruccione, *The theory of open quantum systems* (OUP Oxford, 2002).

[42] M. H. Anderson, J. R. Ensher, M. R. Matthews, C. E. Wieman, and E. A. Cornell, Science **269**, 198 (1995), Full publication date: Jul. 14, 1995.

[43] M. Liu *et al.*, Nature Electronics **4**, 548 (2021).

[44] B. J. Riel, American Journal of Physics **76**, 750 (2008).

[45] S. J. Angus, A. J. Ferguson, A. S. Dzurak, and R. G. Clark, Nano Letters **7**, 2051 (2007).

[46] G. D. Mahan, *Many-particle physics* (Springer Science & Business Media, 2013).

[47] C. Kittel and P. McEuen, *Introduction to solid state physics* (John Wiley & Sons, 2018).

[48] T.-H. Liu, J. Zhou, B. Liao, D. J. Singh, and G. Chen, Phys. Rev. B **95**, 075206 (2017).

[49] A. Nazir and D. P. S. McCutcheon, Journal of Physics: Condensed Matter **28**, 103002 (2016).

[50] L. Allen and J. H. Eberly, *Optical resonance and two-level atoms* (Courier Corporation, 2012).

[51] P. Meystre and M. Sargent, *Elements of quantum optics* (Springer Science & Business Media, 2007).

[52] J. B. Lambert, E. P. Mazzola, and C. D. Ridge, *Nuclear magnetic resonance spectroscopy: an introduction to principles, applications, and experimental methods* (John Wiley & Sons, 2019).

[53] S. Haroche and F. Hartmann, Physical Review A **6**, 1280 (1972).

[54] B. Couillaud and A. Ducasse, Phys. Rev. Lett. **35**, 1276 (1975).

[55] A. V. Turukhin *et al.*, Phys. Rev. Lett. **88**, 023602 (2001).

[56] G. S. Agarwal and T. N. Dey, Phys. Rev. A **68**, 063816 (2003).

[57] D. F. Phillips, A. Fleischhauer, A. Mair, R. L. Walsworth, and M. D. Lukin, Phys. Rev. Lett. **86**, 783 (2001).

[58] C. L. Holloway *et al.*, Journal of Applied Physics **121**, 233106 (2017).

[59] L. Ma, O. Slattery, and X. Tang, Journal of Optics **19**, 043001 (2017).

[60] G. Alzetta, L. Moi, and G. Orriols, Il Nuovo Cimento B (1971-1996) **52**, 209 (1979).

[61] J. F. Bille, *High resolution imaging in microscopy and ophthalmology: new frontiers in biomedical optics* (Springer, 2019).

[62] E. Abbe, Archiv für Mikroskopische Anatomie **9**, 413 (1873).

[63] S. W. Hell, Nature Biotechnology **21**, 1347 (2003).

[64] R. Marchand *et al.*, Phys. Rev. Appl. **16**, 014008 (2021).

[65] W. Chao, B. D. Harteneck, J. A. Liddle, E. H. Anderson, and D. T. Attwood, Nature **435**, 1210 (2005).

[66] M. Schrader and S. W. Hell, Journal of Microscopy **183**, 110 (1996).

[67] S. W. Hell and J. Wichmann, Opt. Lett. **19**, 780 (1994).

[68] T. A. Klar, S. Jakobs, M. Dyba, A. Egner, and S. W. Hell, Proceedings of the National Academy of Sciences **97**, 8206 (2000).

[69] M. Hofmann, C. Eggeling, S. Jakobs, and S. W. Hell, Proceedings of the National Academy of Sciences **102**, 17565 (2005).

[70] E. Betzig *et al.*, Science **313**, 1642 (2006).

[71] M. J. Rust, M. Bates, and X. Zhuang, Nature Methods **3**, 793 (2006).

[72] M. Saxena, G. Eluru, and S. S. Gorthi, Adv. Opt. Photon. **7**, 241 (2015).

[73] F. Balzarotti *et al.*, Science **355**, 606 (2017).

[74] E. Hecht, *Optics* (Pearson Education India, 2012).

[75] V. Westphal and S. W. Hell, Phys. Rev. Lett. **94**, 143903 (2005).

[76] Y. Kozawa and S. Sato, Progress in Optics **66**, 35 (2021).

[77] D. Luo *et al.*, Journal of Optics **22**, 115612 (2020).

[78] A. M. Beckley, T. G. Brown, and M. A. Alonso, Opt. Express **18**, 10777 (2010).

[79] Q. Zhan, Adv. Opt. Photon. **1**, 1 (2009).

[80] X. Yang *et al.*, Opt. Express **27**, 3900 (2019).

[81] T. Grosjean, D. Courjon, and M. Spajer, Optics Communications **203**, 1 (2002).

[82] S. Ramachandran, P. Kristensen, and M. F. Yan, Opt. Lett. **34**, 2525 (2009).

[83] C. Maurer, A. Jesacher, S. Fürhapter, S. Bernet, and M. Ritsch-Marte, New Journal of Physics **9**, 78 (2007).

[84] Z. Chen, T. Zeng, B. Qian, and J. Ding, Opt. Express **23**, 17701 (2015).

[85] Ruchi, P. Senthilkumaran, and S. K. Pal, International Journal of Optics **2020**, 2812803 (2020).

[86] P. Kumar, S. K. Pal, N. K. Nishchal, and P. Senthilkumaran, J. Opt. Soc. Am. A **37**, 1043 (2020).

[87] E. Allahyari *et al.*, Applied Physics Letters **112**, 211103 (2018).

[88] M. Liu *et al.*, Nanophotonics **11**, 3395 (2022).

[89] A. La Porta and M. D. Wang, Phys. Rev. Lett. **92**, 190801 (2004).

[90] A. K. Dubey and V. Yadava, International Journal of Machine Tools and Manufacture **48**, 609 (2008).

[91] F. Castellucci, T. W. Clark, A. Selyem, J. Wang, and S. Franke-Arnold, Phys. Rev. Lett. **127**, 233202 (2021).

[92] F. Bouchard *et al.*, Phys. Rev. Lett. **117**, 233903 (2016).

[93] M. Fleischhauer and M. D. Lukin, Phys. Rev. A **65**, 022314 (2002).

[94] J. Durnin, J. Opt. Soc. Am. A **4**, 651 (1987).

[95] W. L. Erikson and S. Singh, Phys. Rev. E **49**, 5778 (1994).

[96] O. Korotkova, B. G. Hoover, V. L. Gamiz, and E. Wolf, J. Opt. Soc. Am. A **22**, 2547 (2005).

[97] D. Deng, H. Yu, S. Xu, J. Shao, and Z. Fan, Optics Communications **281**, 202 (2008).

[98] Z. Ficek and S. Swain*Quantum interference and coherence: theory and experiments* Vol. 100 (Springer Science & Business Media, 2005).

[99] M. Kiffner, J. Evers, and C. H. Keitel, Phys. Rev. A **73**, 063814 (2006).

[100] J. C. Delagnes and M. A. Bouchene, Phys. Rev. Lett. **98**, 053602 (2007).

[101] F. A. Hashmi and M. A. Bouchene, Phys. Rev. A **77**, 051803(R) (2008).

[102] L. Jin, Y. Niu, and S. Gong, Phys. Rev. A **83**, 023410 (2011).

[103] F. A. Hashmi and M. A. Bouchene, Phys. Rev. Lett. **101**, 213601 (2008).

[104] J. Wu, X.-Y. Lü, and L.-L. Zheng, J. Phys. B: At., Mol. Opt. Phys. **43**, 161003 (2010).

[105] Z. Zhu *et al.*, Phys. Rev. A **94**, 013826 (2016).

[106] A. Kani and H. Wanare, Europhysics Letters **120**, 33001 (2018).

[107] N. Daloi and T. N. Dey, Opt. Express **30**, 21894 (2022).

[108] N. A. Proite, B. E. Unks, J. T. Green, and D. D. Yavuz, Phys. Rev. A **77**, 023819 (2008).

[109] C. J. Zhu, L. Deng, E. W. Hagley, and G. X. Huang, Laser Physics **24**, 065402 (2014).

[110] L. Wang *et al.*, Optics Communications **441**, 190 (2019).

[111] R. Morandotti, H. S. Eisenberg, Y. Silberberg, M. Sorel, and J. S. Aitchison, Phys. Rev. Lett. **86**, 3296 (2001).

[112] G. S. Agarwal and T. N. Dey, Laser & Photonics Reviews **3**, 287 (2009).

[113] A. Vafafard and M. Sahrai, J. Opt. Soc. Am. B **35**, 2118 (2018).

[114] V. Kudriašov *et al.*, Opt. Express **33**, 40931 (2025).

[115] S. P. Tewari and G. S. Agarwal, Phys. Rev. Lett. **56**, 1811 (1986).

[116] H. Schmidt and A. Imamoglu, Opt. Lett. **21**, 1936 (1996).

[117] D. D. Yavuz and D. E. Sikes, Phys. Rev. A **81**, 035804 (2010).

[118] T. N. Dey and G. S. Agarwal, Phys. Rev. A **76**, 015802 (2007).

[119] S. Sharma and T. N. Dey, Phys. Rev. A **96**, 053813 (2017).

[120] Y. Shen, Progress in Quantum Electronics **4**, 1 (1975).

[121] J. Marburger, Progress in Quantum Electronics **4**, 35 (1975).

[122] G. Askaryan, Sov. Phys. JETP **15**, 943 (1962).

[123] R. Y. Chiao, E. Garmire, and C. H. Townes, Phys. Rev. Lett. **13**, 479 (1964).

[124] P. L. Kelley, Phys. Rev. Lett. **15**, 1005 (1965).

[125] P. Lallemand and N. Bloembergen, Phys. Rev. Lett. **15**, 1010 (1965).

[126] E. Garmire, R. Y. Chiao, and C. H. Townes, Phys. Rev. Lett. **16**, 347 (1966).

[127] S. N. Vlasov, V. A. Petrishchev, and V. I. Talanov, Radiophysics and Quantum Electronics **14**, 1062 (1971).

[128] A. Y. Wong and P. Y. Cheung, Phys. Rev. Lett. **52**, 1222 (1984).

[129] P. Panagiotopoulos *et al.*, Phys. Rev. A **93**, 033808 (2016).

[130] C. Eigen *et al.*, Phys. Rev. X **6**, 041058 (2016).

[131] Y. Cho, Phys. Rev. E **98**, 012213 (2018).

[132] S. Vitale, Science **372**, eabc7397 (2021).

[133] V. Sautenkov *et al.*, Optics Communications **431**, 131 (2019).

[134] Y. Wang, *Nonlinear self-focusing in cold Cesium atoms* (The University of Wisconsin-Madison, 2005).

[135] M. H. Helle, T. G. Jones, J. R. Peñano, D. Kaganovich, and A. Ting, Applied Physics Letters **103**, 121101 (2013).

[136] B. Hafizi *et al.*, Opt. Lett. **40**, 1556 (2015).

[137] S. Kumar Orappanpara Soman, Journal of Optics **23**, 123502 (2021).

[138] M. Fleischhauer, A. Imamoglu, and J. P. Marangos, Rev. Mod. Phys. **77**, 633 (2005).

[139] Y. Qi, F. Zhou, T. Huang, Y. Niu, and S. Gong, Phys. Rev. A **84**, 023814 (2011).

[140] Z. Bai, W. Li, and G. Huang, Optica **6**, 309 (2019).

[141] M. Chen, S. Zeng, D. Lu, W. Hu, and Q. Guo, Phys. Rev. E **98**, 022211 (2018).

[142] X. Zhu, S. Cao, J. Xie, Y. Qiu, and Y. He, J. Opt. Soc. Am. B **37**, 3041 (2020).

[143] P. Li, B. A. Malomed, and D. Mihalache, Opt. Express **28**, 34472 (2020).

[144] H. R. Hamedi and G. Juzeliūnas, Phys. Rev. A **91**, 053823 (2015).

[145] H. R. Hamedi, A. H. Gharamaleki, and M. Sahrai, Appl. Opt. **55**, 5892 (2016).

[146] R. Mukherjee, S. Konar, and P. Mishra, Phys. Rev. A **103**, 033517 (2021).

[147] R. Mukherjee and S. Konar, Results in Physics **17**, 103090 (2020).

[148] Z. Bai and G. Huang, Opt. Express **24**, 4442 (2016).

[149] P. Bienias and H. P. Büchler, New Journal of Physics **18**, 123026 (2016).

[150] Y. Chen, Z. Bai, C. Hang, and G. Huang, Opt. Express **31**, 33518 (2023).

[151] Y. Mu, L. Qin, Z. Shi, and G. Huang, Phys. Rev. A **103**, 043709 (2021).

[152] Y. Wu and L. Deng, Phys. Rev. Lett. **93**, 143904 (2004).

[153] C. Hang, G. Huang, and L. Deng, Phys. Rev. E **73**, 036607 (2006).

[154] C. Hang and G. Huang, Opt. Express **18**, 2952 (2010).

[155] U. Khan, B. Amin, K. Ullah, and A. Ullah, Physics Letters A **383**, 125998 (2019).

[156] L. Deng and M. G. Payne, Phys. Rev. Lett. **98**, 253902 (2007).

[157] A. J and B. T, Physica Scripta **97**, 085103 (2022).

[158] T. T. Simpson *et al.*, Opt. Express **30**, 9878 (2022).

[159] H. Rahman *et al.*, Results in Physics **53**, 107024 (2023).

[160] B. Wen *et al.*, Opt. Express **27**, 13845 (2019).

[161] B. Wen, G. Rui, J. He, Y. Cui, and B. Gu, Journal of Optics **22**, 085501 (2020).

[162] Y. Zhang *et al.*, Nano Letters **18**, 5538 (2018).

[163] L. Huang *et al.*, Nanophotonics **9**, 4315 (2020).

[164] Y. She, X. Zheng, D. Wang, and W. Zhang, Opt. Express **21**, 17392 (2013).

[165] H. R. Hamedi, Journal of Applied Physics **119**, 183104 (2016).

[166] D. Wang, Laser Physics Letters **19**, 095207 (2022).

[167] A. Nazir, Phys. Rev. B **78**, 153309 (2008).

[168] B. Krummheuer, V. M. Axt, and T. Kuhn, Phys. Rev. B **65**, 195313 (2002).

[169] A. Vagov, V. M. Axt, and T. Kuhn, Phys. Rev. B **66**, 165312 (2002).

[170] A. Grodecka, C. Weber, P. Machnikowski, and A. Knorr, Phys. Rev. B **76**, 205305 (2007).

[171] Q. Glorieux, T. Aladjidi, P. D. Lett, and R. Kaiser, New Journal of Physics **25**, 051201 (2023).

[172] M. Heuck, K. Jacobs, and D. R. Englund, Phys. Rev. A **101**, 042322 (2020).

[173] F. Lu *et al.*, Sensors **18** (2018).

[174] L. Meng, M. Sun, J. Chen, and Z. Yang, Scientific Reports **6**, 19558 (2016).

[175] Y. Xiang, S. Bai, and Z. Zhang, Optics & Laser Technology **160**, 109079 (2023).

[176] M. Baliyan and N. K. Nishchal, Journal of Optics **25**, 095702 (2023).

[177] E. Melnikova *et al.*, Optics Communications **522**, 128661 (2022).

[178] H. Köhler, Opt. Acta **28**, 1691 (1981).

[179] S. W. Hell, Science **316**, 1153 (2007).

[180] T. Müller, C. Schumann, and A. Kraegeloh, ChemPhysChem **13**, 1986 (2012).

[181] S. Weisenburger and V. Sandoghdar, Contemporary Physics **56**, 123 (2015).

[182] T. Kaldewey *et al.*, Nature Photonics **12**, 68 (2018).

[183] D. Goswami, Physics Reports **374**, 385 (2003).

[184] V. Malinovsky and J. Krause, Eur. Phys. J. D **14**, 147 (2001).

[185] F. Kappe *et al.*, Advanced Quantum Technologies **8**, 2300352 (2025).

[186] J. S. Melinger, S. R. Gandhi, A. Hariharan, D. Goswami, and W. S. Warren, The Journal of Chemical Physics **101**, 6439 (1994).

[187] E. R. Schmidgall, P. R. Eastham, and R. T. Phillips, Phys. Rev. B **81**, 195306 (2010).

[188] S. Herbers, Y. M. Caris, S. E. J. Kuijpers, J.-U. Grabow, and S. Y. T. van de Meerakker, Molecular Physics , e2129105 (2022).

[189] A. Ramachandran, J. Fraser-Leach, S. O'Neal, D. G. Deppe, and K. C. Hall, Opt. Express **29**, 41766 (2021).

[190] A. J. Ramsay *et al.*, Phys. Rev. Lett. **104**, 017402 (2010).

[191] A. J. Ramsay *et al.*, Phys. Rev. Lett. **105**, 177402 (2010).

[192] P. Machnikowski and L. Jacak, Phys. Rev. B **69**, 193302 (2004).

[193] A. Krügel, V. M. Axt, T. Kuhn, P. Machnikowski, and A. Vagov, Applied Physics B **81**, 897 (2005).

[194] A. Vagov, M. D. Croitoru, V. M. Axt, T. Kuhn, and F. M. Peeters, Phys. Rev. Lett. **98**, 227403 (2007).

[195] E. M. Gauger, A. Nazir, S. C. Benjamin, T. M. Stace, and B. W. Lovett, New Journal of Physics **10**, 073016 (2008).

[196] R. Alicki *et al.*, Phys. Rev. A **70**, 010501 (2004).

[197] D. Mogilevtsev *et al.*, Phys. Rev. Lett. **100**, 017401 (2008).

[198] J. Förstner, C. Weber, J. Danckwerts, and A. Knorr, Phys. Rev. Lett. **91**, 127401 (2003).

[199] A. Krügel, V. M. Axt, and T. Kuhn, Phys. Rev. B **73**, 035302 (2006).

[200] H. M. Gil *et al.*, iScience **24**, 102189 (2021).

[201] C. T. Matea *et al.*, International Journal of Nanomedicine **12**, 5421 (2017).

[202] S. K. Hazra, P. K. Pathak, and T. N. Dey, Phys. Rev. B **107**, 235409 (2023).

[203] N. V. Vitanov, A. A. Rangelov, B. W. Shore, and K. Bergmann, Rev. Mod. Phys. **89**, 015006 (2017).

[204] M. M. Mahana, S. Davuluri, and T. N. Dey, Phys. Rev. A **110**, 023716 (2024).

[205] C. Roy and S. Hughes, Phys. Rev. Lett. **106**, 247403 (2011).

[206] S. M. Ulrich *et al.*, Phys. Rev. Lett. **106**, 247402 (2011).

[207] L. Besombes, K. Kheng, L. Marsal, and H. Mariette, Phys. Rev. B **63**, 155307 (2001).

[208] E. Stock *et al.*, Phys. Rev. B **83**, 041304 (2011).

[209] A. Thoma *et al.*, Phys. Rev. Lett. **116**, 033601 (2016).

[210] J. Iles-Smith, D. P. S. McCutcheon, A. Nazir, and J. Mørk, Nature Photonics **11**, 521 (2017).

[211] S. Lüker *et al.*, Phys. Rev. B **85**, 121302 (2012).

[212] A. Debnath, C. Meier, B. Chatel, and T. Amand, Phys. Rev. B **86**, 161304 (2012).

[213] R. Mathew *et al.*, Phys. Rev. B **90**, 035316 (2014).

[214] P.-L. Ardelt *et al.*, Phys. Rev. B **90**, 241404 (2014).

[215] J. H. Quilter *et al.*, Phys. Rev. Lett. **114**, 137401 (2015).

[216] D. P. S. McCutcheon, N. S. Dattani, E. M. Gauger, B. W. Lovett, and A. Nazir, Phys. Rev. B **84**, 081305 (2011).

[217] R. Manson, K. Roy-Choudhury, and S. Hughes, Phys. Rev. B **93**, 155423 (2016).

[218] D. P. DiVincenzo, Science **270**, 255 (1995).

[219] E. F. et al., Science **292**, 472 (2001).

[220] P. M. et al., Science **290**, 2282 (2000).

[221] R. M. S. et al, Nature **439**, 179 (2006).

[222] P. R. Eastham and R. T. Phillips, Phys. Rev. B **79**, 165303 (2009).

[223] B. W. Shore, M. V. Gromovyy, L. P. Yatsenko, and V. I. Romanenko, American Journal of Physics **77**, 1183 (2009).

[224] W. Zhang, A. Noa, K. Nienhaus, L. Hilbert, and G. U. Nienhaus, Journal of Physics D: Applied Physics **52**, 414001 (2019).

[225] W. Jahr, P. Velicky, and J. G. Danzl, Methods **174**, 27 (2020).

[226] M. Bina, The European Physical Journal Special Topics **203**, 163 (2012).

[227] M. Glässl, M. D. Croitoru, A. Vagov, V. M. Axt, and T. Kuhn, Phys. Rev. B **84**, 125304 (2011).

[228] S. Lüker, T. Kuhn, and D. E. Reiter, Phys. Rev. B **96**, 245306 (2017).

[229] S. W. Jolly *et al.*, Nature Communications **10**, 2591 (2019).

[230] T. Kaldewey *et al.*, Phys. Rev. B **95**, 241306 (2017).

[231] A. L. Efros and L. E. Brus, ACS Nano **15**, 6192 (2021).

[232] S. Nemoto, Applied optics **29**, 1940 (1990).

[233] W. K. Chen, *The electrical engineering handbook* (Elsevier, 2004).

[234] W. P. Bowen, R. Schnabel, H.-A. Bachor, and P. K. Lam, Phys. Rev. Lett. **88**, 093601 (2002).

[235] N. Korolkova, G. Leuchs, R. Loudon, T. C. Ralph, and C. Silberhorn, Phys. Rev. A **65**, 052306 (2002).

[236] V. Chille *et al.*, Optics Express **24**, 12385 (2016).

[237] B. Bokić *et al.*, Symmetry **16**, 1053 (2024).

[238] D. Green and K. A. Forbes, Nanoscale **15**, 540 (2023).

TH-3976_186121017

List of publications

- Partha Das and Tarak Nath Dey, "Linear and nonlinear propagation of cylindrical vector beams through a nondegenerate four-level atomic system", Phys. Rev. A **110**, 063720 (2024).
- Partha Das and Tarak Nath Dey, "Self-focusing of lemon and radial vector beam inside an atomic vapour", Asian Journal of Physics **33**, 709-719 (2024).
- Partha Das and Tarak Nath Dey, "Comparative study of focusing with scalar and vector beams in an active Raman gain system", Phys. Rev. A **112**, 033519 (2025)
- Partha Das, Samit Kumar Hazra, and Tarak Nath Dey, "Structured beam controlled super-resolution in quantum dots via rapid adiabatic passage", (Communicated)

Conferences and workshop attended

- **One-Day Workshop on -Introduction to MATLAB**, Organized by IIT Guwahati, India, during 10 August 2019.
- **Non-Hermitian Physics (Online)**, Organized by ICTS, India, during 22-26 March 2021.
- **Structured Light and Spin-Orbit Photonics (SLSOP)** held offline from 29 November 2022 to 2 December 2022, at ICTS Bengaluru, India.
- **Research & industrial conclave-synergy'25** held offline from 10 October 2025 to 12 October 2025, at IIT Guwahati, India.
- **SPIE Photonics West** held offline from 17 January 2026 to 22 January 2026, at San Francisco, California, United States.